STRESS ASSESSMENT OF GEAR TEETH IN EPICYCLIC GEAR TRAIN FOR RADIAL SEDIMENTATION TANK

Grzegorz BUDZIK,* Tadeusz MARKOWSKI,* Michał BATSCH,*
Jadwiga PISULA,* Jacek PACANA,* Bogdan KOZIK*

*Faculty of Mechanical Engineering and Aeronautics, Department of Mechanical Engineering, Rzeszow University of Technology
35-959 Rzeszow, Al. Powstańców Warszawy 8, Poland

gbudzik@prz.edu.pl, tmarkow@prz.edu.pl, mbatsch@prz.edu.pl, jpisula@prz.edu.pl, pacanaj@prz.edu.pl, bogkozik@prz.edu.pl

Received 21 January 2020, revised 18 August 2020, accepted 21 August 2020

Abstract: The paper presents the strength evaluation of planetary gear teeth designed for a radial sedimentation tank drive. A novel type of gear drive, composed of a closed epicyclic gear train and an open gear train with internal cycloidal gear mesh is proposed. Contact stress and root stress in the planetary gear train were determined by the finite element method and according to ISO 6336. The influence of the mesh load factor at planet gears on stress values was also established. A comparison of the results followed. It was observed that the mesh load factor on satellites depends mainly on the way the satellites and central wheels are mounted, the positioning accuracy in the carrier and the accuracy of teeth. Subsequently, a material was selected for the particular design of planetary gear and the assumed load. The analysis of the obtained results allowed assuming that in case of gears in class 7 and the rigid mounting of satellites and central wheels, gears should be made of steel for carburizing and hardening. In case of flexible satellites or flexible couplings in the central wheels and gears in class 4, gears can be made of nitriding steel.

Key words: Planetary gear, FEM, ISO 6336

1. INTRODUCTION

Planetary (epicyclic) gears are gear systems in which at least one gear, called a planet, has no fixed axis, and is instead supported by a rotating part called a carrier. Usually several planet gears are used, so that the transmitted power is distributed, allowing the dimensions of the entire gear system to be reduced. A key factor here is the uniformity of load transfer expressed by the mesh load factor K_γ. Its value determines the percentage share in transmitting power of planet gear. This, as it was proved by Singh (2005, 2010), Ligata et al. (2008), Fernandez del Rincon et al. (2013), Cooley and Parker (2014),Tsai et al. (2015, 2018), by Iglesias et al. (2017), Marques et al. (2016, 2017), and specified in ANSI/AGMA 6123-C16 (2016) standard depends, in particular, on the errors in the fabrication of gears, errors in the positioning on the carrier and the mounting structure of the planets.

The analyzed planetary gear is a part of the drive of a radial sedimentation tank (Fig. 1).

Propulsion is provided by a three-phase squirrel-cage motor, which drives a planetary gear train—the first reduction stage. An electronic control system for the motor should offer a soft start functionality so as to avoid overloading the mechanism. The gear train's output shaft connects to a pinion (a), which engages with an internal gear (b). The gear (b) is attached to a scraper (c), which is bearing-supported on the axis (d) of a sedimentation tank (e). In the present solution, the gear train in the second reduction stage (gears (a) and (b)) is an open gear train submerged in waste water, whereas the epicyclic gear train is a closed gear train located above the surface of waste water. A type series of second-stage open gear trains for scrapers of a diameter from 4 m to 36 m was designed as part of the present project. The details of the analysis and synthesis of second-stage gear train meshing were presented in a study by Batsch et al. (2017). Data used in the design of the planetary gear train were determined on the basis of a dynamic analysis of the entire drive system as well as sedimentation and flotation process requirements.

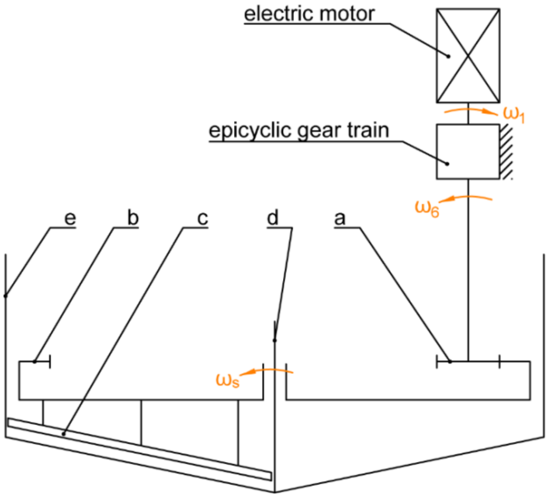

Fig. 1. Proposed kinematic system of a new radial settling tank drive

This paper presents the results of the preliminary calculations of strength of the teeth of a planetary reduction gear designed for radial sedimentation tank drives. Calculations were carried out in accordance with ISO 6336 standard and the finite element meth-

DOI 10.2478/ama-2020-0018

od. The analyses were aimed at selecting the material and determining the condition of the material that would ensure load transmission in the planetary gear train.

2. KINEMATICS

The radial scraper is a device operating at a very low rotation speed (approx. 1 rpm). In order to drive it with a conventional cage induction motor, one should use gearboxes with a large reduction ratio. Planetary gears are one of the gears that allow this while maintaining a relatively small number of reduction stages. There are many design variants of this type of gears, among which a large part has wheels with internal toothing (Dadley, 2002). Finishing this type of teeth can be troublesome due to the need to use special grinding heads. For this reason, it was decided to use the kinematic system of the gears, in which only wheels with external toothing are present. The need to use a large reduction ratio and the desire to use only external gearing prompted the authors to choose gears, whose kinematic diagram is shown in Figure 2.

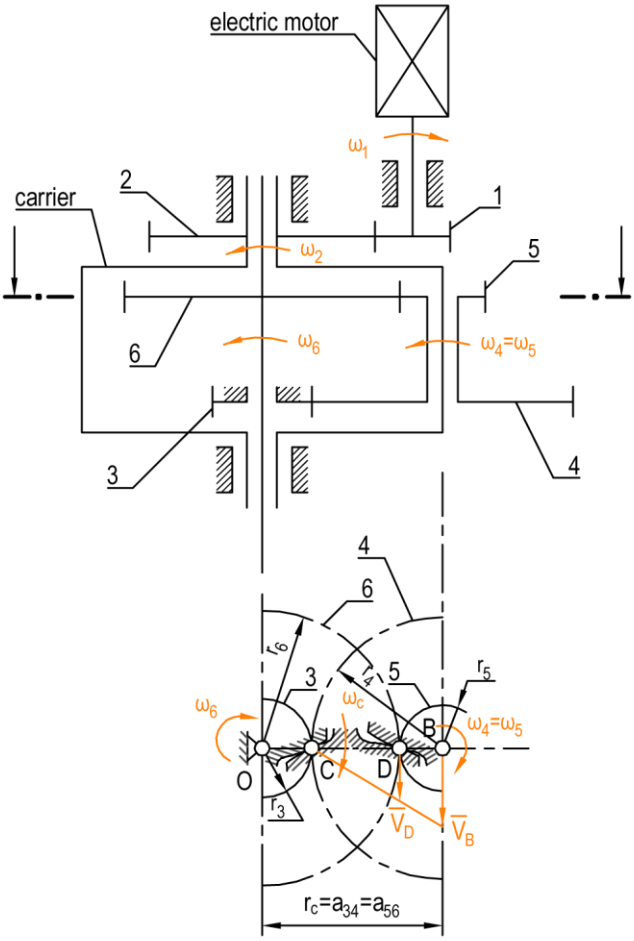

Fig. 1. Kinematic diagram of gear, where: ω_1 – gear 1 angular velocity, ω_2 – gear 2 angular velocity, ω_4 – gear 4 angular velocity, ω_5 – gear 5 angular velocity, ω_6 – gear 6 angular velocity, B – planet's centre of rotation, D – gear 5 & 6 contact point, C – gear 3 and 4 contact point (planet's momentary centre of rotation), O – gear 6 center of rotation, a_{34} – distance between axes of gears 3 and 4, a_{56} – distance between axes of gears 5 and 6

Gear 1, meshing with gear 2, is driven by an electrical motor. Gear 2 has a rigid connection to the carrier. The carrier supports three planets including gears 4 and 5, fixed to each other. Gear 4 rolls against a stationary sun gear (3). Meanwhile, gear 5, meshing with gear 6, transmits velocity and torque to the gear's output shaft. In the discussed case, spur gears were applied, whose parameters are listed in Table 1.

Tab. 1. Gear parameters

Gear no.	Module [mm]	Number of teeth [-]	Profile shift coefficient [-]	Working pitch radius [mm]	Meshing width [mm]
1	2.75	21	0.1799	29.1818	25
2		56	0.2450	77.8182	
3	3	30	0.6110	46.7797	45
4		29	0.7100	45.2203	
5	3.5	26	-0.0786	45.1321	45
6		27	-0.1219	46.8679	

The second gear's (carrier's) angular velocity is given by formula (1):

$$\omega_2 = \omega_c = \omega_1 \frac{r_1}{r_2} \tag{1}$$

where: r_1 – gear 1 rolling radius, r_2 – gear 2 rolling radius. The planet rotates relative to the momentary centre of rotation C. Consequently, from the equality of linear velocities of point B assigned to the carrier and gear 4 stems the following relationship (2):

$$\omega_c = \omega_4 \frac{r_4}{r_c} \tag{2}$$

Likewise, on the basis of the equality of linear velocities of point D assigned to gears 5 and 6, the angular velocity of planet (3) was calculated

$$\omega_4 = \omega_5 = \omega_6 \frac{r_6}{r_4 - r_5} \tag{3}$$

By introducing relationship (3) into formula (2), planetary stage gear ratio (4) was obtained:

$$i_e = \frac{\omega_C}{\omega_6} = \frac{r_4 r_6}{(r_4 - r_5) r_C} = 261 \tag{4}$$

Taking into account cylindrical stage gear ratio $i_c = r_2/r_1$, the overall gear ratio is given by formula (5):

$$i = i_c i_e = \frac{r_2}{r_1} \cdot \frac{r_4 r_6}{(r_4 - r_5) r_C} = 696 \tag{5}$$

3. DISTRIBUTION OF MESHING FORCES

Figure 3 shows the distribution of meshing forces in the planetary gear stage. The carrier is acted upon by torque T_c, resulting from motor torque $T_1 = 1.95 Nm$ and the gear ratio of the cylindrical stage (6):

$$T_c = i_c T_1 = 5.20 Nm \tag{6}$$

From the equations of the balance of torques acting on the planet, the following relationship (7) may be developed:

$$F_{34} = F_{65} \frac{r_5}{r_4} \tag{7}$$

DOI 10.2478/ama-2020-0018

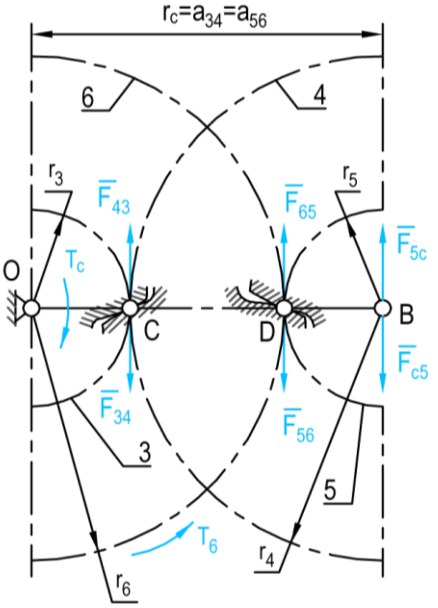

Fig. 3. Distribution of meshing forces in planetary gear stage, where: T_c – carrier torque, F_{34} – circumferential force exerted by gear 3 on gear 4, F_{43} – circumferential force exerted by gear 4 on gear 3, F_{56} – circumferential force exerted by gear 5 on gear 6, F_{65} – circumferential force exerted by gear 6 on gear 5, F_{5c} – circumferential force exerted by planet on carrier, F_{c5} – circumferential force exerted by carrier on planet, T_6 – resistance torque affecting output shaft

By using relationship (7) in the equation, the balance of forces acting on the planet, we may obtain (8):

$$F_{c5} = F_{65}\frac{r_4 - r_5}{r_4} \tag{8}$$

Taking into account that $F_{c5} = \frac{T_c}{r_c}$, the circumferential force at point D is given by formula (9):

$$F_{65} = \frac{T_c}{r_c}\frac{r_4}{r_4 - r_5} = 29006N \tag{9}$$

By introducing relationship (9) into (8), we ultimately arrive at the circumferential force at point C (10):

$$F_{34} = \frac{T_c}{r_c}\frac{r_5}{r_4 - r_5} = 28949N \tag{10}$$

The above equations were derived for a case in which a single planet gear occurs. In reality, in meshing force calculations, one must include the number of planet gears n and the load distribution coefficient K_Y according to formulas (11):

$$F'_{34} = \frac{K_Y}{n}F_{34};\ F'_{65} = \frac{K_Y}{n}F_{65} \tag{11}$$

In a perfect situation (even load distribution over planet gears $K_Y = 1$) all forces balance out, exerting no stress on the bearings of the output shaft or the carrier. The bearings may be stressed if the distribution of the load becomes uneven, and the forces do not balance out entirely.

4. STRENGTH ASSESSMENT ACCORDING TO ISO 6336

Strength calculations were limited to determining nominal stress values resulting from static tooth load.

4.1. Contact stress

Following the ISO 6336-2 (2006) standard, nominal contact stress values are given by formula (12):

$$\sigma_{H0} = Z_H Z_E Z_\varepsilon \sqrt{\frac{F'}{db}\cdot\frac{u+1}{u}} \tag{12}$$

where: Z_H – zone factor, Z_E – elasticity factor, Z_ε – contact ratio factor, F' – circumferential force, d – drive gear pitch diameter, b – ring width, u – gear pair ratio. Calculation procedures determining individual coefficients were described in the above-mentioned standard. The resulting stress values for individual gear pairs are shown in Table 2.

Tab. 2. Analytically-determined contact stress values

	Mesh load factor K_Y [-]				
	0.7	1	1.1	1.2	1.3
	Nominal contact stress σ_{H0} [MPa]				
Gear pair 1-2	103.20				
Gear pair 3-4	712.01	851.02	892.56	932.25	970.31
Gear pair 5-6	776.04	927.54	972.81	1016.07	1057.56

4.2. Root stress

As it is given in ISO 6336-3 (2006) standard, nominal root stress values are calculated by means of formula (13):

$$\sigma_{F0} = Y_F Y_S \frac{F'}{bm} \tag{13}$$

where: Y_F – form factor, Y_S – stress correction factor, F' – circumferential force, m – module, b – meshing width. Calculation procedures for determining individual coefficients were described in the above-mentioned standard. The resulting stress values for individual gears are shown in Table 3.

Tab. 3. Analytically-determined root stress

	Mesh load factor K_Y [-]				
	0.7	1	1.1	1.2	1.3
	Nominal root stress σ_{F0} [MPa]				
Gear 1	2.79				
Gear 2	2.80				
Gear 3	148.40	212.00	233.20	254.40	275.60
Gear 4	146.02	208.61	229.47	250.33	271.19
Gear 5	118.60	169.43	186.37	203.32	220.26
Gear 6	119.89	171.27	188.40	205.53	222.65

5. FEM SIMULATION

5.1. Computational model

Numerical calculations of the gear motor were performed in Abaqus software by means of the finite element method (FEM). Key stress values were determined based on the models that accurately represent the dimensions of real gearbox components. These were compared with results obtained from analytical calculations. To simplify finite element model, the entire task was split into three phases, which covered consecutive gear motor stages.

Since the gearing contains cylindrical spur gears, numerical FEM calculations were performed using flat models based on the plane stress states theory developed by Rusiński et al. (2000). For each of the stages, computational models were cross-sections through the center of the width of gears of a particular gearing stage. Such procedure, as it was concluded by Kopecki and Witek (2000) and by Rusiński et al. (2000), guarantees accurate results with considerably shorter calculation and result processing time.

It was assumed that the gears are made of steel of the following parameters: Young's modulus $2.05 \cdot 10^{11}$ Pa, Poisson coefficient 0.3. All boundary conditions, loads, restraints and displacements were defined according to the analytically pre-calculated values and the adopted kinematic system. Frictionless contact between the carrier and the planet gear (item 3 in Fig. 4) was assumed. The axis of the carrier was connected with a rigid body to the axis of the sun gear (item 4 in Fig. 4). In this case, the effect of play on the planet gears or errors in the geometry in the actual gear train were not investigated. The carrier axis was allowed to moved only over a circle, the center of which was placed on the axis of the sun gear. The movement of the carrier arising from the gear train kinematics was forced, and resistance (torque) was defined on the planetary gear due to its connection to gear 5 (Fig. 2).

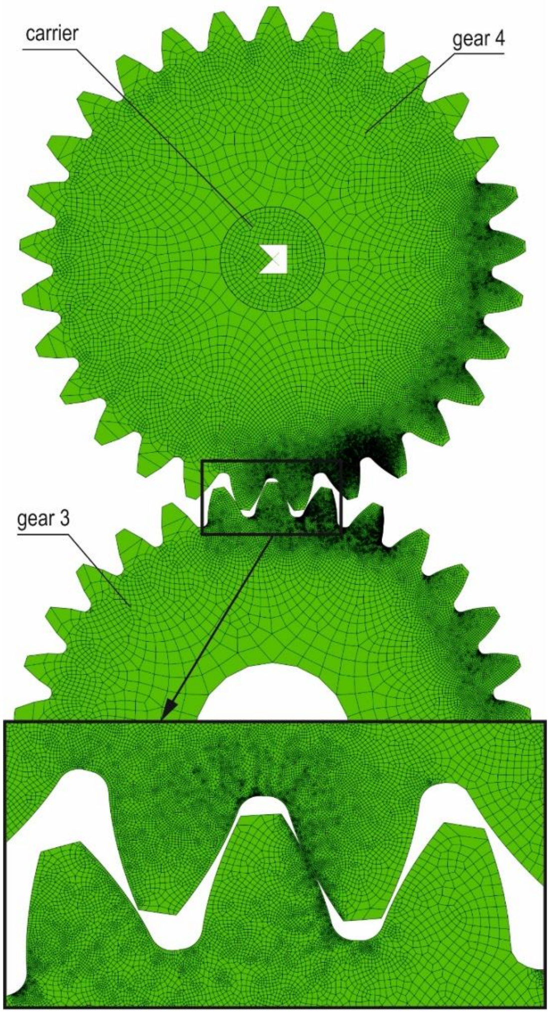

Fig. 4. Gear model designed for calculations in Abaqus software

The models were discretized, that is, divided into finite elements in an uneven manner according to the recommendations formulated by Budzik and Pacana (2008) and Kopecki and Witek (2000). Definitely, the largest density of nodes was present in the toothed ring area, with lower density in other locations on the models, which can be seen in Figure 4. Also, within a single tooth, differentiation of the mesh was introduced by using several times more finite elements in the discretization of the active tooth flank than for its passive side (Fig. 4). It made possible to shorten the calculations and to get highly accurate results in key areas. The discretization performed in Abaqus's pre-processor, CPS4R quadrilaterals were used.

Figure 4 presents an overview of the model prepared for calculations in Abaqus software for the second gear stage. Apart from gears 3 and 4, a model of the carrier was also included, through which rolling trajectory for the planet gear was defined. Grid density in the area of the toothed rings of engaging gear models is clearly visible.

In the process of the analysis, both the model preparation and computational methods were kept the same for three stages of the gear.

5.2. Calculation results

The basic form in which the results were obtained was the distribution of reduced stress presented on previously prepared models. The analysis focused on the gear meshing area, where the highest stress values were recorded. The area is of fundamental importance in terms of strength. Figure 5 shows sample results for the second stage of the gearbox.

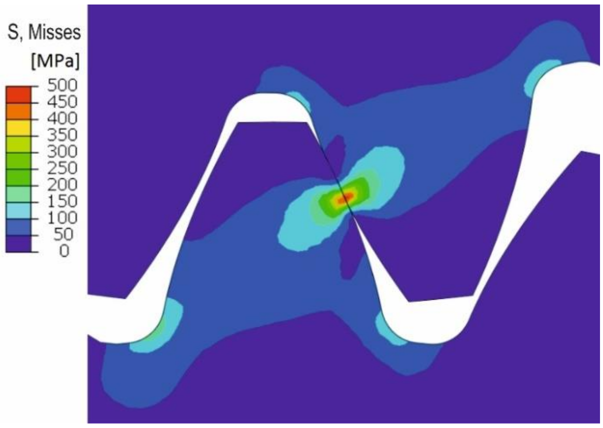

Fig. 5. Distribution of reduced stress in gear 3 and 4 meshing area

Evidently, the highest stress values were recorded at the point of contact between the flanks of meshing teeth. Stress concentration is also present at the opposite side of the teeth. In accordance with ISO 6336-1 (2006) standard, stress in these areas constitutes a basic criterion for assessing the correctness of the designed gear. The results showed as stress distribution and helped to identify areas at risk. However, they are insufficient to perform precise strength calculations. In order to increase clarity, the results may be presented as charts. Figures 6 and 7 show sample reduced root stress values for gears 3 and 4. The illustrations also contain schematic charts taken into account in analytical calculations according to a generally approved literature on strength calculations and gear performance quality (Sánchez et al., 2019). Here, we assume a rectilinear load distribution, evenly divided into three stages of engagement. As can be seen, the real nature of load exerted on a gear tooth is slightly different. It does not interfere with general-purpose gear calculations, however, when designing more demanding systems, one must take into account more accurate results offered by the numerical FEM method.

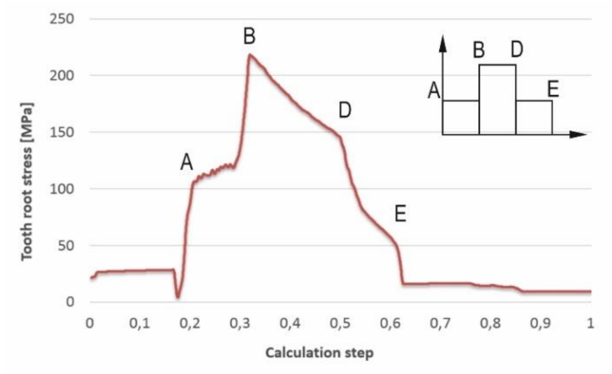

Fig. 6. Changes in reduced root stress values in gear 3 (A, B, D, E – characteristic points on path of contact, A – entry into engagement of second tooth (two-pair meshing), B – lowest point of single tooth contact (LPSTC), D – highest point of single tooth contact (HPSTC), E – exit from meshing of second tooth)

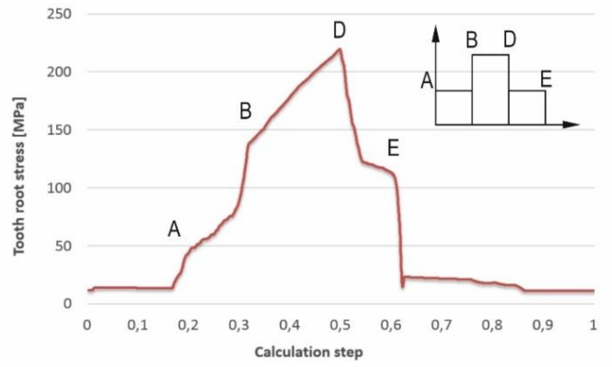

Fig. 7. Changes in values of reduced root stress in gear 4 (A, B, D, E – characteristic points on path of contact, description as in Fig. 5)

Charts illustrating reduced root stress as well as contact stress values for all gears of the analyzed gearing were created on a similar basis. This helped trace the moments where extreme values occurred and read their quantity. Subsequently, one may compare the results obtained in numerical calculations with the ones generated in analytical calculations and confirm their mutual consistency.

5.3. Uneven load distribution

As multipath gears are characterized by the risk of uneven load distribution on each of the paths (Parker and Lin, 2004; Budzik et al. 2013), the issue was also examined in the analysis.

In the initial solution for $K_\gamma = 1$, each of the three planets carried the same load. Knowing that during its operation, the torque value transmitted by each path is variable, such assumption was also made in FEM numerical calculations. It was assumed that the maximum practically foreseeable value of the mesh load factor would occur (ANSI/AGMA 6123-C16), and the load at the second and third stage of the gear motor was proportionally increased. An inverse situation was also taken into account, with the planet transmitting a torque lower than nominal, because the two remaining ones carry a higher load. The results of numerical calculations obtained for the initial case and for inequality coefficients of 0.7, 1.1, 1.2 and 1.3 were juxtaposed to compare how unbalanced load distribution affects stress values in the gears of a planetary gearing.

The results for reduced root stress and contact stress for all wheels of speed reducing gears were listed in Tables 4 and 5.

Tab. 4. Contact stress values on basis of numerical FEM calculations

	Mesh load factor K_γ [-]				
	0,7	1,0	1,1	1,2	1,3
	Contact stress [MPa]				
Gear pair 1-2	112,21				
Gear pair 3-4	698,98	898,45	914,51	938,44	978,98
Gear pair 5-6	813,42	937,44	966,54	997,12	1012,81

Tab. 5. Reduced root stress on basis of numerical FEM calculations

	Mesh load factor K_γ [-]				
	0,7	1,0	1,1	1,2	1,3
	Tooth root stress [MPa]				
Gear 1	2,71				
Gear 2	2,67				
Gear 3	157,96	222,74	242,49	263,28	284,73
Gear 4	156,32	224,80	245,00	266,69	288,67
Gear 5	117,55	183,21	190,35	198,53	206,42
Gear 6	126,61	189,14	197,46	205,35	212,25

6. COMPARISON OF RESULTS

The results are presented in charts (Figures 8 and 9).

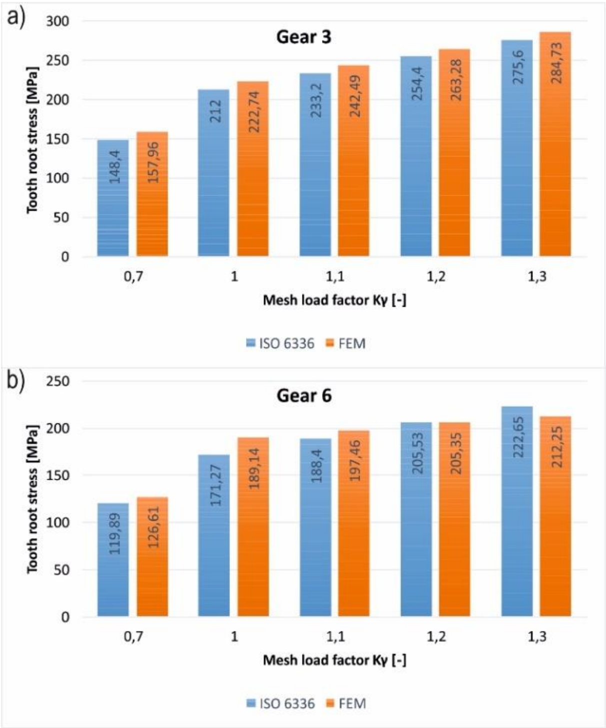

Fig. 8. Reduced root stress for: a) gear 3, b) gear 6

Reduced root stress values determined by FEM simulation approximate those obtained analytically. FEM error with respect to the analytical method reaches a maximum of 10.43% with a reduced stress difference of 17.87 MPa for gear 6 and mesh load factor 1.0. In addition, the largest differences in reduced root stress occur for all wheels with a load distribution coefficient equaling 1.0.

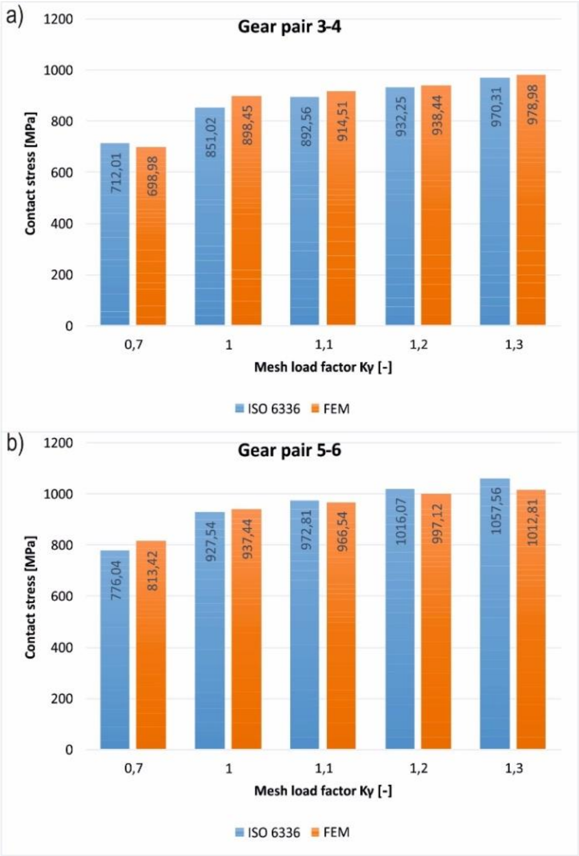

Fig. 9. Contact stress values for: a) pair 3-4, b) pair 5-6

In the case of contact stress, it was noted that the FEM error related to the analytical method shows neither an upward nor a downward trend with increasing load (increase of load distribution coefficient). The largest difference in the value of reduced stress 47.43 MPa, constituting approx. 5.6% of the value of analytical stress occurred for the mash load factor 1.0 (Fig. 9b).

7. SUMMARY AND CONCLUSIONS

On the basis of the performed calculations and simulations, it can be concluded that:

- The first gearing stage is slightly loaded, and gears 1 and 2 can be made of quenched and tempered steel, for example, 42CrMo4.
- The epicyclical stage of the gearing is subjected to the highest load, and bending and contact stresses necessitate the use of steel for surface hardening (nitriding or carburizing and hardening).

In addition, the mesh load factor over planets has a significant effect on the selection of the material for planetary stage gears (gear pairs 3-4 and 5-6). It depends in particular on how the planet and sun gears are mounted, the positioning accuracy on the carrier, tooth fabrication accuracy and, in the planetary gearing discussed in this study, the accuracy of the positioning of the teeth of gear 5 relative to gear 4. Guidelines contained in ANSI/AGMA 6123-C16 (2016) standard, as well as simulations and calculations performed prompted the authors to form the following conclusions:

- If planet and sun gears are supported without flexible mounts, and gears are made to class 7 (mesh load factor according to ANSI/AGMA 6123-C16 (2016) standard equals 1.23), gears should be made of carbon steel for carburizing and hardening.
- If planets are flexibly mounted or flexible clutches are used and gears are made to class 4 (mesh load factor according to ANSI/AGMA 6123-C16 (2016) standard equals 1), gears may be made of steel for nitriding.

The analysis of the load capacity of a multi-path gearing presented in this study was aimed to determine the locations of potential failures and work-flow hazards. Apart from gear contact areas, no other locations of increased stress values were found. One should note, however, that stress values obtained in numerical calculations are slightly different from the actual ones. This is due to both the use of discrete models as well as a simplified load pattern. Numerical analyses did not include, for example, friction, safety or overload factors. Without these additional parameters, the stresses calculated by numerical FEM often do not yield ultimate results. The obtained results allow to identify risks or simulate engagement, providing very useful information for design purposes. However, they should always be checked by means of other computational or experimental methods. Verification of the results enables the introduction of suitable similarity coefficients into numerical calculations. This makes them an even more useful tool in the hands of a gear engineer.

REFERENCES

1. **ANSI/AGMA 6123-C16** (2016), Design Manual for Enclosed Epicyclic Gear Drives.
2. **Batsch M., Markowski T., Zubrzycki M.** (2017), Mathematical model of internal pin gear mesh (in Polish), *STAL Metale Nowe technologie.* Koła zębate - projektowanie, wytwarzanie, pomiary, eksploatacja, 13–16.
3. **Budzik G., Kozik B., Pacana J.** (2013)**,** Defining influence of load conditions on distribution and value of stresses in dual-power-path gear wheels applying FEM, *Aircraft Engineering and Aerospace Technology*, Vol. 85, No. 6, 453–459.
4. **Budzik G., Pacana J.** (2008), Analysis of the correctness of the FEM solution depending on the type and number of finite elements used (in Polish), *Acta Mechanica Slovaca*, 3-A/2008, t. 12, Technical University of Kosice, 327–332.
5. **Cooley C.G., Parker R.G.** (2014) A review of planetary and epicyclic gear dynamics and vibrations research, *Applied Mechanics Reviews*, Vol. 66, No. 4, Article Number 040804
6. **Dadley D.W.** (2002), *Handbook of Practical Gear Design*, CRC Press LLC.
7. **Fernandez del Rincon A., Viadero F., Iglesias M., García P., de-Juan A., Sancibrian R**. (2013) A model for the study of meshing stiffness in spur gear transmissions, *Mechanism and Machine Theory*, Vol. 61, 30–58, doi.org/10.1016/j.mechmachtheory.2012.10.008
8. **Iglesias M., Fernandez del Rincon A., de-Juan A., Garcia P., Diez-Ibarbia A., Viadero F.** (2017) Planetary transmission load sharing: Manufacturing errors and system configuration study, *Mechanism and Machine Theory*, Vol. 111, 21–38, https://doi.org/10.1016/j.mechmachtheory.2016.12.010.

9. **ISO 6336-1** (2006), Calculation of load capacity of spur and helical gears — Part 1: Basic principles, introduction and general influence factors.
10. **ISO 6336-2** (2006), Calculation of load capacity of spur and helical gears — Part 2: Calculation of surface durability (pitting).
11. **ISO 6336-3** (2006), Calculation of load capacity of spur and helical gears — Part 3: Calculation of tooth bending strength.
12. **Kopecki H., Witek L.** (2000), Influence of the type and number of elements on the error and convergence of the FEM solution on the example of the stability analysis of a compressed member (in Polish). *V Konferencja Naukowo-Techniczna, Military University of Technology*, *(WAT)*, IPPT PAN, Warsaw - Rynia.
13. **Ligata H., Kahraman A., Singh A.** (2008), An experimental study of the influence of manufacturing errors on the planetary gear stresses and planet load sharing, *Journal of Mechanical Design*, Transactions of the ASME, Vol. 130, No. 4, 577–595.
14. **Markowski T., Budzik G., Pacana J.** (2010), Criteria for selecting a numerical model for the strength calculations of a cylindrical gear with the FEM method (in Polish), *Modelowanie Inżynierskie*, Vol. 8, No. 39, 135–142.
15. **Marques P.M.T., Martins R.C., Seabra, J.H.O.** (2016) Power loss and load distribution models including frictional effects for spur and helical gears, *Mechanism and Machine Theory*, Vol. 96, Part 1, 1–25, DOI: 10.1016/j.mechmachtheory.2015.09.005
16. **Marques P.M.T., Martins R.C., Seabra, J.H.O.** (2017) Analytical load sharing and mesh stiffness model for spur/helical and internal/external gears – Towards constant mesh stiffness gear design, *Mechanism and Machine Theory,* Vol. 113, 126–140, doi.org/10.1016/j.mechmachtheory.2017.03.007
17. **Parker R.G., Lin J.** (2004) Mesh Phasing Relationships in Planetary and Epicyclic Gears, *Journal of Mechanical Design, Vol. 126(2), 365–370, https://doi.org/10.1115/1.1667892*
18. **Rusiński E., Czmochowski J., Smolnicki T.** (2000), *Advanced finite element method in load-bearing structures* (in Polish), The Wrocław University of Technology Publishing House, Wrocław.
19. **Sánchez M.B., Pleguezuelos M., Pedrero J. I.** (2019), Strength model for bending and pitting calculations of internal spur gears, *Mechanism and Machine Theory*, Vol. 133, 691–705, https://doi.org/10.1016/j.mechmachtheory.2018.12.016
20. **Singh A.** (2005), Application of a System Level Model to Study the Planetary Load Sharing Behavior, *Journal of Mechanical Design*, Vol. 127, 469–476.
21. **Singh A.** (2010), Load sharing behavior in epicyclic gears: Physical explanation and generalized formulation, *Mechanism and Machine Theory*, Vol. 45, 511–530.
22. **Tsai S.-J., Huang G.-L., Ye S.-Y.** (2015) Gear meshing analysis of planetary gear sets with a floating sun gear, *Mechanism and Machine Theory*, Vol. 84, 145–163, https://doi.org/10.1016/j.mechmachtheory.2014.03.001
23. **Tsai S.-J., Ye S.-Y.** (2018), A computerized approach for loaded tooth contact analysis of planetary gear drives considering relevant deformations, Mechanism and Machine Theory, Vol. 122, 252–278, https://doi.org/10.1016/j.mechmachtheory.2017.12.026
24. **Wiktor J.** (2004), *Analytical and numerical methods of analysis of geometric parameters, motion disturbances and strength of cylindrical gears* (in Polish), The Rzeszów University of Technology Publishing House, Rzeszów.

Studies carried out as part of project “Designing an innovative type of a scraper with an integrated planetary drive for new or modernized sedimentation tanks,” No. POIR.01.01.01-00-0286/15-00 under Action 1.1 “R&D Projects of Businesses,” Sub-Action 1.1.1 “Industrial research and development work performed by businesses” POIR in 2015. Competition 1/1.1.1/2015 of the Intelligent Development Operation Programme 2014–2020 co-funded from the European Regional Development Fund.

DOI 10.2478/ama-2020-0019

PARAMETRIC STUDY ON THE SPRING-BACK EFFECT IN AA5052 ALLOY IN THE COURSE OF THREE-POINT ROLL BENDING PROCESS

Viswanathan SHRINAATH,*Ramalingam VAIRAVIGNESH,*Ramasamy PADMANABAN*

*Department of Mechanical Engineering, Amrita School of Engineering, Coimbatore, Amrita Vishwa Vidyapeetham,
Amritanagar, Coimbatore - 641 112 Tamil Nadu, India

anand.shri96@gmail.com, r_vairavignesh@cb.amrita.edu, dr_padmanaban@cb.amrita.edu

Received 25 December 2019, revised 13 October 2020, accepted 16 October 2020

Abstract: Three-point roll bending is one of the most common forming processes employed to obtain the desired radius of curvature in the sheet metal operations. Upon the removal of the forming load, the sheet metal deforms to a lesser extent than that of the required dimension. This phenomenon is termed as spring-back and is considered the most challenging areas of research in three-point roll bending of sheet metals. This study aims to develop a numerical model using HyperWorks and Radioss solver to understand the influence of load, the distance between the forming rollers, and its thickness on the spring-back effect in the course of three-point roll bending of sheet metal (AA5052). The results of the numerical model are validated with the results of the experimental trials. Besides, a statistical model is developed to relate the amount of spring-back with the three-point roll bending process parameters.

Keywords: Three-point roll bending, multi-pass forming process, spring-back, dynamic explicit analysis, optimization

1. INTRODUCTION

AA5052 is an aluminum alloy with magnesium as the primary alloying element and is known for its high corrosion resistance and low weight to high strength ratio. Hence, it is widely used in aircraft tubes, automobile parts, and hydraulic tubes. Besides, AA5052 alloy has good formable properties. However, the forming of AA5052 alloy has many challenges. Sheet metal forming is one of the important and most common processes used in the manufacturing industries (Hecker, 1975; Hu et al., 2002; Parsa et al., 2012). During forming processes, force is applied on the sheet metal to modify its geometry rather than the removal of material. Three-point roll bending is one of the forming processes, which bends a long continuous strip of sheet metal into a large or medium size tubular section that is typically used in aircraft structures, pressure vessels, and tunnels.

The symmetric roll bending machines have three rollers with an arrangement similar to that of an isosceles triangle. In symmetric roll bending machines, the top roller moves vertically, and the bottom rollers move horizontally. The vertical movement of the roller applies a load on the sheet metal. The rotation of bottom rollers helps in uniform distribution of the load along the length of the sheet metal, forming the sheet metal to the desired radius of curvature. However, the recovery of the elastic region in the sheet metal upon removal of load results in the spring-back effect. The forming of the sheet metal to the desired radius of curvature depends on the thickness of the sheet metal, material property (Young's modulus, Poisson's ratio & yield strength), and the process parameters such as displacement of the top roller (TRD), the distance between the bottom rollers (DBBR), the radius of top and bottom roller.

A few studies attempted to understand the behavior of the sheet metal during the forming process (Abvabi et al., 2014; Ghimire et al., 2017; lee et al., 2005; Westermann et al., 2011; Xing et al., 2013; Xu et al., 2004; Belykh et al., 2016; Davies and Magee, 1977; Fortin et al., 1983; Kumar et al., 2014). Hansen and Jannerup(1979) developed an analytical model to predict the final curvature (range) of the sheet metal. The results indicate that the final curvature is highly sensitive to the forming parameters than that of the material properties. However, the analytical model predictions could not determine the exact final curvature. Hardt et al. (1982) developed a shape controller system for the forming process. The shape controller attains the desired shape based on the loaded sheet metal, material properties at the loaded position, and the amount of elastic spring-back. A series of experiments were conducted with a shape controller to attain the desired shape. However, the dynamic control of the workpiece was highly challenging with the shape controller.

Yang and Shima(1988) determined the relationship between the displacement of the center roller and the final curvature of the sheet metal in the forming process. He also demonstrated that the distribution of the curvature was axisymmetric about a point and was not symmetric about the center of the axis. However, material properties were not considered in the analytical method. Gandhi and Ravel (2006) developed models for single-pass bending with constant Young’s modulus and multi-pass bending with constant and varying Young’s modulus. However, the study lacks a comprehensive analysis of the influence of the number of passes and the load applied. Srivastav and Shinde (2010) studied the dynamic process of the plate rolling using finite element analysis. A 3D, dynamic elastic-plastic for steel material, was developed and validated to study the stress and strain in the sheet metal using Radioss. However, the influence of parameters was not discussed explicitly.

A few analytical models were developed to analyze the spring-back effect in the three-point roll bending of aluminum alloys (Yang and Shima, 1988; Paulsen and Welo, 1996; Badr et al., 2017; Guo et al., 2017; Ameen, 2012; Liu et al., 2018; Ktari et al., 2012; Khamen et al., 2016). However, these models were developed based on the theory of bending in which the neutral axis remains at the midpoint along with the thickness and the material properties like Young's modulus remaining constant for the entire process. However, in practical situations, Young's modulus changes while deforming the material to the desired shape.

Most of the studies were carried out using finite element models to correlate the process parameters with the experiment results (final radius of curvature). Finite element analysis to investigate the effect of process parameters on the spring-back effect during deformation processing of materials is not available in the open literature.

The study aims to perform a parametric study on the three-point roll bending process and spring-back effect in the materials. A simulation model was developed for the three-point process using HyperWorks(2010) and Radioss(2014). The model was validated using the experimental test. The influence of process parameters in three-point roll bending on the spring-back effect was analyzed using a hybrid linear and radial basis function model. The model was used to optimize the process parameters to achieve the minimum spring-back effect (desired radius of curvature).

2. MATERIALS AND METHODS

2.1. Computational Methodology

Computation methodology is a powerful and cost-effective tool used to predict the approximate solution for practical problems. In this work, the finite element method and design of experiments are used to explore the amount of spring-back in the three-point roll bending process.

2.1.1. Numerical Modeling

Non-linear dynamic finite element model was developed to predict the large plastic strain, large deformation, and contact phenomenon during the three-point roll bending process of the sheet metal. The finite element model was developed using HyperWorks(2010) and solved using a Radioss solver (2004). The bending process of sheet metal was simulated using the explicit analysis while the spring back process used the implicit analysis. The developed finite element model used a multi-stage forming process, where the top roller displacement was given stage-wise to achieve the accuracy of the formed radius of curvature. The accuracy of the developed model depends on the contact properties between roll and sheet metal. The mid-surface of the sheet metal was extracted to reduce the computation time and the results were calculated along the mid-surface normal.

2.1.2. Geometric Specification

The 3D solid model of three rollers and the sheet metal was developed, based on the three-point roll machine specification process condition given in Table 1.

Tab. 1. Geometric specification

Parameters	Dimension in mm
Top roller diameter	220
Bottom roller diameter	140
Distance between the bottom rollers	380
Sheet metal dimension	900×100×3

2.1.3. Meshing and Element Properties

The 3D model of the three-point roll bending process was imported and was meshed using Hypermesh. The roller and sheet metal were meshed using 2D first order quadrilateral element of element length 10 mm as shown in Figure 1. The sheet metal elements were modeled as orthotropic shell elements with an angle of 0° degree. The QEPH Shell element would auto-stabilize hourglass energy. The shell element properties were as follows: the thickness of sheet metal = 3 mm, number of integration point (N) = 5, Ithick = 1, and Iplastic = 1. Since the roller is a rigid body, three rigid elements were created for each roller using the RB2 element. RB2 element has one independent node at the center and all other nodes are dependent nodes connected to the independent node.

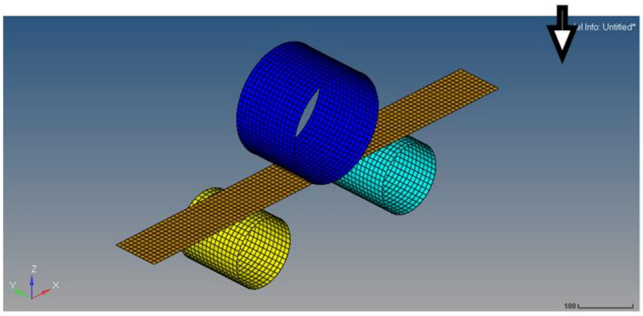

Fig. 1. Meshed model

2.1.4. Material Properties

The rollers were made of steel while the sheet metal was made of AA5052 alloy of thickness 3 mm. Since the sheet metal was deforming plastically in an anisotropic way, elastoplastic Hill's model (Hill, 1958) was used to define the shell element of the sheet metal. The material properties like Young's modulus, Poisson ratio, and density were given as input.

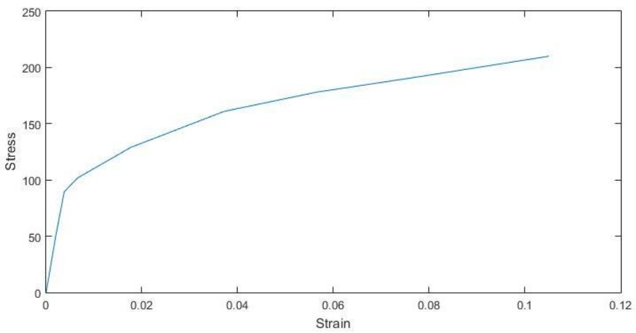

Fig. 2. True stress (MPa) – strain (ratio; no units) curve of Aluminum 5052

DOI 10.2478/ama-2020-0019

In this elastoplastic model, the effective stress-strain curve of Aluminum 5052 and Lankford formability constant was given as an input following the studies of Hecker (1975). The anisotropic coefficients (plastic strain ratio; no units) are as follows: R0 = 0.74, R45 = 0.48, and R90 = 1.04. Figure 2 shows the true stress-strain curve of AA5052.

2.1.5. Load and Boundary Conditions

The forming process was accomplished in two-steps, the first step is bending, that is, the load is given to the sheet metal by the displacement of the top roller and the second step is rolling, that is, the rollers rotate to distribute the load along the length of sheet metal. Hence, the constraints of the rollers were given to the independent nodes of the rigid element (RB2), all the dependent node would take the constraints given to the independent node. The constraints were given in the global axis, for the top displacement along the X3 axis, and rotation along the X2 axis was allowed. Similarly, for the bottom roller, only rotation along the X2 axis was allowed. Since this forming process is a multi-stage process, for each displacement of the top roller, the bottom roller rotates at 0.000785 rad/ms. The top roller was displaced 8 times by 5 mm totaling a displacement of 40 mm.

2.1.6. Contact Definition

In the finite element analysis, the Master-Slave approach was used to define the contact in the model. Since the surface of the sheet metal made a contact with the rollers, the surface to surface contact was defined in the finite element model. Rollers were defined as the master nodes since it was a rigid body, and sheet metal as slave nodes. The interaction between the roller and sheet metal was assigned as a sliding approach because the sheet metal slides into the roller by the friction factor. In this model, the friction is assumed to be a constant of 0.1. The gap between the sheet metal and roller was set constant because of no considerable change in the thickness of the sheet metal.

2.1.7. Spring-Back Procedure

Spring back is the recovery of the elastic region when the applied load is removed. For the spring back process, a separate engine file was created, and it was carried out as an implicit analysis. The spring back engine file would start after the termination time of the dynamic forming process.

2.2. Statistical Model

A manufacturing process is analyzed based on the process parameters, as the process parameters significantly influence the properties/geometries of the product. Conducting experimental/numerical trials for analyzing the influence of process parameters is a time-consuming process. Hence, the study adopted the Design of Experiments approaches to minimize the number of trials to study the influence of process parameters on the spring-back effect.

In this study, three factors namely top roller displacement (TRD), the distance between bottom rollers (DBBR), and sheet metal thickness (Thick) were varied at five levels. The numerical simulations were carried out based on the parametric combinations, given in Table 2. The finite element model was used to predict the amount of spring-back (geometry changes of the sheet metal before and after spring-back) in the roll forming process. A hybrid linear function and radial basis function was developed to correlate the process parameters with the amount of spring-back. The development of the hybrid linear function and radial basis function-based model is based on the previous literature (Ramalingam and Ramasamy, 2017; Vignesh et al., 2018; Vignesh and Padmanaban, 2018). The model was used to develop contour plots, which in turn were used to study the interactive effect of process parameters on the amount of spring-back in three-point roll bending of AA5052 alloy.

Tab. 3. Design Matrix

Sl. No.	Process Parameters						Amount of Spring Back (mm)*
	Real Value			Coded value			
	Thick (mm)	TRD (mm)	DBBR (mm)	Thick	TRD	DBBR	
1	1	40	380	-2	0	0	750
2	2	40	380	-1	0	0	345
3	3	30	380	0	-2	0	400
4	3	35	380	0	-1	0	270
5	3	40	360	0	0	-2	117
6	3	40	370	0	0	-1	150
7	3	40	390	0	0	1	218
8	3	40	400	0	0	2	258
9	3	45	380	0	1	0	130
10	3	50	380	0	2	0	100
11	4	40	380	1	0	0	140
12	5	40	380	2	0	0	100

*Geometry changes of the sheet metal before and after spring-back

2.3. Experimental Methodology

The three-point roll bending trails on AA5052 sheet metal were performed on the symmetrical three-point roll bending machine. The machine specification and the sheet metal specification are given in Table 1. In symmetrical three-point roll bending, the AA5052 alloy sheet metal was placed in such a way that the load will be acting on the midpoint of the sheet metal. Before applying the load, it was ensured that all the three rollers made contact with the sheet metal. The initial position of the top roller was noted and the top roller displacement was applied in steps. The top roller was displaced by 5 mm by the controller. Now at 5 mm of top roller displacement, the rotation velocity of 0.785 rad/s was given to the bottom rollers.

As the bottom roller rotated, the sheet metal moved in a horizontal direction because of the friction between the roller and the sheet metal. The bottom roller was rotated in both directions so that the direction could be reversed. The action was repeated until the load acted all over the sheet metal and until the top roller displaced up to 40 mm.

While removing the load, the sheet metal would spring-back until the equilibrium was achieved between the elastic and plastic regions in the sheet metal. By the spring-back effect, the radius formed by the top roller increases as soon as the top roller is moved back to the initial position. This geometry changes of the sheet metal before and after spring-back is measured as the amount of spring-back. By the experimental test, only the radius of the sheet metal after the spring-back is measured, which is known as the final radius of the sheet metal after the spring-back. The bend region length and the radius after spring-back were as follows: bend region length = 430 mm and radius after spring-back = 660 mm. Since the experiment was carried out without the pre-bending, the bend region was taken into consideration.

3. RESULTS AND DISCUSSIONS

3.1. Numerical Model

3.1.1. Mesh Convergence

A finite element model with sufficient mesh density was used in this study. A convergence study was performed with different mesh densities, as it affects stress, displacement, and CPU computation time. A poor mesh that has a large aspect ratio of the element, leads to inaccurate prediction or convergence problems. However, refining the mesh considerably increases the computation time. A Mesh convergence study for the sheet metal was performed. The results indicate that that the load transfer was almost the same for 10 mm and 8 mm element length. But the computational time was high for 8 mm element length. So, an element size of 10 mm was used for the study, as the predicted results were in good agreement with the experimental results.

3.1.2. Model Validation

The 2D finite element model was simulated based on the experimental data. The following results were obtained: stress distribution, strain distribution, deformation before and after spring-back, radius before spring-back, and after spring-back. Figure 3 shows the stress distribution in the sheet metal. The results indicate that plastic deformation occurred in the sheet metal when stress crossed the yield limit. Based on this stress distribution, the plastic strain developed in the sheet metal is shown in Figure 4.

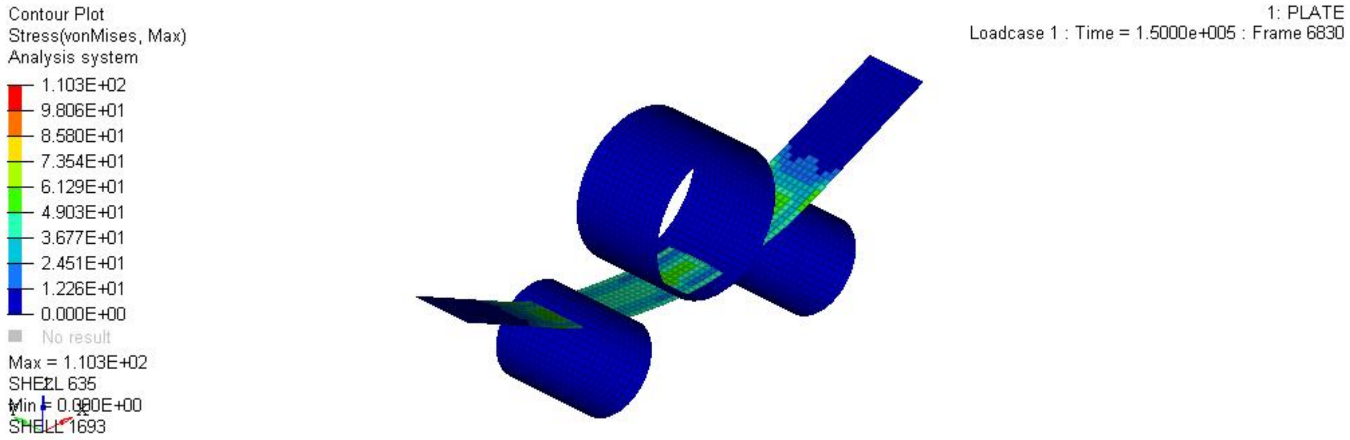

Fig. 3. Stress (MPa) distribution in the sheet metal

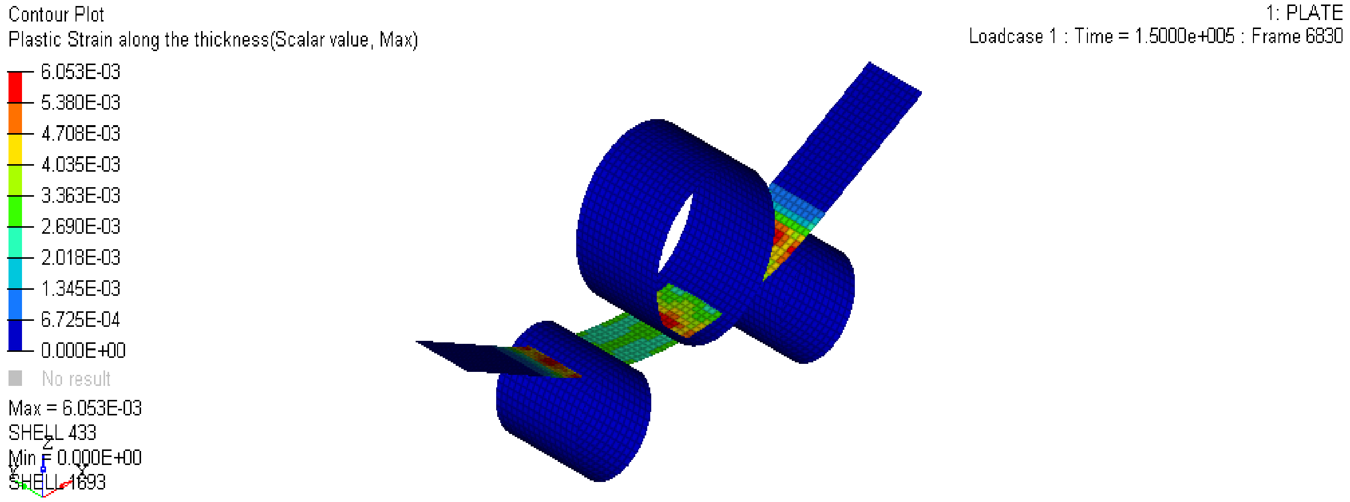

Fig. 4. Plastic strain (ratio; no units) distribution in the sheet metal

When the top roller contact was removed, the sheet metal underwent spring-back, that is, recovery of the elastic region in the material. If spring-back occurred, the radius of the deformed sheet metal was either higher or lower than that of the desired radius. The curvature of the sheet metal before spring-back was 507 mm and the curvature of sheet metal after spring-back 635 mm.

Table 3 shows the final radius of curvature after spring back from the finite element model and experimental test. The numerically predicted the final radius of curvature of the sheet metal was in good correlation with the experimental results.

Tab. 3. Model validation with Experimental test

	Simulation Result	Experimental Result
Radius after spring back (mm)	635	660

3.2. Statistical model

Table 2 shows the design matrix for variation in the process parameters and the corresponding spring-back. The process parameters (top roller displacement, the distance between bottom rollers, the thickness of sheet metal) are related to the response (amount of spring-back) using a hybrid linear-radial basis function model. The generated statistical model is a hybrid Linear-Radial Basis Function, that is given by equation (1). The Radial Basis Function network was developed using a multiquadric kernel with 4 centers, global width of 0.24811 and a regularization parameter, and a lambda of 0.0001.

$$\mathrm{T} = 118.2636 - 224.9054 * \mathrm{DBBR} - 258.9317 * \mathrm{TRD} - 924.9986 * \mathrm{Thickness} + \mathrm{RBF} \tag{1}$$

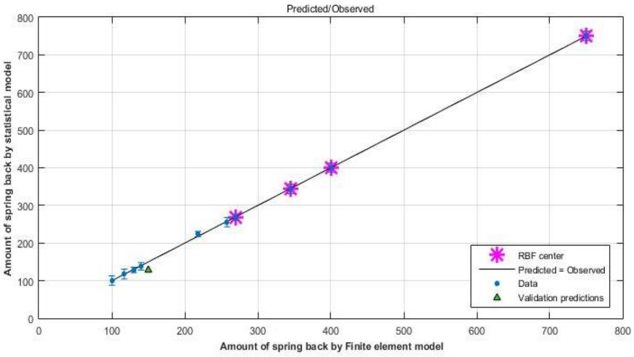

Fig. 5. Amount of spring back (mm) – Finite element model vs Statistical model

From Figure 5, a linear trend was observed between the amount of spring-back from the finite element model and the predicted statistical model. The coefficient of determination (R2) and root mean squared error (RMSE) value was used to assess the efficiency of the developed statistical model. The R2 was 1 for the statistical model, depicting its closeness with the finite element model predictions. The RMSE is 4.137 for the statistical model, which is small.

3.2.1. Effect of Process Parameters

The effect of TRD and the DBBR on the amount of spring back is shown in Figure 6. The material deformed at 30 mm TRD and 360 mm DBBR exhibited the largest spring-back. The amount of spring back reduced as the DBBR increased from 360 mm to 380 mm. With the further increment in DBBR from 380 mm to 400 mm, the amount of spring back increased. Similarly, if TRD increased, the amount of spring back decreased. The force exerted on the sheet metal for 30 mm of TRD was 260 N.

Correspondingly, the stress of 104.3 MPa and strain of 3.54e-03 was induced in the sheet metal. With an increase in TRD to 50 mm, the force exerted on the sheet metal was 310 N. The corresponding stress in the sheet metal was 115.7 MPa, and strain in the sheet metal is 8.0e-03. The developed strain lay well enough in the plastic region, which was higher than that of the strain developed with TRD of 30 mm. Besides, the amount of spring-back in the sheet metal reduced with more plastic deformation. Hence, spring-back decreased with an increase in TRD.

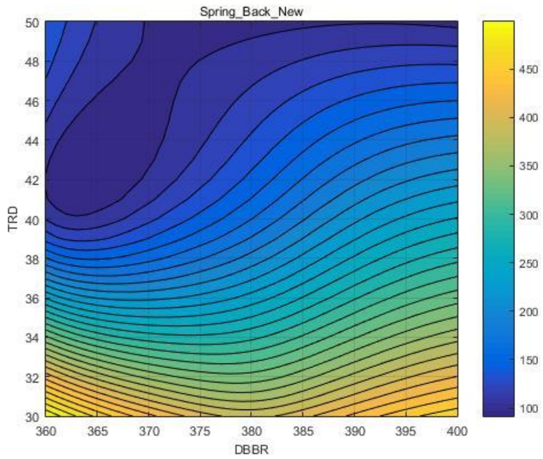

Fig. 6. Effect of top roller displacement (mm) vs distance between bottom rollers (mm) on spring-back (mm)

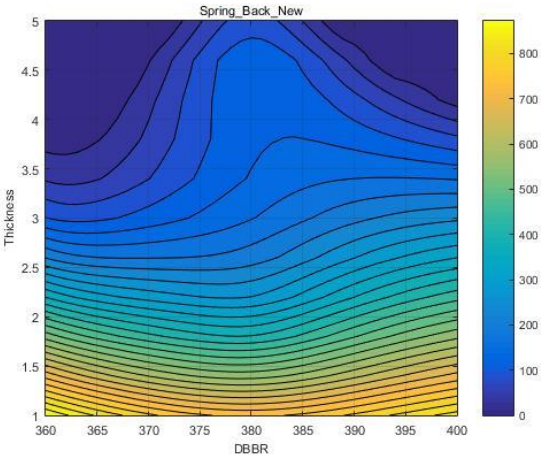

Fig. 7 Effect of the thickness (mm) vs distance between bottom roller (mm) on spring-back (mm)

The amount of spring-back was low for the sheet metal deformed at 40 mm TRD and 360 mm DBBR. As DBBR increased, the amount of spring back also increased. The load applied by the top roller acted over a narrow region in the sheet if the DBBR was less (i.e., 360 mm). Hence, the stress and strain developed in the region were 113.2 MPa and 7.37e-03. With an increase in the load application area (DBBR > 360 mm), the stress-induced was 108.4 MPa, and the strain in the sheet metal was 5.02e-03. Hence, the sheet metal formed at 360 mm DBBR had lesser spring-back than that formed at 400 mm DBBR. A lesser amount of spring-back was observed in the sheet metal that was deformed at low DBBR and high TRD.

The effect of sheet metal thickness and DBBR on the amount of spring-back is shown in Figure 7. The sheet metal of thickness 1 mm deformed at 360 mm DBBR had the highest amount of spring-back. When the DBBR was increased from 360 mm to 380 mm, the amount of spring-back decreased. However, with a further increase in DBBR from 380 mm to 400 mm, the amount of spring back decreased. The amount of spring back reduced with an increase in the thickness of sheet metal. A force of 850 N was exerted on the sheet metal of thickness 5 mm that induced stress of 122.2 MPa and strain 1.10e-02. The developed strain was in the plastic region, as the stress was larger than the yielding stress of 89.5 MPa. Hence, the amount of spring-back was lesser. During deformation, a force of 24 N induced stress of 93.7 MPa and strain of 6.07e-04 in the sheet metal of thickness 1 mm. As the induced stress value was similar to the yielding stress of 89.5 MPa, a large amount of spring-back was observed in the sheet metal of thickness 1 mm than that of sheet metal of thickness 5 mm.

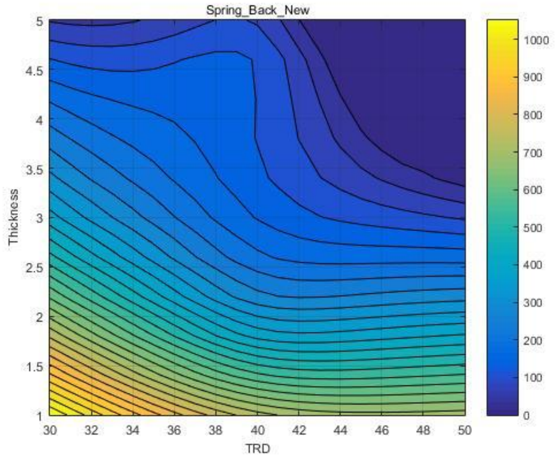

Fig. 8. Effect of thickness (mm) vs top roller displacement (mm) on spring-back (mm)

Tab.4. Optimized values

Sl. No.	Process Parameters	Values
1	Top roller displacement	42 mm
2	Distance between bottom rollers	385 mm
3	Sheet metal thickness	3.5 mm

From Figure 6 and Figure 7, it is observed that DBBR has a less significant effect on the amount of spring-back than that of TRD and sheet metal thickness. However, DBBR behaves uniquely if TRD and thickness of the sheet metal were low. The effect of sheet metal thickness and TRD is shown in Figure 8. It is observed that the amount of spring-back was high for 1 mm sheet metal thickness and 30 mm TRD. As mentioned earlier, the amount of spring-back reduced with an increase in TRD from 30 mm to 50 mm. It is observed that the amount of spring-back was less when the sheet metal thickness was high, and the TRD was high. The optimization results are as shown in Table 4. If the roll forming process is performed at that level of process parameters, the spring-back effect was minimum. The optimization results were successfully validated with the finite element model.

4. CONCLUSION

A finite element model was developed and validated to predict the amount of spring back in the roll forming process for AA5052 alloy. A linear-radial basis function model was developed interrelating the process parameters namely top roller displacement, the distance between bottom rollers, and thickness of the sheet metal with the amount of spring back. The model was utilized to optimize the process parameters to reduce the amount of spring back in the course of the roll forming process of AA5052 alloy. The results demonstrated the following:

- The amount of spring-back increases with an increase in top roller displacement.
- The amount of spring-back decreases with an increase in the thickness of the sheet metal.
- Distance between the bottom rollers has a minor influence on the spring-back effect.

REFERENCES

1. **Abvabi A., Mendiguren J., Rolfe B.F., Weiss M.** (2014), Springback Investigation in Roll Forming of a V-Section, *Applied mechanics and materials*, 553, 643–648.
2. **Ameen H.A.** (2012), Effect of Sheet Thickness and Type of Alloys on the Springback Phenomenon for Cylindrical Die, *American journal of scientific and industrial research*, 480.
3. **Badr O.M., Rolfe B., Zhang P., Weiss M.** (2017), Applying a new constitutive model to analyse the springbackbehaviour of titanium in bending and roll forming, *International Journal of Mechanical Sciences*, 128, 389–400,
4. **Belykh S., Krivenok A., Bormotin K., Stankevich A., Krupskiy R., Mishagin V., Burenin A.** (2016), Numerical and Experimental Study of Multi-Point Forming of Thick Double-Curvature Plates from Aluminum Alloy 7075, *KnE Materials Science*, vol (NA), 17–23.
5. **Davies R., Magee C.** (1977), *The effect of strain rate upon the bending behavior of materials*, ASME, New York.
6. **Fortin P., Bull M., Moore D.** (1983), *An optimized aluminum alloy (x6111) for auto body sheet applications*, SAE Technical Paper.
7. **Gandhi A., Raval H.**, (2006), Article Title, ASME 2006 International Mechanical Engineering Congress and Exposition, *American Society of Mechanical Engineers Digital Collection*, 107–116.
8. **Ghimire S., Emeerith Y., Ghosh R., Ghosh S., Barman R.N.** (2017), Finite Element Analysis of an Aluminium Alloy Sheet in a V-Die Punch Mechanism Considering Spring-Back Effect, *International Journal of Theoretical and Applied Mechanics*, 12, 331–342.
9. **Guo X., Gu Y., Wang H., Jin K., Tao J.** (2018), The Bauschinger effect and mechanical properties of AA5754 aluminum alloy in incremental forming process, *The International Journal of Advanced Manufacturing Technology*, 94, 1387–1396.
10. **Hansen N., Jannerup O.** (1979), *Modelling of elastic-plastic bending of beams using a roller bending machine*, ASME, New York
11. **Hardt D., Roberts M., Stelson K.A.** (1982), *Closed-loop shape control of a roll-bending process*, ASME, New York

12. **Hecker S.** (1975), *Formability of aluminum alloy sheets*, ASME, New York
13. **Hill R.** (1958), A general theory of uniqueness and stability in elastic-plastic solids, *Journal of the Mechanics and Physics of Solids*, 6, 236–249.
14. **Hu J., Marciniak Z., Duncan J.** (2002), *Mechanics of sheet metal forming*, Elsevier, Oxford.
15. **HyperWorks** (2010), *HyperMesh*, Version 11.
16. **HyperWorks** (2014), *Hyperworks* 14.0 RADIOSS reference guide, Altair engineering.
17. **Khamneh M.E., Askari-Paykani M., ShahverdiH,.,Hadavi S.M.M., Emami M.** (2016), Optimization of spring-back in creep age forming process of 7075 Al-Alclad alloy using D-optimal design of experiment method, *Measurement* 88, 278–286,
18. **Ktari A., Antar Z., Haddar N., Elleuch K.** (2012), Modeling and computation of the three-roller bending process of steel sheets, *Journal of mechanical science and technology*, 26, 123–128.
19. **Kumar K.D., Appukuttan K., Neelakantha V., Naik P.S.** (2014), Experimental determination of spring back and thinning effect of aluminum sheet metal during L-bending operation, *Materials & Design*, 56, 613–619.
20. **Lee M.-G., Kim D., Kim C., Wenner M.L., Chung K.** (2005), Spring-back evaluation of automotive sheets based on isotropic–kinematic hardening laws and non-quadratic anisotropic yield functions, part III: applications, *International journal of plasticity*, 21, 915–953.
21. **Liu Y., Wang L., Zhu B., Wang Y., Zhang Y.** (2018), Identification of two aluminum alloys and springback behaviors in cold bending, *Procedia Manufacturing*, 15, 701–708.
22. **Parsa M., Pishbin H., Kazemi M.** (2012), Investigating spring back phenomena in double curved sheet metals forming, *Materials & Design*, 41, 326–337.
23. **Paulsen F., Welo T.** (1996), Application of numerical simulation in the bending of aluminium-alloy profiles, *Journal of Materials Processing Technology*, 58, 274–285.
24. **Ramalingam V.V., Ramasamy P.** (2017), Modelling corrosion behavior of friction stir processed aluminium alloy 5083 using polynomial: radial basis function, *Transactions of the Indian Institute of Metals*, 70, 2575–2589.
25. **Srivastav Y., Shinde S.** (2010), Dynamic Simulation and Analysis of Plate Roll Bending Process for Forming a Cylindrical Shell,*Proceedings of the HyperWorks Technology Conference 2010*, Altair Technology Conference.
26. **Vignesh R.V., Padmanaban R., Datta M.** (2018), Influence of FSP on the microstructure, microhardness, intergranular corrosion susceptibility and wear resistance of AA5083 alloy, *Tribology-Materials, Surfaces & Interfaces*, 12(3), 157–169.
27. **VigneshV., Padmanaban R.** (2018), Modelling of peak temperature during friction stir processing of magnesium alloy AZ91, IOP Conference Series: Materials Science and Engineering, 310(1), 012019.
28. **Westermann I., Snilsberg K.E., Sharifi Z., Hopperstad O.S., Marthinsen K., Holmedal B.** (2011), Three-point bending of heat-treatable aluminum alloys: influence of microstructure and texture on bendability and fracture behavior, *Metallurgical and Materials Transactions*, A 42, 3386–3398.
29. **Xing M.-Z., Wang Y.-G., Jiang Z.-X.** (2013), Dynamic fracture behaviors of selected aluminum alloys under three-point bending, *Defence Technology*, 9, 193–200.
30. **Xu W., Ma C., Li C., Feng W.** (2004), Sensitive factors in springback simulation for sheet metal forming, *Journal of Materials Processing Technology*, 151, 217–222, (2004).
31. **Yang M., Shima S.** (1988), Simulation of pyramid type three-roll bending process, *International Journal of Mechanical Sciences*, 30, 877–886.

Acknowledgment: The authors express their sincere gratitude to Mr. Ashutosh Sinha, Senior Engineer, System Design and Detail Engineering Department, Larsen & Toubro Limited (Defense), Coimbatore for his guidance and support to perform numerical and experimental tests.

sciendo

DOI 10.2478/ama-2020-0020

EFFECT OF KERR FOUNDATION AND IN-PLANE FORCES ON FREE VIBRATION OF FGM NANOBEAMS WITH DIVERSE DISTRIBUTION OF POROSITY

Piotr JANKOWSKI[*]

[*]Faculty of Mechanical Engineering, Bialystok University of Technology, ul. Wiejska 45C, 15-351 Białystok, Poland

p.jankowski@doktoranci.pb.edu.pl

Received 19 June 2020, revised 20 October 2020, accepted 23 October 2020

Abstract: In the present paper, the effect of diverse distribution of functionally graded porous material and Kerr elastic foundation on natural vibrations of nanobeams subjected to in-plane forces is investigated based on the nonlocal strain gradient theory. The displacement field of the nanobeam satisfies assumptions of Reddy higher-order shear deformation beam theory. All the displacements gradients are assumed to be small, then the components of the Green-Lagrange strain tensor are linear and infinitesimal. The constitutive relations for functionally graded (FG) porous material are expressed by nonlocal and length scale parameters and power-law variation of material parameters in conjunction with cosine functions. It created possibility to investigate an effect of functionally graded materials with diverse distribution of porosity and volume of voids on mechanics of structures in nano scale. The Hamilton's variational principle is utilized to derive governing equations of motion of the FG porous nanobeam. Analytical solution to formulated boundary value problem is obtained in closed-form by using Navier solution technique. Validation of obtained results and parametric study are presented in tabular and graphical form. Influence of axial tensile/compressive forces and three different types of porosity distribution as well as stiffness of Kerr foundation on natural frequencies of functionally graded nanobeam is comprehensively studied.

Keywords: Porosity distribution; nanobeam; Reddy beam theory; free vibrations; nonlocal strain gradient theory

1. INTRODUCTION

Recent research and development in nanotechnology have contributed to design devices in nano and micro scale called nanoelectromechanical (NEMS) and microelectromechanical (MEMS) systems (Lyshevski, 2002). NEMS and MEMS may be used in many areas including automotive, aerospace, biotechnology, healthcare, office equipment and telecommunication (Leondes, 2006). Nano and micro devices, depending on requirements, can be manufactured with porous materials (Bhushan, 2004), functionally graded materials (FGMs) (Ashoori et al., 2017) and it commonly takes the form of plates and beams (Lam et al., 2003).

To consider nano/micro size scale effect on structures nonlocal theories have been derived, for instance couple stress theory (Toupin, 1962), modified couple stress theory (Yang et al., 2002), Eringen's nonlocal theory (Eringen and Edelen, 1972; Eringen, 1972), strain gradient theory (Mindlin, 1964, 1965) and nonlocal strain gradient theory (Lim et al., 2015).

The literature survey related to the study of mechanical behavior of nanobeams is conducted to justify the originality of the present paper. The review is divided into two paragraphs: considering the effect of elastic foundation and mechanical response of nanostructures without foundation.

Aydogdu (2008) studied the influence of length to thickness ratio on bending, buckling and free vibrations based on Eringen's nonlocal theory and various beam models. Lim et al. (2010) analyzed the free vibration of axially pre-tensioned nanobeams with various boundary condition according to Eringen's nonlocal elasticity. Sahmani and Ansari (2011) presented buckling analysis with comparison of Euler-Bernoulli, Timoshenko and Levinson beam theory with different boundary condition using Eringen's nonlocal elasticity. Thai (2012) introduced new nonlocal shear deformation beam theory and analyzed the mechanical behavior of simply supported nanobeam. Thai and Vo (2012a) investigated deflection, buckling and free vibrations of nanobeam on the basis of sinusoidal shear deformation theory and nonlocal constitutive relations of Eringen. Eltaher et al. (2012, 2013) used finite element method to investigate free vibration and static buckling behaviors of functionally graded nanobeam based on Euler-Bernoulli model assumptions and Eringen's nonlocal theory. Nazemnezhad and Hosseini-Hashemi (2014) examined the nonlinear free vibrations of FGM Euler-Bernoulli nanobeam using Eringen's nonlocal theory. Şimşek (2014) studied the effect of aspect ratio and Eringen's nonlocal parameter on nonlinear frequency of nanobeam. Rahmani and Jandaghian (2015) conducted buckling analysis of functionally graded nanobeam using Eringen's nonlocal and Reddy beam theories. Li and Hu (2015) examined deflection and buckling of Euler-Bernoulli nanobeam model on the basic of nonlocal strain gradient theory. Şimşek (2016) employed Euler-Bernoulli beam assumptions and nonlocal strain gradient theory to study the nonlinear free vibration of simply supported nanobeam made of functionally graded material. Lu et al. (2017) developed sinusoidal shear deformation beam theory to analyze free vibration problems of simply supported nanobeam using nonlocal strain gradient theory. Shafiei et al. (2017) applied Timoshenko beam model to study the influence of porosity on vibration problems of functionally graded nano and micro beams. Eltaher et al. (2018) presented the finite element method to study the bending and vibrations of functionally graded nanobeam with porosity according to Euler-Bernoulli beam and Eringen's nonlocal theories. Zhang et al. (2019) investigated the influence of Eringen's nonlocal parameter, power index and length to thickness ratio on natural vibrations of functionally graded nanobeam witch various boundary condition.

El-Borgi et al. (2015) considered free and forced vibration of functionally graded nanobeam resting on nonlinear elastic foundation on the basis of Euler-Bernoulli beam model assumptions and Eringen's nonlocal theory. Ghadiri et al. (2017) presented the analytical solution for nonlinear vibrations of functionally graded visco-elastically supported nanobeam subjected to transverse concentrated load. Saffari et al. (2017) studied the free vibration of simply supported FGM nanobeam resting on Winkler-Pasternak foundation based on Timoshenko beam model and Eringen's nonlocal elasticity. Reza Barati (2017) examined the forced vibrations of FGM nanobeam resting on Kerr foundation under hydro-thermal loads on the basis of sinusoidal shear deformation theory and Eringen's nonlocal theory. Lv et al. (2018) analyzed the effect of Winkler foundation and material defects on nonlinear vibrations of FGM Timoshenko nanobeam via nonlocal strain gradient theory. Karami and Janghorban (2019) proposed a new shear deformation theory and analyzed the free vibration of functionally graded nanobeam resting on Winkler-Pasternak foundation using nonlocal strain gradient theory.

The carried out literature review indicates that there does not exist an analysis of effect of stiffness of Kerr foundation and in-plane axial forces on free vibration of FGM nanobeam with diverse distributions of porosity based on the nonlocal strain gradient-based Reddy higher-order shear deformation theory. Unlike other nonlocal models, the utilized nonlocal strain gradient model is a hybrid nonlocal model, which can capture both hardening and softening phenomena in structures in nano scale. For the first time, influences of Kerr elastic foundation, volume of pores, diverse distribution of porosity and functionally graded material as well as both small scale parameters on dynamical response of nanobeams subjected to axial compressive/tensile loads were presented. Additionally, for the first time, comparison of Winkler-Pasternak and Kerr foundation effect on eigenfrequencies of simply-supported FGM nanobeam is shown.

2. DISPLACEMENT AND STRAIN FIELDS

Consider a functionally graded porous nanobeam under an axial in-plane forces $\widehat{N}_{xx}$ and resting on three-parametric foundation. Let L, h and b denote the length, thickness and width of the nanobeam, respectively. The foundation is described by springs stiffness (K_l, K_u) and shear (G) stiffness of layer. The coordinate system (x, z) and cross-section are presented in Fig. 1.

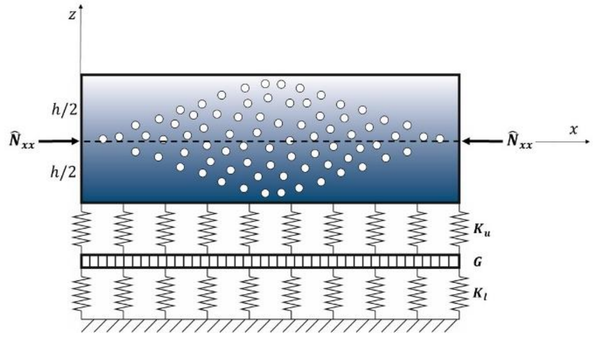

Fig. 1. The geometry and coordinate system of FGM porous nanobeam subjected to in-plane axial forces

Based on the higher-order shear deformation theory, the displacement field of the nanobeam takes the form (Reddy, 2017):

$$u_x(x,z,t) = u_0(x,t) + z\varphi_x(x,t) - c_1 z^3\left(\varphi_x(x,t) + \frac{\partial w_0(x,t)}{\partial x}\right) \tag{1a}$$

$$u_z(x,t) = w_0(x,t) \tag{1b}$$

where u_x and u_z are displacements along x and z directions, respectively. u_0, w_0 and φ_x are unknown generalized displacements. Hence, u_0 and w_0 denote axial and transverse displacement of a material point in the mid-plane $(x, 0)$ in the undeformed configuration at any time t. φ_x is rotation of the point on the centroidal axis x of the beam, and $c_1 = 4/(3h^2)$.

Taking into account the assumptions that all the displacement gradients are very small, consequently, the components of Green-Lagrange strain tensor are linear and infinitesimal. The general forms of strain-displacement relations associated with the displacement field (1) are defined as:

$$\varepsilon_{xx} = \varepsilon_{xx}^{(0)} + z\varepsilon_{xx}^{(1)} + z^3\varepsilon_{xx}^{(3)} \tag{2a}$$

$$2\varepsilon_{xz} = \gamma_{xz}^{(0)} + z^2\gamma_{xz}^{(2)} \tag{2b}$$

where the particular components of the linear strains are:

$$\left\{\varepsilon_{xx}^{(0)}, \varepsilon_{xx}^{(1)}, \varepsilon_{xx}^{(3)}\right\} = \left\{\frac{\partial u_0}{\partial x}, \frac{\partial \varphi_x}{\partial x}, -c_1\left(\frac{\partial \varphi_x}{\partial x} + \frac{\partial^2 w_0}{\partial x^2}\right)\right\} \tag{3a}$$

$$\left\{\gamma_{xz}^{(0)}, \gamma_{xz}^{(2)}\right\} = \left\{\varphi_x + \frac{\partial w_0}{\partial x}, -c_2\left(\varphi_x + \frac{\partial w_0}{\partial x}\right)\right\} \tag{3b}$$

where $c_2 = 3c_1$.

3. CONSTITUTIVE RELATIONS

On the basis of reduced higher-order nonlocal strain gradient theory (Lim et al., 2015) to only one length scale parameter, the constitutive relations of the nanobeam are expressed as:

$$(1 - \mathfrak{B}\nabla^2)\sigma_{xx} = (1 - \ell^2\nabla^2)C_{xx}\varepsilon_{xx} \tag{4a}$$

$$(1 - \mathfrak{B}\nabla^2)\sigma_{xz} = (1 - \ell^2\nabla^2)2C_{xz}\varepsilon_{xz} \tag{4b}$$

where nonlocal parameter $\mathfrak{B} = (e_0 a)^2$ describes nonlocal stress field, material length scale parameter ℓ captures higher-order strain gradient stress field, and $\nabla^2 = \frac{\partial^2}{\partial x^2}$ is the Laplace operator.

Stiffness coefficients of the FGM porous nanobeam are:

$$C_{xx} = E(z) \tag{5a}$$

$$C_{xz} = \frac{E(z)}{2(1+\nu)} \tag{5b}$$

where Poisson's ratio ν is assumed to be constant and Young's modulus $E(z)$ varies through the nanobeam thickness according to the power-law (Kim et al., 2019):

$$E(z) = \left[(E_t - E_b)\left(\frac{z}{h} + \frac{1}{2}\right)^g + E_b\right]\left[1 - \Upsilon(z, \vartheta)\right] \tag{6}$$

where E_t and E_b are Young's modulus at the top $(z = h/2)$ and bottom $(z = -h/2)$ surface, respectively. The constant g is power-law index and $\Upsilon(z, \vartheta)$ is a porosity distribution function. In the present paper, three different types of porosity are considered and written as:

Type 1: $\Upsilon(z,\vartheta)=\vartheta cos\left(\frac{\pi z}{h}\right)$ (7a)

Type 2: $\Upsilon(z,\vartheta)=\vartheta cos\left[\frac{\pi}{2}\left(\frac{z}{h}-\frac{1}{2}\right)\right]$ (7b)

Type 3: $\Upsilon(z,\vartheta)=\vartheta cos\left[\frac{\pi}{2}\left(\frac{z}{h}+\frac{1}{2}\right)\right]$ (7c)

where ϑ is porosity coefficient. Types of porosity distribution through nanobeam thickness is presented in Fig. 2.

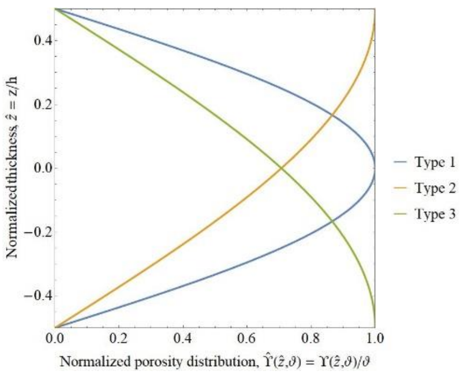

Fig. 2. Normalized distributions of porosity through nanobeam thickness

An example of effect of both power-law index and types of porosity distributions (with constant porosity coefficient value) on the variation of Young's modulus is shown in Fig. 3.

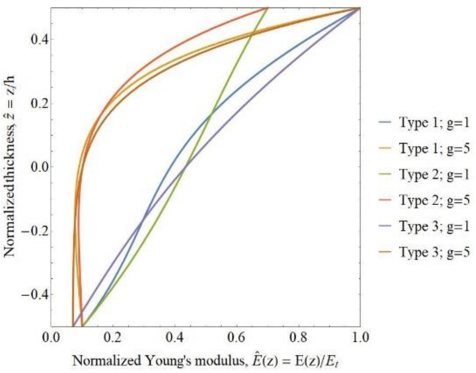

Fig. 3. Variations of Young's modulus through beam thickness depending on power-law index and porosity distribution

Substituting strains (Eq. 2) into equations (4), particular form of constitutive relations are obtained:

$$(1-\mathfrak{B}\nabla^2)\sigma_{xx}=(1-\ell^2\nabla^2)C_{xx}\left[\frac{\partial u_0}{\partial x}+z\frac{\partial\varphi_x}{\partial x}-\mathrm{c}_1z^3\left(\frac{\partial\varphi_x}{\partial x}+\frac{\partial^2w_0}{\partial x^2}\right)\right] \quad (8a)$$

$$(1-\mathfrak{B}\nabla^2)\sigma_{xz}=(1-\ell^2\nabla^2)C_{xz}\left[\varphi_x+\frac{\partial w_0}{\partial x}-\mathrm{c}_2z^2\left(\varphi_x+\frac{\partial w_0}{\partial x}\right)\right] \quad (8b)$$

4. EQUATIONS OF MOTION

Equations of motion of the nanobeam are derived based on the dynamic version of Hamilton principle (Reddy, 2017):

$$\int_0^T(\delta\mathcal{U}-\delta\mathcal{K}+\delta\mathcal{V})dt=0 \quad (9)$$

The quantities $\delta\mathcal{U}$, $\delta\mathcal{K}$ and $\delta\mathcal{V}$ are the virtual strain energy, kinetic energy and work done by external forces, respectively. Each virtual energy and the virtual work are defined as:

$$\delta\mathcal{U}=\int_0^L\int_A(\sigma_{xx}\delta\varepsilon_{xx}+2\sigma_{xz}\delta\varepsilon_{xz})dA\,dx \quad (10a)$$

$$\delta\mathcal{K}=\int_0^L\int_A\rho(z)(\dot{u}_x\delta\dot{u}_x+\dot{u}_z\delta\dot{u}_z)dA\,dx \quad (10b)$$

$$\delta\mathcal{V}=-\int_L\left[\widehat{N}_{xx}\frac{\partial w_0}{\partial x}\frac{\partial\delta w_0}{\partial x}+F_f\delta w_0\right]dz \quad (10c)$$

where $dA=bdz$, $\widehat{N}_{xx}$ are the axial in-plane compressive/tensile forces, F_f denotes a reaction of elastic foundation, and $\rho(z)$ is the mass density of the FGM porous nanobeam

$$\rho(z)=\left[(\rho_t-\rho_b)\left(\frac{z}{h}+\frac{1}{2}\right)^g+\rho_b\right][1-\Upsilon(z,\vartheta)] \quad (11)$$

that varies from a value at the bottom surface ρ_b to a value at the top surface ρ_t.

The particular form of the strain energy (Eq. 10a) is presented below:

$$\delta\mathcal{U}=\int_0^L\left[N_{xx}\frac{\partial\delta u_0}{\partial x}+M_{xx}\frac{\partial\delta\varphi_x}{\partial x}-\mathrm{c}_1P_{xx}\left(\frac{\partial\delta\varphi_x}{\partial x}+\frac{\partial^2\delta w_0}{\partial x^2}\right)+N_{xz}\left(\delta\varphi_x+\frac{\partial\delta w_0}{\partial x}\right)-\mathrm{c}_2R_{xz}\left(\delta\varphi_x+\frac{\partial\delta w_0}{\partial x}\right)\right]dx \quad (12)$$

where introduced thickness-integrated forces and moments take the following form:

$$\{N_{xx},M_{xx},P_{xx}\}=b\int_{-h/2}^{h/2}\sigma_{xx}\{1,z,z^3\}dz \quad (13a)$$

$$\{N_{xz},R_{xz}\}=b\int_{-h/2}^{h/2}\sigma_{xz}\{1,z^2\}dz \quad (13b)$$

The final form of virtual kinetic energy (Eq. 10b) is expressed as:

$$\delta\mathcal{K}=\int_0^L I_0(\dot{u}_0\delta\dot{u}_0+\dot{w}_0\delta\dot{w}_0)+I_1(\dot{u}_0\delta\dot{\varphi}_x+\dot{\varphi}_x\delta\dot{u}_0)+I_2(\dot{\varphi}_x\delta\dot{\varphi}_x)-\mathrm{c}_1I_3\left(\dot{u}_0\delta\dot{\varphi}_x+\dot{u}_0\frac{\partial\delta\dot{w}_0}{\partial x}+\dot{\varphi}_x\delta\dot{u}_0+\frac{\partial\dot{w}_0}{\partial x}\delta\dot{u}_0\right)-\mathrm{c}_1I_4\left(\dot{\varphi}_x\delta\dot{\varphi}_x+\dot{\varphi}_x\frac{\partial\delta\dot{w}_0}{\partial x}+\dot{\varphi}_x\delta\dot{\varphi}_x+\frac{\partial\dot{w}_0}{\partial x}\delta\dot{\varphi}_x\right)+\mathrm{c}_1^2I_6\left(\dot{\varphi}_x\delta\dot{\varphi}_x+\dot{\varphi}_x\frac{\partial\delta\dot{w}_0}{\partial x}+\frac{\partial\dot{w}_0}{\partial x}\delta\dot{\varphi}_x+\frac{\partial\dot{w}_0}{\partial x}\frac{\partial\delta\dot{w}_0}{\partial x}\right)dx \quad (14)$$

where introduced mass inertias are defined as:

$$I_i=b\int_{-h/2}^{h/2}\rho(z)z^idz\ \ \wedge\ \ i\in\langle 0,6\rangle \quad (15)$$

The particular form of work done by external forces (Eq. 10c) takes the form:

$$\delta\mathcal{V}=-\int_L\left[-\widehat{N}_{xx}\frac{\partial^2w_0}{\partial x^2}\delta w_0+F_f\delta w_0\right]dz \quad (16)$$

The reaction of foundation is modeled as Kerr foundation (Kerr, 1965):

$$F_f\equiv F_k=-\left(\frac{K_lK_u}{K_l+K_u}\right)w_0+\left(\frac{GK_u}{K_l+K_u}\right)\frac{\partial^2w_0}{\partial x^2} \quad (17)$$

with lower K_l and upper K_u spring stiffness coefficients. G represents stiffness of shear layer.

Removing upper spring, the model is simplified to Winkler-Pasternak foundation (Pasternak, 1954):

$$F_f\equiv F_P=-K_ww_0+K_s\frac{\partial^2w_0}{\partial x^2} \quad (18)$$

DOI 10.2478/ama-2020-0020

where K_w and K_s are spring and shear stiffness coefficient, respectively.

Further simplification by removing shear layer leads to Winkler model of foundation:

$$F_f \equiv F_W = -K_w w_0 \tag{19}$$

Derived equations of motion for macro-scale FGM porous beam are expressed as:

$$\delta u_0: \frac{\partial N_{xx}}{\partial x} = I_0 \ddot{u}_0 + I_1 \ddot{\varphi}_x - \mathrm{c}_1 I_3 \left(\ddot{\varphi}_x + \frac{\partial \ddot{w}_0}{\partial x}\right) \tag{20a}$$

$$\delta \varphi_x: \frac{\partial M_{xx}}{\partial x} - \mathrm{c}_1 \frac{\partial P_{xx}}{\partial x} - N_{xz} + \mathrm{c}_2 R_{xz} = I_1 \ddot{u}_0 + I_2 \ddot{\varphi}_x - \mathrm{c}_1 I_3 \ddot{u}_0 - \mathrm{c}_1 I_4 \left(2\ddot{\varphi}_x + \frac{\partial \ddot{w}_0}{\partial x}\right) + \mathrm{c}_1^2 I_6 \left(\ddot{\varphi}_x + \frac{\partial \ddot{w}_0}{\partial x}\right) \tag{20b}$$

$$\delta w_0: \mathrm{c}_1 \frac{\partial^2 P_{xx}}{\partial x^2} + \frac{\partial N_{xz}}{\partial x} - \mathrm{c}_2 \frac{\partial R_{xz}}{\partial x} - \widehat{N}_{xx} \frac{\partial^2 w_0}{\partial x^2} + \left(\frac{K_l K_u}{K_l + K_u}\right) w_0 - \left(\frac{G K_u}{K_l + K_u}\right) \frac{\partial^2 w_0}{\partial x^2} = I_0 \ddot{w}_0 + \mathrm{c}_1 I_3 \frac{\partial \ddot{u}_0}{\partial x} + \mathrm{c}_1 I_4 \frac{\partial \ddot{\varphi}_x}{\partial x} - \mathrm{c}_1^2 I_6 \left(\frac{\partial \ddot{\varphi}_x}{\partial x} + \frac{\partial^2 \ddot{w}_0}{\partial x^2}\right) \tag{20c}$$

Substituting particular form of constitutive equations (Eq. 8) into thickness-integrated forces and moments (Eq. 13) in order to obtain nonlocal forces and moments in final nonlocal forms:

$$(1 - \mathfrak{B}\nabla^2) N_{xx} = (1 - \ell^2 \nabla^2) \left[A_{xx}^{(0)} \frac{\partial u_0}{\partial x} + A_{xx}^{(1)} \frac{\partial \varphi_x}{\partial x} - \mathrm{c}_1 A_{xx}^{(3)} \left(\frac{\partial \varphi_x}{\partial x} + \frac{\partial^2 w_0}{\partial x^2}\right)\right] \tag{21a}$$

$$(1 - \mathfrak{B}\nabla^2) M_{xx} = (1 - \ell^2 \nabla^2) \left[A_{xx}^{(1)} \frac{\partial u_0}{\partial x} + A_{xx}^{(2)} \frac{\partial \varphi_x}{\partial x} - \mathrm{c}_1 A_{xx}^{(4)} \left(\frac{\partial \varphi_x}{\partial x} + \frac{\partial^2 w_0}{\partial x^2}\right)\right] \tag{21b}$$

$$(1 - \mathfrak{B}\nabla^2) P_{xx} = (1 - \ell^2 \nabla^2) \left[A_{xx}^{(3)} \frac{\partial u_0}{\partial x} + A_{xx}^{(4)} \frac{\partial \varphi_x}{\partial x} - \mathrm{c}_1 A_{xx}^{(6)} \left(\frac{\partial \varphi_x}{\partial x} + \frac{\partial^2 w_0}{\partial x^2}\right)\right] \tag{21c}$$

$$(1 - \mathfrak{B}\nabla^2) N_{xz} = (1 - \ell^2 \nabla^2) \left[A_{xz}^{(0)} \left(\varphi_x + \frac{\partial w_0}{\partial x}\right) - \mathrm{c}_2 A_{xz}^{(2)} \left(\varphi_x + \frac{\partial w_0}{\partial x}\right)\right] \tag{21d}$$

$$(1 - \mathfrak{B}\nabla^2) R_{xz} = (1 - \ell^2 \nabla^2) \left[A_{xz}^{(2)} \left(\varphi_x + \frac{\partial w_0}{\partial x}\right) - \mathrm{c}_2 A_{xz}^{(4)} \left(\varphi_x + \frac{\partial w_0}{\partial x}\right)\right] \tag{21e}$$

where resultant stiffness coefficients are obtained as:

$$\left\{A_{xx}^{(0)}, A_{xx}^{(1)}, A_{xx}^{(2)}, A_{xx}^{(3)}, A_{xx}^{(4)}, A_{xx}^{(6)}\right\} = b \int_{-h/2}^{h/2} C_{xx} \{1, z, z^2, z^3, z^4, z^6\} dz \tag{22a}$$

$$\left\{A_{xz}^{(0)}, A_{xz}^{(2)}, A_{xz}^{(4)}\right\} = b \int_{-h/2}^{h/2} C_{xz} \{1, z^2, z^4\} dz \tag{22b}$$

Substituting nonlocal forces and moments (Eq. 21) into equations of motion (Eq. 19), three equations of motion of the nanobeam expressed by displacements are derived in the form:

$$A_{xx}^{(0)} \frac{\partial^2 u_0}{\partial x^2} + A_{xx}^{(1)} \frac{\partial^2 \varphi_x}{\partial x^2} - \mathrm{c}_1 A_{xx}^{(3)} \left(\frac{\partial^2 \varphi_x}{\partial x^2} + \frac{\partial^3 w_0}{\partial x^3}\right) - \ell^2 \left[A_{xx}^{(0)} \frac{\partial^4 u_0}{\partial x^4} + A_{xx}^{(1)} \frac{\partial^4 \varphi_x}{\partial x^4} - \mathrm{c}_1 A_{xx}^{(3)} \left(\frac{\partial^4 \varphi_x}{\partial x^2} + \frac{\partial^5 w_0}{\partial x^3}\right)\right] = I_0 \ddot{u}_0 + I_1 \ddot{\varphi}_x - \mathrm{c}_1 I_3 \left(\ddot{\varphi}_x + \frac{\partial \ddot{w}_0}{\partial x}\right) - \mathfrak{B} \left[I_0 \frac{\partial^2 \ddot{u}_0}{\partial x^2} + I_1 \frac{\partial^2 \ddot{\varphi}_x}{\partial x^2} - \mathrm{c}_1 I_3 \left(\frac{\partial^2 \ddot{\varphi}_x}{\partial x^2} + \frac{\partial^3 \ddot{w}_0}{\partial x^3}\right)\right] \tag{23a}$$

$$-A_{xz}^{(0)} \left(\varphi_x + \frac{\partial w_0}{\partial x}\right) + 2\mathrm{c}_2 A_{xz}^{(2)} \left(\varphi_x + \frac{\partial w_0}{\partial x}\right) - \mathrm{c}_2^2 A_{xz}^{(4)} \left(\varphi_x + \frac{\partial w_0}{\partial x}\right) + A_{xx}^{(1)} \frac{\partial^2 u_0}{\partial x^2} - \mathrm{c}_1 A_{xx}^{(3)} \frac{\partial^2 u_0}{\partial x^2} + A_{xx}^{(2)} \frac{\partial^2 \varphi_x}{\partial x^2} - \mathrm{c}_1 A_{xx}^{(4)} \frac{\partial^2 \varphi_x}{\partial x^2} - \mathrm{c}_1 A_{xx}^{(4)} \left(\frac{\partial^2 \varphi_x}{\partial x^2} + \frac{\partial^3 w_0}{\partial x^3}\right) + \mathrm{c}_1^2 A_{xx}^{(6)} \left(\frac{\partial^2 \varphi_x}{\partial x^2} + \frac{\partial^3 w_0}{\partial x^3}\right) - \ell^2 \left[-A_{xz}^{(0)} \left(\frac{\partial^2 \varphi_x}{\partial x^2} + \frac{\partial^3 w_0}{\partial x^3}\right) + 2\mathrm{c}_2 A_{xz}^{(2)} \left(\frac{\partial^2 \varphi_x}{\partial x^2} + \frac{\partial^3 w_0}{\partial x^3}\right) - \mathrm{c}_2^2 A_{xz}^{(4)} \left(\frac{\partial^2 \varphi_x}{\partial x^2} + \frac{\partial^3 w_0}{\partial x^3}\right) + A_{xx}^{(1)} \frac{\partial^4 u_0}{\partial x^4} - \mathrm{c}_1 A_{xx}^{(3)} \frac{\partial^4 u_0}{\partial x^4} + A_{xx}^{(2)} \frac{\partial^4 \varphi_x}{\partial x^4} - \mathrm{c}_1 A_{xx}^{(4)} \frac{\partial^4 \varphi_x}{\partial x^4} - \mathrm{c}_1 A_{xx}^{(4)} \left(\frac{\partial^4 \varphi_x}{\partial x^4} + \frac{\partial^5 w_0}{\partial x^5}\right) + \mathrm{c}_1^2 A_{xx}^{(6)} \left(\frac{\partial^4 \varphi_x}{\partial x^4} + \frac{\partial^5 w_0}{\partial x^5}\right)\right] = I_1 \ddot{u}_0 - \mathrm{c}_1 I_3 \ddot{u}_0 + I_2 \ddot{\varphi}_x + \mathrm{c}_1^2 I_6 \left(\ddot{\varphi}_x + \frac{\partial \ddot{w}_0}{\partial x}\right) - \mathrm{c}_1 I_4 \left(2\ddot{\varphi}_x + \frac{\partial \ddot{w}_0}{\partial x}\right) - \mathfrak{B} \left[I_1 \frac{\partial^2 \ddot{u}_0}{\partial x^2} - \mathrm{c}_1 I_3 \frac{\partial^2 \ddot{u}_0}{\partial x^2} + I_2 \frac{\partial^2 \ddot{\varphi}_x}{\partial x^2} + \mathrm{c}_1^2 I_6 \left(\frac{\partial^2 \ddot{\varphi}_x}{\partial x^2} + \frac{\partial^3 \ddot{w}_0}{\partial x^3}\right) - \mathrm{c}_1 I_4 \left(2 \frac{\partial^2 \ddot{\varphi}_x}{\partial x^2} + \frac{\partial^3 \ddot{w}_0}{\partial x^3}\right)\right] \tag{23b}$$

$$c_1 A_{xx}^{(3)} \frac{\partial^3 u_0}{\partial x^3} + A_{xz}^{(0)} \left(\frac{\partial \varphi_x}{\partial x} + \frac{\partial^2 w_0}{\partial x^2}\right) - 2c_2 A_{xz}^{(2)} \left(\frac{\partial \varphi_x}{\partial x} + \frac{\partial^2 w_0}{\partial x^2}\right) + c_2^2 A_{xz}^{(4)} \left(\frac{\partial \varphi_x}{\partial x} + \frac{\partial^2 w_0}{\partial x^2}\right) + c_1 A_{xx}^{(4)} \frac{\partial^3 \varphi_x}{\partial x^3} - c_1^2 A_{xx}^{(6)} \left(\frac{\partial^3 \varphi_x}{\partial x^3} + \frac{\partial^4 w_0}{\partial x^4}\right) - \ell^2 \left[c_1 A_{xx}^{(3)} \frac{\partial^5 u_0}{\partial x^5} + A_{xz}^{(0)} \left(\frac{\partial^3 \varphi_x}{\partial x^3} + \frac{\partial^4 w_0}{\partial x^4}\right) - 2c_2 A_{xz}^{(2)} \left(\frac{\partial^3 \varphi_x}{\partial x^3} + \frac{\partial^4 w_0}{\partial x^4}\right) + c_2^2 A_{xz}^{(4)} \left(\frac{\partial^3 \varphi_x}{\partial x^3} + \frac{\partial^4 w_0}{\partial x^4}\right) + c_1 A_{xx}^{(4)} \frac{\partial^5 \varphi_x}{\partial x^5} - c_1^2 A_{xx}^{(6)} \left(\frac{\partial^5 \varphi_x}{\partial x^5} + \frac{\partial^6 w_0}{\partial x^6}\right)\right] = I_0 \ddot{w}_0 + c_1 I_3 \frac{\partial \ddot{u}_0}{\partial x} + c_1 I_4 \frac{\partial \ddot{\varphi}_x}{\partial x} - c_1^2 I_6 \left(\frac{\partial \ddot{\varphi}_x}{\partial x} + \frac{\partial^2 \ddot{w}_0}{\partial x^2}\right) + \widehat{N}_{xx} \frac{\partial^2 w_0}{\partial x^2} + \frac{K_l K_u}{K_l + K_u} w_0 - \frac{G K_u}{K_l + K_u} \frac{\partial^2 w_0}{\partial x^2} - \mathfrak{B} \left[I_0 \frac{\partial^2 \ddot{w}_0}{\partial x^2} + c_1 I_3 \frac{\partial^3 \ddot{u}_0}{\partial x^3} + c_1 I_4 \frac{\partial^3 \ddot{\varphi}_x}{\partial x^3} - c_1^2 I_6 \left(\frac{\partial^3 \ddot{\varphi}_x}{\partial x^3} + \frac{\partial^4 \ddot{w}_0}{\partial x^4}\right) + \widehat{N}_{xx} \frac{\partial^4 w_0}{\partial x^4} + \frac{K_l K_u}{K_l + K_u} \frac{\partial^2 w_0}{\partial x^2} - \frac{G K_u}{K_l + K_u} \frac{\partial^4 w_0}{\partial x^4}\right] \tag{23c}$$

5. SOLUTION OF THE PROBLEM

Analytical solution for simply supported FGM porous nanobeam is derived using Navier solution technique. The generalized displacements are expanded in trigonometric series in form of:

$$\begin{pmatrix} u_0 \\ \varphi_x \\ w_0 \end{pmatrix} = \sum_{n=1}^{\infty} \begin{pmatrix} \bar{u} \cos(\beta_n x) e^{i\omega_n t} \\ \bar{\varphi} \cos(\beta_n x) e^{i\omega_n t} \\ \bar{w} \sin(\beta_n x)\, e^{i\omega_n t} \end{pmatrix} \wedge \quad \beta_n = \frac{n\pi}{L} \tag{24}$$

where $\bar{u}$, $\bar{\varphi}$, $\bar{w}$ are maximum values of displacements and ω_n is natural frequency of the n-th mode.

The system of three governing equations for free vibration analysis is defined as:

$$\{[K] - \omega_n^2 [M]\}\{\Delta\} = 0 \tag{25}$$

where $[K]$ and $[M]$ are stiffness and inertia matrices with size 3x3, and Δ are displacements in vector form:

$$\{\Delta\} = [\bar{u}\ \bar{\varphi}\ \bar{w}]^T \tag{26}$$

Stiffness and inertia matrices are symmetric $(\mathrm{K_{ij}} = \mathrm{K_{ji}}, \mathrm{M_{ij}} = \mathrm{M_{ji}})$. Coefficients of these matrices are obtained as:

$$K_{11} = -A_{xx}^{(0)} \beta_n^2 - \ell^2 A_{xx}^{(0)} \beta_n^4 \tag{27a}$$

$$K_{12} = -A_{xx}^{(1)} \beta_n^2 + \mathrm{c}_1 A_{xx}^{(3)} \beta_n^2 + \ell^2 \left(-A_{xx}^{(1)} \beta_n^4 + \mathrm{c}_1 A_{xx}^{(3)} \beta_n^4\right) \tag{27b}$$

$$K_{13} = \mathrm{c}_1 A_{xx}^{(3)} \beta_n^3 + \ell^2 \mathrm{c}_1 A_{xx}^{(3)} \beta_n^5 \tag{27c}$$

$$K_{22} = -A_{xz}^{(0)} + 2\mathrm{c}_2 A_{xz}^{(2)} - \mathrm{c}_2^2 A_{xz}^{(4)} - A_{xx}^{(2)}\beta_n^2 + 2\mathrm{c}_1 A_{xx}^{(4)}\beta_n^2 - \mathrm{c}_1^2 A_{xx}^{(6)}\beta_n^2 + \ell^2\left(-A_{xz}^{(0)}\beta_n^2 + 2\mathrm{c}_2 A_{xz}^{(2)}\beta_n^2 - \mathrm{c}_2^2 A_{xz}^{(4)}\beta_n^2 - A_{xx}^{(2)}\beta_n^4 + 2\mathrm{c}_1 A_{xx}^{(4)}\beta_n^4 - \mathrm{c}_1^2 A_{xx}^{(6)}\beta_n^4\right) \tag{27d}$$

$$K_{23} = -A_{xz}^{(0)}\beta_n + 2\mathrm{c}_2 A_{xz}^{(2)}\beta_n - \mathrm{c}_2^2 A_{xz}^{(4)}\beta_n + \mathrm{c}_1 A_{xx}^{(4)}\beta_n^3 - \mathrm{c}_1^2 A_{xx}^{(6)}\beta_n^3 + \ell^2\left(-A_{xz}^{(0)}\beta_n^3 + 2\mathrm{c}_2 A_{xz}^{(2)}\beta_n^3 - \mathrm{c}_2^2 A_{xz}^{(4)}\beta_n^3 + \mathrm{c}_1 A_{xx}^{(4)}\beta_n^5 - \mathrm{c}_1^2 A_{xx}^{(6)}\beta_n^5\right) \tag{27e}$$

$$K_{33} = -A_{xz}^{(0)}\beta_n^2 + 2\mathrm{c}_2 A_{xz}^{(2)}\beta_n^2 - \mathrm{c}_2^2 A_{xz}^{(4)}\beta_n^2 - \mathrm{c}_1^2 A_{xx}^{(6)}\beta_n^4 + \ell^2\left(-A_{xz}^{(0)}\beta_n^4 + 2\mathrm{c}_2 A_{xz}^{(2)}\beta_n^4 - \mathrm{c}_2^2 A_{xz}^{(4)}\beta_n^4 - \mathrm{c}_1^2 A_{xx}^{(6)}\beta_n^6\right) - \frac{K_l K_u}{K_l + K_u} - \frac{G K_u}{K_l + K_u}\beta_n^2 + \widehat{N}_{xx}\beta_n^2 + \mathfrak{B}\left(\frac{K_l K_u}{K_l + K_u}\beta_n^2 - \frac{G K_u}{K_l + K_u}\beta_n^4 + \widehat{N}_{xx}\beta_n^4\right) \tag{27f}$$

$$M_{11} = -I_0 - \mathfrak{B} I_0 \beta_n^2 \tag{28a}$$

$$M_{12} = -I_1 + \mathrm{c}_1 I_3 + \mathfrak{B}(-I_1\beta_n^2 + \mathrm{c}_1 I_3 \beta_n^2) \tag{28b}$$

$$M_{13} = \mathrm{c}_1 I_3 \beta_n + \mathfrak{B}\mathrm{c}_1 I_3 \beta_n^3 \tag{28c}$$

$$M_{22} = -I_2 + 2\mathrm{c}_1 I_4 - \mathrm{c}_1^2 I_6 + \mathfrak{B}(-I_2\beta_n^2 + 2\mathrm{c}_1 I_4 \beta_n^2 - \mathrm{c}_1^2 I_6 \beta_n^2) \tag{28d}$$

$$M_{23} = \mathrm{c}_1 I_4 \beta_n - \mathrm{c}_1^2 I_6 \beta_n + \mathfrak{B}(\mathrm{c}_1 I_4 \beta_n^3 - \mathrm{c}_1^2 I_6 \beta_n^3) \tag{28e}$$

$$M_{33} = -I_0 - \mathrm{c}_1^2 I_6 \beta_n^2 + \mathfrak{B}(-I_0\beta_n^2 - \mathrm{c}_1^2 I_6 \beta_n^4) \tag{28f}$$

6. RESULTS AND DISCUSSION

Free vibration analysis of FGM porous nanobeam with simply supported edges is conducted in the present section. Firstly, the comparison of obtained numerical results with results from the literature is shown to verify the correctness of the present model. Then, the free vibration analysis of functionally graded porous nanobeam is presented in the following subsection.

6.1. Verification

Eigenfrequencies for functionally graded beam are compared with results on the basis of sinusoidal shear deformation theory (Thai and Vo, 2012b) and presented in Table 1. The parameters $L = 10\,m$, $\upsilon = 0.3$, $E_1 = 380\,GPa$, $E_2 = 70\,GPa$, $\rho_1 = 3960\,kg/m^3$, $\rho_2 = 2702\,kg/m^3$ were applied to obtain the results.

Tab. 1. Dimensionless natural frequency $\overline{\omega} = \sqrt{\omega}\sqrt[4]{\frac{L^4 \rho A}{EI_2}}$ of simply supported beam

L/h	g	Thai and Vo (2012b)	Present
5	0	5.1531	5.1528
	1	3.9907	3.9904
	2	3.6263	3.6264
	5	3.3998	3.4012
20	0	5.4603	5.4603
	1	4.2051	4.2051
	2	3.8361	3.8361
	5	3.6485	3.6485

Table 2 presents the comparison of calculated first three modes of free vibrations with results obtained based on sinusoidal shear deformation theory and nonlocal strain gradient theory (Lu et al., 2017). The following parameters were used to obtain the numerical results: $L = 10\,nm$, $L/h = 10$, $\upsilon = 0.3$, $E = 30\,MPa$, $\rho = 1\,kg/m^3$.

Tab. 2. First three modes of dimensionless natural frequency $\overline{\omega}_n = \omega_n L^2 \sqrt{\frac{I_0}{EI_2}}$ of simply supported nanobeam

ω_n	$\mathfrak{B}$	ℓ/h	Lu et al. (2017)	Present
ω_1	0	0	9.7077	9.7075
	1		9.2614	9.2612
	4		8.2198	8.2197
	0	0.5	9.8267	9.8266
	1		9.3750	9.3748
	4		8.3206	8.3205
	0	1	10.1755	10.1753
	1		9.7077	9.7075
	4		8.6159	8.6158
ω_2	0	0	37.1009	37.0981
	1		31.4146	31.4122
	4		23.1019	23.1001
	0	0.5	38.8887	38.8857
	1		32.9283	32.9258
	4		24.2151	24.2133
	0	1	43.8165	43.8132
	1		37.1009	37.0981
	4		27.2835	27.2815
ω_3	0	0	78.1855	78.1719
	1		56.8977	56.8878
	4		36.6416	36.6353
	0	0.5	86.4318	86.4168
	1		62.8988	62.8879
	4		40.5062	40.4992
	0	1	107.4379	107.4190
	1		78.1855	78.1719
	4		50.3508	50.3420

Tab. 3. Dimensionless natural frequency $\overline{\omega} = \sqrt{\omega}\sqrt[4]{\frac{L^4 \rho A}{EI_2}}$ of simply supported beam

$\overline{K}_w$	$\frac{\overline{K}_s}{\pi^2}$	Karami and Janghorban (2019)	Present
0	0	3.216341	3.216341
	0.5	3.532519	3.532519
	1	3.781208	3.781208
	2.5	4.326928	4.326928
10^2	0	3.793132	3.793132
	0.5	3.998874	3.998874
	1	4.177015	4.177015
	2.5	4.607107	4.607107
10^4	0	10.02651	10.02651
	0.5	10.03856	10.03856
	1	10.05058	10.05058
	2.5	10.08636	10.08636

DOI 10.2478/ama-2020-0020

Table 3 contains the comparison of fundamental frequency of homogeneous macro-sized beam resting on Winkler-Pasternak foundation (Karami and Janghorban, 2019). We have not found any numerical results in tabular form for nanobeam resting on Kerr foundation. Winkler-Pasternak stiffness coefficients are dimensionless, and takes the form: $\overline{K}_w = K_w \frac{L^4}{EI_2}$, $\overline{K}_s = K_s \frac{L^2}{EI_2}$. Numerical results are obtained for the following parameters: $L = 10\,m$, $L/h = 120$, $\upsilon = 0.3$, $E = 30\,MPa$, $\rho = 1\,kg/m^3$, $C_{xx} = \frac{E(z)}{1-\upsilon^2}$.

It can be concluded, from Tables 1–3 that the numerical results from the present model are in good agreement with the results from the previous papers.

6.2. Free vibration analysis

In the present subsection, free vibrations analysis is conducted for simply supported FGM nanobeam with diverse porosity distributions. In the study, geometrical and material properties are assumed as constant: length $L = 50\,nm$, constant thickness $h = 10\,nm$ and unit width b. Young's moduli take values $E_t = 380\,GPa, E_b = 70\,GPa$, densities $\rho_t = 3100\,kg/m^3$, $\rho_b = 2700\,kg/m^3$ and constant Poisson's ratio $\upsilon = 0.3$. During investigation, the power-law index is assumed to be constant $g\ = 2$.

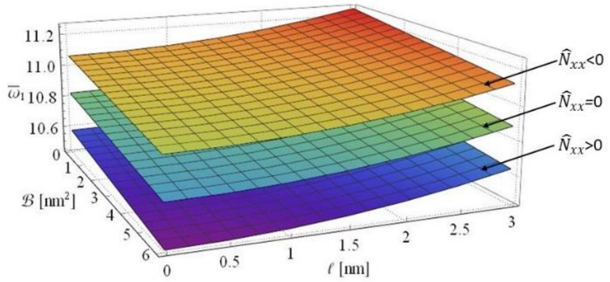

Fig. 4. Effect of nonlocal parameter $\mathfrak{B}$ and length scale parameter ℓ in conjunction with compressive/tensile forces on dimensionless fundamental frequencies of FGM nanobeam

Figure 4 presents the influence of nonlocal parameters $\mathfrak{B}$, ℓ on dimensionless fundamental frequencies $\left(\overline{\omega}_1 = 10^2 \cdot \omega_1 L^2 \sqrt{I_0/E_t I_2}\right)$ of FGM nanobeam without porosity. The figure shows softening (increasing nonlocal parameter $\mathfrak{B}$) and hardening (increasing length scale parameter ℓ) effects according to Eringen's nonlocal theory and Mindlin's strain gradient theory, respectively. The figure also shows the dependence of axial in-plane compressive $\left(\widehat{N}_{xx} > 0\right)$ and tensile $\left(\widehat{N}_{xx} < 0\right)$ forces on dimensionless natural frequencies. Applied compressive forces cause weakening of the structure stiffness, in consequence, its eigenfrequencies decrease. Opposite phenomenon may be observed for tensile force. Nanobeam stiffness increases, thus its fundamental frequencies increase. The phenomena are similar to situations observed by Timoshenko and Woinowsky-Krieger (1959) in bending of rectangular plates subjected to compressive/tensile axial in-plane forces.

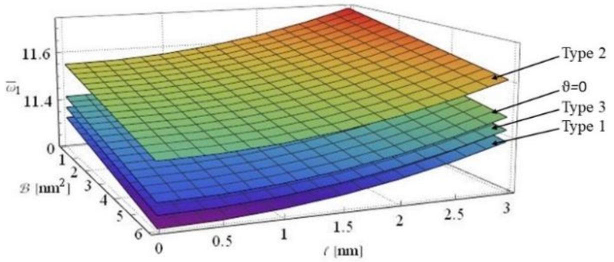

Fig. 5. Effect of nonlocal parameter $\mathfrak{B}$ and length scale parameter ℓ in conjunction with diverse porosity types on dimensionless fundamental frequencies of FGM nanobeam under tensile forces

Natural frequencies for FGM nanobeam subjected to tensile forces without porosity and with diverse porosity types (with porosity coefficient $\vartheta = 0.3$) are presented in Figure 5. Based on the material properties' variation (Fig. 3) and porosity distribution (Fig. 2), it can be observed that porosity Type 1 and Type 3 have similar influence on the response of structure. Porosity causes the structures to become lighter and softer, and consequently, dimensionless fundamental frequencies decrease for Type 1 and Type 3. Ratio of mass to stiffness of FGM nanobeam for Type 2 (porosity accumulated at the bottom surface with lower value of Young's modulus) is higher than for structure without porosity, therefore, fundamental frequencies are also higher.

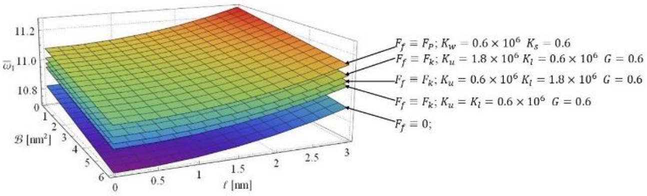

Fig. 6. Effect of nonlocal parameter $\mathfrak{B}$ and length scale parameter ℓ in conjunction with reaction of foundation on dimensionless fundamental frequencies of FGM nanobeam

Figure 6 shows the comparison of Winkler-Pasternak and Kerr foundations effects on eigenfrequencies of FGM nanobeam without porosity. It is clearly observed that the foundation effect causes the whole vibrational system to become stiffer, and thus, natural frequencies increase. Fundamental frequencies of nanobeam resting on Kerr foundation are lower in comparison to Winkler-Pasternak foundation with the same springs and shear moduli stiffnesses. Nevertheless, Kerr foundation, due to more parameters, gives an opportunity to more precisely control the dynamic behavior of the nanobeam.

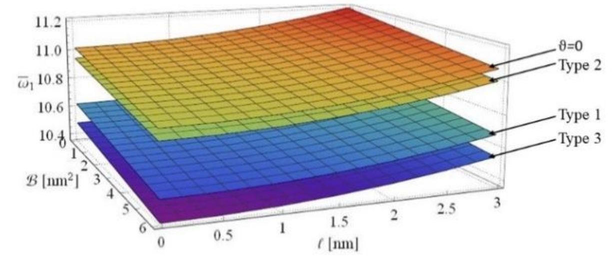

Fig. 7. Effect of nonlocal parameter $\mathfrak{B}$ and length scale parameter ℓ in conjunction with diverse porosity types on dimensionless fundamental frequencies of FGM nanobeam resting on Kerr foundation

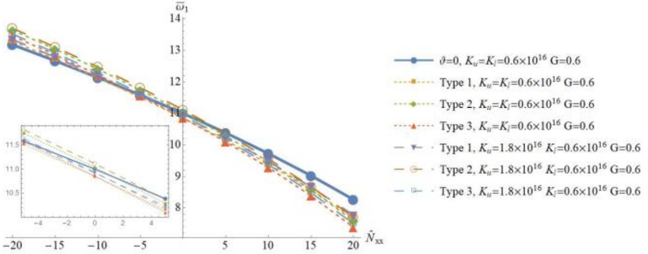

Fig. 8. Effect of axial in-plane forces in conjunction with diverse porosity types on dimensionless fundamental frequencies of FGM nanobeam resting on Kerr foundation.

Dependence of eigenfrequencies of nanobeam resting on Kerr foundation on various porosity types (porosity coefficient $\vartheta = 0.6$) is presented in Figure 7. Similar to previous analysis, porosity Type 1 and Type 3 have a similar impact on natural frequencies. From the figure, it can be also observed that increasing porosity coefficient value causes decreasing of resultant stiffness for porosity distribution Type 2, and natural frequencies are lower for structure without porosity (compare with Fig. 5).

Figure 8 presents the effect of compressive/tensile forces of FGM nanobeam with various porosity distribution and foundation stiffness. It may be observed that natural frequencies of the nanobeam decrease with increasing compressive force. It is related to the weakening of nanobeam stiffness under compressive force. Opposite effect, increasing structural stiffness, occur with increasing tensile forces. Therefore, increase of tensile forces' value causes an increase of nanobeams eigenfrequencies.

Numerical results for natural frequencies of FGM nanobeam resting on Kerr foundation with diverse porosity distribution and subjected to compressive/tensile forces are presented in Table 4. Following results are calculated for nonlocal parameters $\mathfrak{B} = 2$ and $\ell = 2$.

Tab. 4. Dimensionless natural frequency $\left(\bar{\omega}_1 = 10^2 \cdot \omega_1 L^2 \sqrt{\frac{I_0}{E_t I_2}}\right)$ of elastically supported FGM porous nanobeam under axial in-plane forces

$\hat{N}_{xx}$	G	K_u $[\cdot 10^{16}]$	K_l $[\cdot 10^{16}]$	Type 1,2,3	Type 1	Type 2	Type 3
				ϑ			
				0		0.3	
-10	0	0	0	12.0200	11.9992	12.2672	12.0856
	0.6	0.6	0.6	12.1355	12.1284	12.4052	12.2236
			1.8	12.1605	12.1563	12.4349	12.2533
		1.8	0.6	12.1929	12.1926	12.4736	12.2920
			1.8	12.2993	12.3114	12.6004	12.4187
	1.2	0.6	0.6	12.1680	12.1648	12.4439	12.2623
			1.8	12.1767	12.1744	12.4543	12.2727
		1.8	0.6	12.2414	12.2467	12.5314	12.3498
			1.8	12.3314	12.3472	12.6385	12.4569
-5	0	0	0	11.4592	11.3695	11.5941	11.4123
	0.6	0.6	0.6	11.5803	11.5059	11.7400	11.5583
			1.8	11.6065	11.5353	11.7715	11.5897
		1.8	0.6	11.6404	11.5735	11.8123	11.6306
			1.8	11.7519	11.6986	11.9461	11.7645
	1.2	0.6	0.6	11.6144	11.5442	11.7810	11.5993
			1.8	11.6235	11.5544	11.7919	11.6102
		1.8	0.6	11.6912	11.6305	11.8733	11.6917
			1.8	11.7854	11.7363	11.9864	11.8048
0	0	0	0	10.8694	10.7029	10.8795	10.6966
	0.6	0.6	0.6	10.9971	10.8476	11.0348	10.8522
			1.8	11.0246	10.8788	11.0683	10.8857
		1.8	0.6	11.0604	10.9193	11.1117	10.9292
			1.8	11.1776	11.0519	11.2539	11.0716
	1.2	0.6	0.6	11.0330	10.8882	11.0784	10.8959
			1.8	11.0425	10.8990	11.0900	10.9075
		1.8	0.6	11.1138	10.9797	11.1766	10.9942
			1.8	11.2129	11.0917	11.2966	11.1144
5	0	0	0	10.2458	9.9918	10.1144	9.9294
	0.6	0.6	0.6	10.3811	10.1467	10.2813	10.0969
			1.8	10.4103	10.1800	10.3172	10.1328
		1.8	0.6	10.4481	10.2232	10.3638	10.1796
			1.8	10.5722	10.3648	10.5161	10.3323
	1.2	0.6	0.6	10.4191	10.1901	10.3281	10.1438

			1.8	10.4292	10.2016	10.3405	10.1562
		1.8	0.6	10.5047	10.2878	10.4333	10.2493
			1.8	10.6095	10.4073	10.5618	10.3782
10	0	0	0	9.5816	9.2259	9.2864	9.0976
	0.6	0.6	0.6	9.7262	9.3935	9.4680	9.2802
			1.8	9.7573	9.4294	9.5069	9.3193
		1.8	0.6	9.7977	9.4762	9.5575	9.3701
			1.8	9.9298	9.6287	9.7224	9.5358
	1.2	0.6	0.6	9.7667	9.4404	9.5187	9.3312
			1.8	9.7775	9.4528	9.5322	9.3447
		1.8	0.6	9.8580	9.5458	9.6328	9.4458
			1.8	9.9695	9.6744	9.7719	9.5855

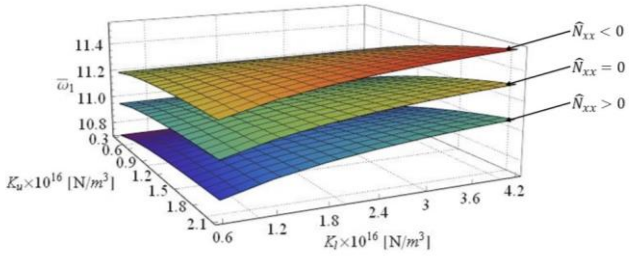

Fig. 9. Effect of Kerr foundation in conjunction with compressive/tensile forces on dimensionless fundamental frequencies of FGM nanobeam

It is observed from Figure 9 that natural frequencies of FGM nanobeam increase with increasing stiffness of both springs of Kerr foundation because the whole system becomes stiffer. For this analysis, the stiffness value of shear layer is assumed to be constant $G = 0.6$. Foundation response does not change the dynamical behavior of the structure under tensile $\left(\widehat{N}_{xx} < 0\right)$ and compressive $\left(\widehat{N}_{xx} > 0\right)$ forces. Nanobeam subjected to tensile/compressive forces undergoes increasing/decreasing of stiffness, consequently eigen frequencies increase/decrease.

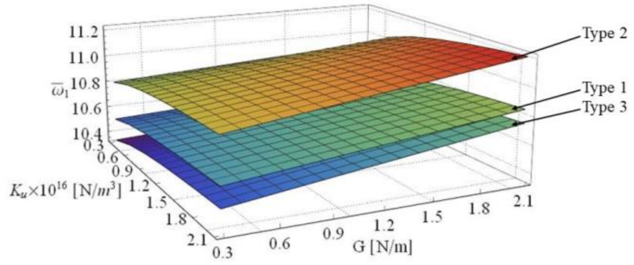

Fig. 10. Effect of Kerr foundation in conjunction with diverse porosity distribution on dimensionless fundamental frequencies of FGM nanobeam.

Figure 10 illustrates the influence of Kerr foundation on the dimensionless fundamental frequency of the nanobeam for diverse porosity distribution. For every considered porosity distribution, natural frequencies increase with increasing both stiffness coefficient of the foundation. For this analysis, stiffness value of lower spring is assumed to be constant $K_l = 0.6$. Influence of elastic foundation does not change the free vibration characteristic for the investigated porosity distributions.

7. CONCLUSIONS

In the present paper, comprehensive analysis of free vibration is conducted for the generalized model of FGM nanobeam with diverse porosity distribution, axial in-plane forces and elastic foundation. The nanobeam is modelled using the nonlocal strain gradient-based Reddy higher-order shear deformation theory. Equations of motion have been derived on the basis of the dynamical version of Hamilton principle and the analytical solution for free vibration problems of simply supported nanobeam is obtained in closed-form using Navier solution technique. Present results have been compared with the results from the literature. The parametric analysis examined the effect of axial in-plane forces, porosity distribution, and foundation response in conjunction with both nonlocal parameters on dynamical behavior of simply supported nanobeam.

The present study and the obtained results may be applied to validate different analytical and numerical methods to analyze nanostructures. Additionally, the numerical results can be used in the analysis and optimization of FGM porous nanostructures in NEMS devices.

REFERENCES

1. **Ashoori A.R, Salari E., Sadough Vanini S.A.,** (2017), A Thermo-Electro-Mechanical Vibration Analysis of Size-Dependent Functionally Graded Piezoelectric Nanobeams, *Advances in High Temperature Ceramic Matrix Composites and Materials for Sustainable Development; Ceramic Transactions*, Vol. 263, 547–558.
2. **Aydogdu M.,** (2009), A general nonlocal beam theory: Its application to nanobeam bending, buckling and vibration, *Physica E: Low-dimensional Systems and Nanostructures*, Vol. 41(9), 1651–1655.
3. **Bhushan B. (Ed),** (2004), *Springer Handbook of Nanotechnology*, Springer Verlag, Berlin.
4. **El-Borgi S., Fernandes R., Reddy J.N.,** (2015), Non-local free and forced vibrations of graded nanobeams resting on a non-linear elastic foundation, *International Journal of Non-Linear Mechanics*, Vol. 77, 348–363.
5. **Eltaher M.A., Emam S.A., Mahmoud F.F.,** (2012), Free vibration analysis of functionally graded size-dependent nanobeams. *Applied Mathematics and Computation*, Vol. 218(14), 7406–7420.

6. **Eltaher M.A., Emam S.A., Mahmoud F.F.,** (2013), Static and stability analysis of nonlocal functionally graded nanobeams, *Composite Structures*, Vol. 96, 82–88.
7. **Eltaher M.A., Fouda N., El-midany, T., Sadoun, A.M.,** (2018), Modified porosity model in analysis of functionally graded porous nanobeams. *Journal of the Brazilian Society of Mechanical Sciences and Engineering*, Vol. 40, 141.
8. **Eringen A.C.,** (1972), Nonlocal polar elastic continua. *International Journal of Engineering Science*, Vol. 10(1), 1–16.
9. **Eringen A.C., Edelen D.G.B.,** (1972), On nonlocal elasticity. *International Journal of Engineering Science*, Vol. 10(3), 233–248.
10. **Ghadiri M., Rajabpour A., Akbarshahi A.,** (2017), Non-linear forced vibration analysis of nanobeams subjected to moving concentrated load resting on a viscoelastic foundation considering thermal and surface effects, *Applied Mathematical Modelling*, Vol. 50, 676–694.
11. **Karami B., Janghorban M.,** (2019), A new size-dependent shear deformation theory for free vibration analysis of functionally graded/anisotropic nanobeams, *Thin-Walled Structures*, Vol. 143, 106227.
12. **Kerr A.D.,** (1965), A study of a new foundation model. *Acta Mechanica*, Vol. 1(2), 135–147.
13. **Kim J., Żur K.K., Reddy, J.N.,** (2019), Bending, free vibration, and buckling of modified couples stress-based functionally graded porous micro-plates, *Composite Structures*, Vol. 209, 879–888.
14. **Lam D.C.C., Yang F., Chong A.C.M., Wang J., Tong P.,** (2003), Experiments and theory in strain gradient elasticity, *Journal of the Mechanics and Physics of Solids*, Vol. 51(8), 1477–1508.
15. **Leondes C.T. (Ed),** (2006), *MEMS/NEMS Handbook Techniques and Applications*, Springer, New York.
16. **Li L., Hu Y.,** (2015), Buckling analysis of size-dependent nonlinear beams based on a nonlocal strain gradient theory, *International Journal of Engineering Science*, Vol. 97, 84–94.
17. **Lim C.W., Li C., Yu J.-L.,** (2010), Free vibration of pre-tensioned nanobeams based on nonlocal stress theory, *Journal of Zhejiang University-SCIENCE A*, Vol. 11, 34–42.
18. **Lim C.W., Zhang G., Reddy J.N.,** (2015), A higher-order nonlocal elasticity and strain gradient theory and its applications in wave propagation. *Journal of the Mechanics and Physics of Solids*, Vol. 78, 298–313.
19. **Lu L., Guo X., Zhao J.,** (2017), Size-dependent vibration analysis of nanobeams based on the nonlocal strain gradient theory, *International Journal of Engineering Science*, Vol. 116, 12–24.
20. **Lv Z., Qiu Z., Zhu J., Zhu B., Yang W.,** (2018), Nonlinear free vibration analysis of defective FG nanobeams embedded in elastic medium, *Composite Structures*, Vol. 202, 675–685.
21. **Lyshevski S.E.,** (2002), *MEMS and NEMS: System, Devices and Structures*, CRC Press, New York.
22. **Mindlin R.D.,** (1964), Micro-structure in linear elasticity. *Archive for Rational Mechanics and Analysis*, Vol. 16, 51–78.
23. **Mindlin R.D.,** (1965), Second gradient of strain and surface-tension in linear elasticity. *International Journal of Solids and Structures* Vol. 1(4), 417–438.
24. **Nazemnezhad R., Hosseini-Hashemi S.,** (2014), Nonlocal nonlinear free vibration of functionally graded nanobeams, *Composite Structures*, Vol. 110, 192–199.
25. **Pasternak P.L.,** (1954), *On a New method of Analysis of an Elastic Foundation by Means of Two Foundation Constants*, Gosudarstvennoe Izdatelstvo Literaturi po Stroitelstvu I Arkhitekture, Moscow.
26. **Rahmani O., Jandaghian A.A.,** (2015), Buckling analysis of functionally graded nanobeams based on a nonlocal third-order shear deformation theory. *Applied Physics A*, Vol. 119, 1019–1032.
27. **Reddy J.N.,** (2017), *Energy principles and variational methods in applied mechanics*, John Wiley & Sons, New York.
28. **Reza Barati M.,** (2017), Investigating dynamic response of porous inhomogeneous nanobeams on hybrid Kerr foundation under hygro-thermal loading, *Applied Physics A*, Vol. 123, 332.
29. **Saffari S., Hashemian M., Toghraie D.,** (2017), Dynamic stability of functionally graded nanobeam based on nonlocal Timoshenko theory considering surface effects, *Physica B: Condensed Matter*, Vol. 520, 97–105.
30. **Sahmani S., Ansari R.,** (2011), Nonlocal beam models for buckling of nanobeams using state-space method regarding different boundary conditions, *Journal of Mechanical Science and Technology*, Vol. 25, 2365.
31. **Shafiei N., Mirjavadi S.S., Afshari B.M., Rabby S., Kazemi, M.,** (2017), Vibration of two-dimensional imperfect functionally graded (2D-FG) porous nano-/micro-beams, *Computer Methods in Applied Mechanics and Engineering*, Vol. 322, 615–632.
32. **Şimşek M.,** (2014), Large amplitude free vibration of nanobeams with various boundary conditions based on the nonlocal elasticity theory, *Composites Part B: Engineering*, Vol. 56, 621–628.
33. **Şimşek M.,** (2016), Nonlinear free vibration of a functionally graded nanobeam using nonlocal strain gradient theory and a novel Hamiltonian approach, *International Journal of Engineering Science*, Vol. 105, 12–27.
34. **Thai H.T.,** (2012), A nonlocal beam theory for bending, buckling, and vibration of nanobeams, *International Journal of Engineering Science*, Vol. 52, 56–64.
35. **Thai H.T., Vo T.P.,** (2012a), A nonlocal sinusoidal shear deformation beam theory with application to bending, buckling, and vibration of nanobeams. *International Journal of Engineering Science*, Vol. 54, 58–66.
36. **Thai H.T., Vo, T.P.,** (2012b), Bending and free vibration of functionally graded beams using various higher order shear deformation beam theories. *International Journal of Mechanical Sciences*, Vol. 62(1), 57–66.
37. **Timoshenko S., Woinowsky-Krieger S.,** (1959), *Theory of plates and shells*, McGraw-Hill Book Company, New York.
38. **Toupin R,A.,** (1962), Elastic materials with couple-stresses. *Archive for Rational Mechanics and Analysis*, Vol. 11, 385–414.
39. **Yang F., Chong A.C.M., Lam D.C.C., Tong P.,** (2002), Couple stress based strain gradient theory for elasticity, *International Journal of Solids and Structures*, Vol. 39(10), 2731–2743.
40. **Zhang K, Ge M.-H., Zhao C., Deng Z-C., Lu, X-J.,** (2019), Free vibration of nonlocal Timoshenko beams made of functionally graded materials by Symplectic method, *Composites Part B: Engineering*, 156, 174–184.

The work has been conducted within W/WM-IIM/3/2020 project and was financed by the funds of the Ministry of Science and Higher Education, Poland.

DOI 10.2478/ama-2020-0021

DESIGNING OF THE MACHINE FOR CUTTING TRANSPORT BELTS: CONCEPTUAL WORKS

Aashutosh KALE[*], **Aleksandra BISZCZANIK**[**], **Krzysztof WAŁĘSA**[**], **Mateusz KUKLA**[**],
Maciej BERDYCHOWSKI[**], **Dominik WILCZYŃSKI**[**]

*Rajarambapu Institute of Technology, Rajaramnagar, Uran Islampur, Maharashtra 415414, India
**Institute of Machine Design, Poznań University of Technology, ul. Piotrowo 3, 61-138 Poznań, Poland

ashutosh.kale15@gmail.com, aleksandra.biszczanik@put.poznan.pl, krzysztof.walesa@put.poznan.pl, mateusz.kukla@put.poznan.pl,
maciej.berdychowski@put.poznan.pl, dominik.wilczynski@put.poznan.pl

received 24 April 2020, revised 4 November 2020, accepted 6 November 2020

Abstract: Belt conveyors are commonly employed in manufacturing and excavation processes. One of the basic components of such equipment are flat transport belts which can be monolithic or composite. In both cases, the belts are most often made of plastic materials. The manufacturing process of flat transport belts usually involves two stages. During the first stage, belts of very high length of up to several hundred meters are manufactured with use of the correct technology for a given belt type. In order to be usable in the finished conveyor system, correct length of such belts is to be achieved. Considering the above, the subsequent stage of manufacturing requires cutting the belts down to the appropriate length and very often joining the ends to form a closed loop with specific circumference. In an attempt to answer the demand of the manufacturing industry, the authors took up design works on an automated device for crosswise cutting of monolithic and composite belts. This article presents three construction concepts of the authors' own design together with an analysis of construction and operating factors which affect their usability. The presented discussion leads to selecting one of the solutions for which a drive system concept designed by the authors is proposed. Additionally, an analysis of the influence of the cutting knife geometry on cutting force is provided.

Key words: Transport belts cutting, Flat transport belts, Polyurethane and composite belts, Knife cutting, Knife penetration force

1. INTRODUCTION

Belt conveyors are widely employed in the processing and excavation industries. They are commonly used in food processing plants as well as for transporting food and plants (Soares et al., 2014). They are also used for internal transportation of components on production lines, e.g.: packaging, glass, paper (BASF, 2010; Breco, 2011). Conveyors with perforated transport belts may also be used for vacuum conveying of low density materials (Wojtkowiak et al., 2017). The use of belt conveyors in many industry branches and under different operating conditions necessitates that belts made of different materials are used, usually polymer as well as with different geometric parameters (Domek and Dudziak, 2011). Industrial manufacturing typically uses flat belts with thickness much lower than their width and length. These components are characterized by relatively high flexibility when untensioned, which is the key factor to account for when designing equipment for their processing (Berdychowski et al., 2020).

The manufacturing process of drive belts usually involves producing belts of very high length and winding them on reels. In the next stage of manufacturing, it is cut down to the required size. After this operation is carried out, the belt can be used in a device. In numerous cases it is required to use belts forming a closed loop which calls for another process to form a permanent connection of the belt ends.

Manufacturing a complete transport belt, apart from cutting it to size and connecting ends, if required, frequently involves many additional operations such as: perforation, surface activation and coating as well as mounting additional components to improve transport efficiency, which may involve making hot welded or adhesive connections (Behabelt, 2015; Fierek et al., 2020; Sikora, 1993).

Considering the wide scope of application of transport belts, which results in a variety of requirements that are set for these components, one needs to ensure that the crosswise cutting operation produces a product of high quality. This requirement involves primarily the quality of edge after cutting as well as shape and dimensioning accuracy of the entire belt. In addition, the broad range of possible additional processing means that the requirements to maintain the correct edge dimensioning are also critical. Furthermore, surface quality after the cut is performed has a material effect on the possible future processing of the belt. Uneven, frayed cut may necessitate further processing operations before the subsequent stages of manufacturing, which causes loss of material, increases manufacturing time and additional expenses.

The process of cutting flexible materials may present numerous challenges. The disadvantageous factors include the relatively low thickness of the processed products which results in its high flexibility (Broniewicz et al., 1970; Wałęsa et al., 2019).

In order to meet the industry demand regarding the crosswise cut of the belt to achieve the desired length, works were taken up to design a device for guillotine cutting of composite belts made of different polymers as well as monolithic belts made of thermoplastic polyurethane.

The aim of this work is to discuss the conceptual designs developed for the construction of the device for cutting flat transport belts and to select the most suitable solution based on analyzing the factors related to construction and operation for each proposed solution. The selected concept will be supplemented with a control system design together with preliminary considerations for selecting the optimal knife geometry. In particular, the latter consideration is of significant importance as identifying the effective values of process forces is the baseline approach in conscious design of machines and technological devices (Górecki et al., 2016, 2020a and 2020b; Górecki, 2020; Klimpel, 2000; Wojtkowiak and Talaśka, 2019).

2. DESIGN ASSUMPTIONS

The design of every mechatronic device requires to formulate certain design assumptions (Osiński, 2007). Typically, they follow the requirements specified by the intended user for the prepared design as well as any limitations imposed by the current state of technology, or any conditions which stem from the available manufacturing technology.

Flat transport belts which are to be cut are characterized by the following geometric parameters, as per the user's specification:

- maximum width *s* = 500 mm,
- maximum thickness *g* = 10 mm,
- flat profile or toothed on one side.

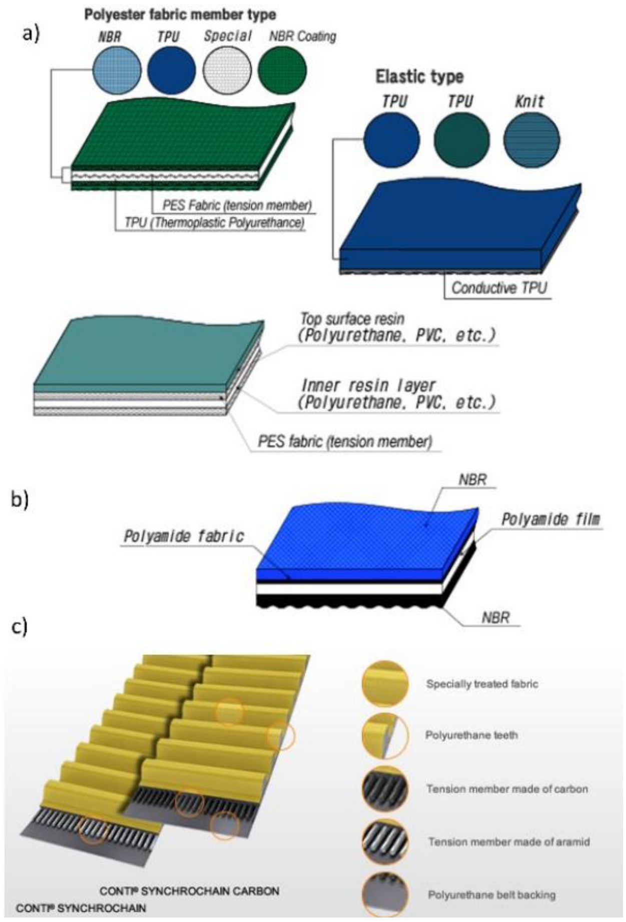

Fig. 1. Example composite belt structures (Continental, 2020; Wilhelm Herm. Müller, 2020; Wojtkowiak et al., 2018a and 2018b)

The cut belts may be made of two types of materials:

- monolithic thermoplastic elastomer based on polyurethane, non-foamed and non-reinforced (Puszka, 2006; Żuchowska, 2000). The material is typically manufactured in form of a flat tape, cast or extruded (Krawiec and Domek, 2019),
- composite structure comprising several layers of different polymer materials (Fig. 1).

In the case of composite belts, the most commonly employed plastic materials used as the constituents of the composite are: polyethylene, polyester fabrics, polyvinyl chloride, rubber, polyamide and aramid fiber (Madej and Ozimina, 2010). Depending on the specific belt, some of these materials can be used in the belt body and others as reinforcement, e.g. in form of fabric, foil or loosely placed fibers (Ciszewski and Radomski, 1989). The diversity of constituent materials means that the required force can change in the course of the separation process. Based on the data provided in literature, the cutting force, depending on the method employed, is between 30 and 7000 [N]. The force value depends on belt thickness, the type of material as well as the method of performing the cut. As evidenced in the body of research, the force values are greater when perforating or cutting reinforced belts with thickness up to 6 mm, and lower when cutting flat belts with thickness up to 1 mm (Wojtkowiak et al., 2018a and 2018b; Wilczyński et al., 2019).

The information regarding the type of material to be cut is particularly important. What follows from numerous research, the necessary force to cut different belts will vary in a great range, similarly to the character of cutting force variance being different for different belts (Groover, 2015), e.g.:

- for belts made of thermoplastic polyurethane, the force necessary for the technical performance of cutting the flat belt exhibits a strong non-linear dependence on e.g. cutting speed (Wałęsa et al., 2020b; Wanqing et al., 2017),
- for some types of composite belts (Fig. 1), the force necessary to perform the cut is varied, multi-linear, with the graph line depending on the number and thickness of the individual layers of the composite, whereas the coefficient of inclination for individual parts of the characteristic depends on the specific type of material (Talaśka and Wojtkowiak, 2018).

The variety of cut belts necessitates the development of a construction solution for the cutting device which enables to efficiently perform the operation regardless of the processed material.

The subsequent stages of the manufacturing process, including connecting the belt ends to form a closed loop or surface coating, require maintaining the highest possible precision of the cut, typically referred to as: maximum belt edge non-linear error after cutting, as well as allowable deviation from perpendicularity relative to side surface. Moreover, the belt ends at the point of cut should be smooth without need for further processing. This requirement is particularly important in the case of composite belts with fabric reinforcement. In this case, for all the punching and cutting operations, it is necessary to exactly sever the reinforcement fibers so that they are not drawn out from the belt structure (Wojtkowiak et al., 2018a and 2018b). For monolithic belts, particularly when cutting belts of higher thickness, an edge chamfering effect is observed resulting from a complex state of stress in the cut area (Wałęsa et al., 2019, 2020a and 2020b).

One of the conditions for seeking the optimal construction solution for the belt cutting device is the requirement to maintain compatibility of the device with other machines employed in the flat transport belt manufacturing process. The designed device must not apply any force on the belt which might cause its displacement as it is manufactured on an automated production line involving other equipment, e.g. for lengthwise cutting and perforation. The designed solution must perform its intended function without affecting the other processes. It is required that the belt introduced to the device operating area does not change its longitudinal and lateral position. Moreover, carrying out the cut must not cause any deformation of the belt.

The above observations together with the experience involving the designed equipment for cutting and perforating composite belts allow to formulate the following design specification:

- the machine must ensure the cutting operation maintains the required geometric accuracy, with maximum perpendicular deviation from the side edge being 1 mm and maximum rectilinear error of the belt edge being 0.5 mm,
- after the cutting operation is performed, the resulting edge must be smooth without fraying of the reinforcement fibers of composite belts an without chamfering of edges of monolithic belts,
- the device must not apply any external force to the belt to cause it to move,
- the working motion should separate the belt in one pass to maintain a uniform cutting line. This approach is necessary, considering the flexibility of the worked material.

With view of the specifications provided above, a preliminary analysis was carried out for 3 different methods of delivery of the belt cutting process:

- milling with shank cutter,
- guillotine cutting using two cutting edges to ensure the process is similar to a pure shear,
- guillotine cutting using one cutting edge with the working knife being pressed into the belt with specified force. In this variant, the working knife is supported by a rigid body with a recess for the blade allowing for collision-free passing through the material.

The above concepts of implementation of the crosswise cut operation were subject to an analysis which allows to formulate the following conclusions:

- the milling variant was discarded because this method requires several passes to separate the material along its entire length. Furthermore, it may cause reinforcement fibers to get drawn outside the composite belt together with a significant loss of material,
- the variant to employ guillotine cutting using two knife edges was discarded because such system requires highly precise instrumentation, with clearance adjustment between the main blade and counterblade. Furthermore, this approach causes the belt to move upwards, which may cause a displacement in the system.

The variant to be used in the implementation shall employ guillotine cutting using a single cutting edge. This concept was considered to be the most appropriate due to the lower complexity of construction (single knife moving vertically) as well as the expected best cutting result.

The concept of guillotine cutting employing a single knife with supporting material is furthermore the easiest to implement on an existing belt manufacturing line. Such a solution can easily be framed within a gated structure. This way the belt will be positioned on the table contained inside the frame to facilitate accurate positioning to perform the cut. At the same time, the cut belt can be passed to the subsequent workstation of the manufacturing line.

3. DEVICE CONSTRUCTION CONCEPTS

Based on: the listed requirements regarding the operation of the guillotine mechanism as well as the resulting assumptions regarding device construction, three conceptual designs were developed to facilitate crosswise cutting of flat transport belts. For each proposed solution, the same profiled table with grips to immobilize the belt were envisioned to ensure correct tensioning of the belt and preventing its further motion. This facilitates the correct performance of the cutting operation and maintaining the required dimensioning accuracy. Furthermore, this is beneficial for obtaining the required surface quality of the belt after the cut, which is one of the requirements related to the end result of the carried out operation. Finally, the tabletop will feature a recess allowing the blade to move safely after cutting the material.

In each of the proposed design concepts, the cutting force is generated by use of pneumatic actuators. This choice is dictated by operational factors as compressed air used in the drive system is typically readily available on the premises of the manufacturing facility.

When formulating the construction concept of the entire device, the final geometry of the knife was not considered. The solutions presented further mostly differ with respect to: the number of employed pneumatic actuators, the shape of the worktable on which the cutting process is to be carried out, the size of the frame, employed instrumentation and the method of transmitting the force from the actuator to the knife.

According to the first concept (Fig. 2), the blade (5), attached to a guide beam (3), lead on linear guides (4) is put to motion via two bi-directional pneumatic actuators (2). This way the blade is pressed into the flat transport belt (6) placed on the supporting table (7), causing the belt to become cut. The total displacement of the knife (5) is equal to the piston stroke length of the pneumatic actuator (2).

The proposed device utilizes 2 pneumatic actuators (2) installed vertically at the upper beam of the device frame (1). The guide beam (3) is fastened by joints to the piston rods of the actuators (2), a small distance away from its ends. The guide beam (3) with attached simple knife (5) is connected with two guides (4) placed on both sides. The guides are to ensure correct travel of the knife. The belt (6) to be cut is placed on the table (7) under the knife (5) and secured with grips (8).

During device operation, the extension of the actuator piston rod causes a downward movement of the guide beam with the knife. This exerts pressure on the belt resulting in cutting force with value dependent on the surface area of actuator pistons and their supply pressure.

The advantages of this solution include:

- simple construction facilitating easy integration with existing manufacturing line and problem-free operation,
- achieving uniform distribution of force on the cutting edge,
- possibility of easy modification.

The disadvantages of the presented solution include:

- no possibility to adjust the stroke of the blade which limits the possibility to adjust the device for cutting belts of different thickness or other materials used in the belt manufacturing industry, e.g. foams,
- the system with two actuators acting as a joint drive for the fastened beam with knife is susceptible to the slanting of the beam and consequently of the knife. Synchronous operation of pneumatic actuators is typically very challenging to achieve,

this may lead to uneven extension and slanting of the beam causing jamming on vertical guides. In extreme cases, it is possible for one edge of the blade to hit the belt and damage another component. Therefore, the pneumatic control system necessary for the device with such construction requires to use the relatively expensive synchronizing valves,
- the actuators effect the cutting force dynamically during the extension of the piston rod, which increases the probability of damaging them as a result of piston rod buckling (Osiński, 2007),
- the required length of the blade for cutting belts with assumed width necessitates large dimensions of the machine and high spacing between the actuators.

The second solution also entails employing a set of two vertical pneumatic actuators (2), attached to the upper beam of the frame (1), however, in this variant the guide beam (3) with attached knife (5) is longer, therefore the knife is placed on an arm outside the frame (Fig. 3).

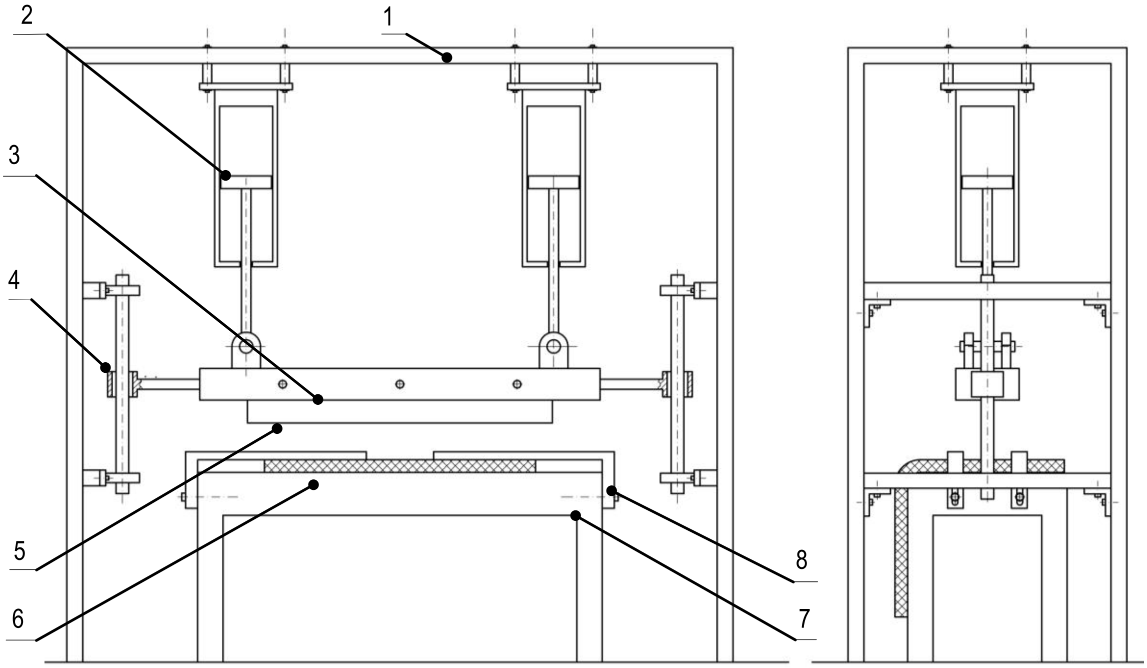

Fig. 2. Device for crosswise cutting of transport belts according to the first proposed concept: 1 – frame 2 – pneumatic actuator, 3 – guide beam, 4 – linear guide, 5 – knife, 6 – belt, 7 – table, 8 – holding grips

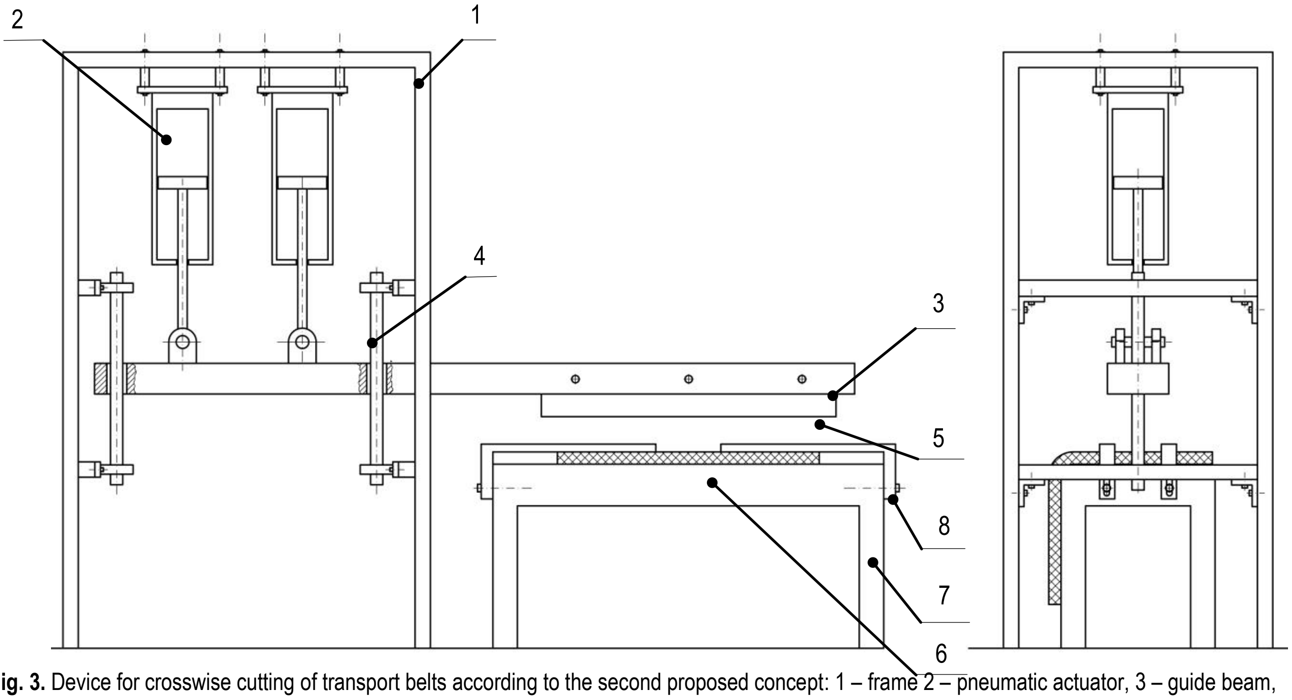

Fig. 3. Device for crosswise cutting of transport belts according to the second proposed concept: 1 – frame 2 – pneumatic actuator, 3 – guide beam, 4 – linear guide, 5 – knife, 6 – belt, 7 – table, 8 – belt grips

Employing a lever-like system alters the distribution of forces applied to the knife, whereas the dependency between knife displacement and piston displacement is the same as in the first design concept.

An advantage of the second design concept is the possibility to adapt the device to cutting belts that are wider than provided in initial assumptions. It is possible because in this solution the actuator spacing does not depend on the width of the belt (6) and the knife (5), whereas the table supporting the belt is placed outside the frame. This allows to reduce the width of the frame (1). However, one needs to consider that too low width of this component in such arrangement can negatively affect device stability and rigidity of the beam guiding (3). Additionally, the beam (3) component has significant length which means its rigidity becomes a critical characteristic. In the presented system, the force load on the guide beam is located outside the area between its supports, additionally, the dual pneumatic actuator drive solution without synchronization can cause slanting and jamming in the guides. Therefore, similarly to the first design concept, synchronization of actuators will be required.

The third design concept (Fig. 4) involves a single pneumatic actuator (2) driving a cam (9) which revolves on a bearing in a grip (10) presses on the beam guiding the knife (3). The presented solution is characterized by the fact that the displacement of the knife is not dependent exclusively on the extension of the actuator since it is possible to use a cam with movable fastening point for the actuator piston rod joint.

In this solution, the pneumatic actuator (2) is installed horizontally and the piston rod is connected to the cam (9) by a pin placed in the oval shaped hole in the cam. Additionally, the cam is installed in the fixture (10) which allows free rotation. In this arrangement, extension of the actuator causes rotational movement of the cam which due to eccentricity can affect the guide beam (3) by pushing it downwards. This motion causes displacement of the knife to cut the belt. The proposed concept also includes return springs (11) which cause the guide beam with the knife to move upwards after the pneumatic actuator piston retracts (2). In contrast to previously described solutions, the return springs are necessary for correct device operation.

The use of such springs, apart from facilitating the return motion to the base position of the knife also provides shock absorption for the guide beam - knife system, allowing to carry out the cutting operation much more fluidly. Consequently, a significant improvement of the cut edge quality may be achieved. Moreover, the springs prevent sudden impact of the knife on the belt. An appropriate selection of cam geometry allows to shorten the stroke of the piston in comparison to previously discussed concepts. The use of cam further serves to prevent excessive downward displacement of the blade as after passing the extreme displacement of the cam, the system does not move downwards regardless of the piston extension, instead it retracts upwards. Finally, the use of one actuator simplifies the pneumatic and control systems which are to be employed.

Among the disadvantages of this design concept, similarly to the first discussed concept, is that the width of the workstation is determined by the width of the table and the cut belt, which cannot be easily adapted to cut belts with higher width than initially assumed. Additionally, the cutting force will not be equal to the force effected by the piston. This additionally entails optimizing the cam geometry for this purpose.

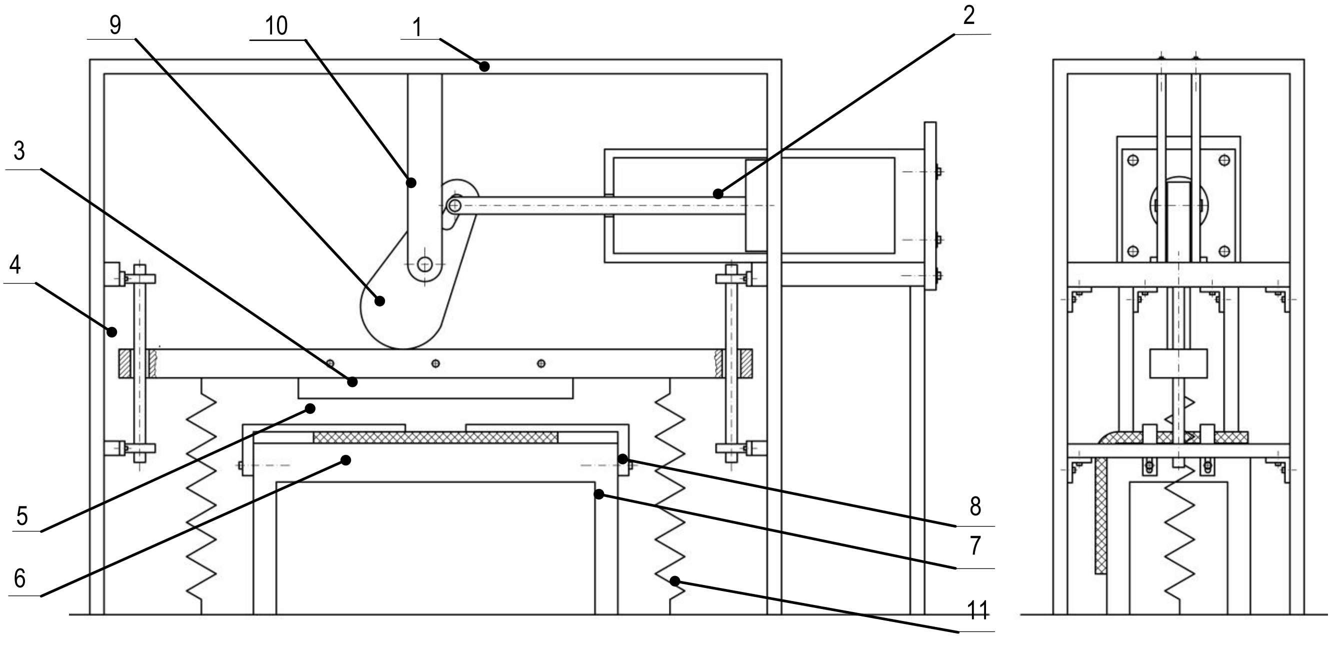

Fig. 4. Device for crosswise cutting of transport belts according to the third proposed concept: 1 – frame 2 – pneumatic actuator, 3 – guide beam, 4 – linear guide, 5 – knife, 6 – belt, 7 – table, 8 – belt grips, 9 – cam, 10 – cam fixture, 11 – spring

Analyzing the features of the presented design concepts of the transport belt cutting device, only the third variant meets all the initial assumptions. This construction of this variant is relatively simple, while similar to the first concept; however, the use of one actuator allows to simplify the pneumatic and control systems. The system concept in the third variant is further characterized by improved stability in comparison to the second variant, where dimensional requirements are difficult to specify without in-depth analysis due to the required system rigidity.

An advantage of using the cam mechanism is the additional mechanical protection of the system, preventing excessive downward motion of the knife. Such protection would be achievable in the other concept variants exclusively by selecting the exact value for the piston stroke with no margin, or by using additional sensors. The return spring system limits the dynamics of the downward motion of the knife which may have a positive effect on component wear by reducing vibration and impacts, which will further affect cutting accuracy and surface quality of the cut edge. In comparison to the other variants, the above mentioned features of the third concept indicate that this is the best implementation for the given application.

4. CONTROL SYSTEM DESIGN

The concept selected in the previous stage is to facilitate the cutting of belts with initially assumed parameters. To this end, the device will carry out actions in a sequence as provided by the working algorithm on Fig. 5.

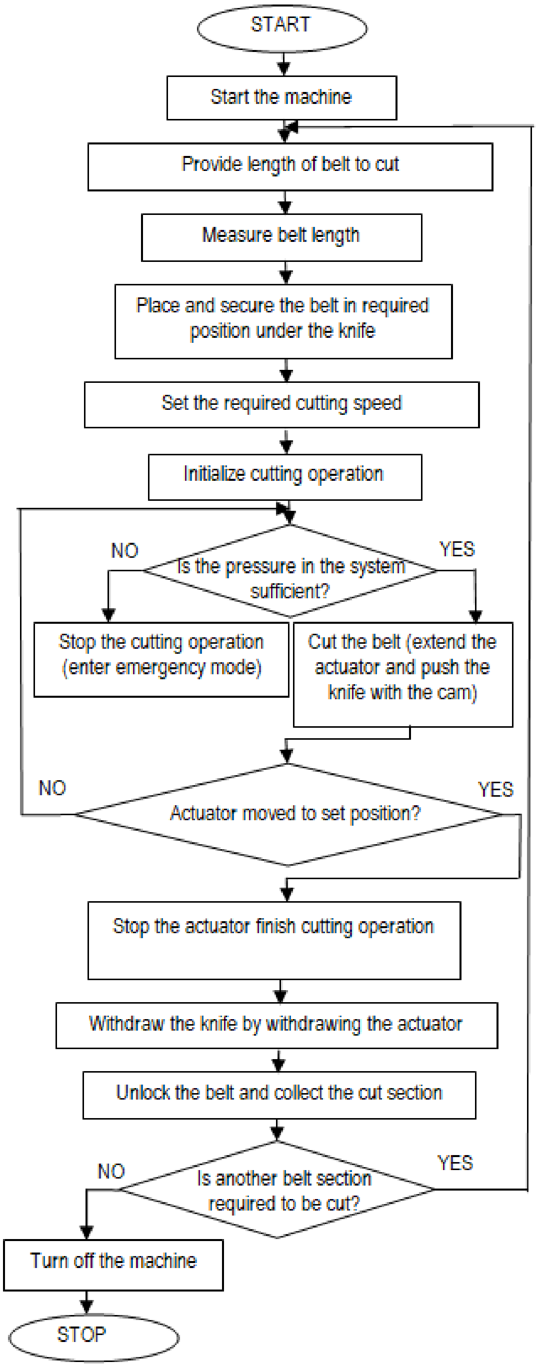

Fig. 5. The working algorithm of the machine for cutting the belt

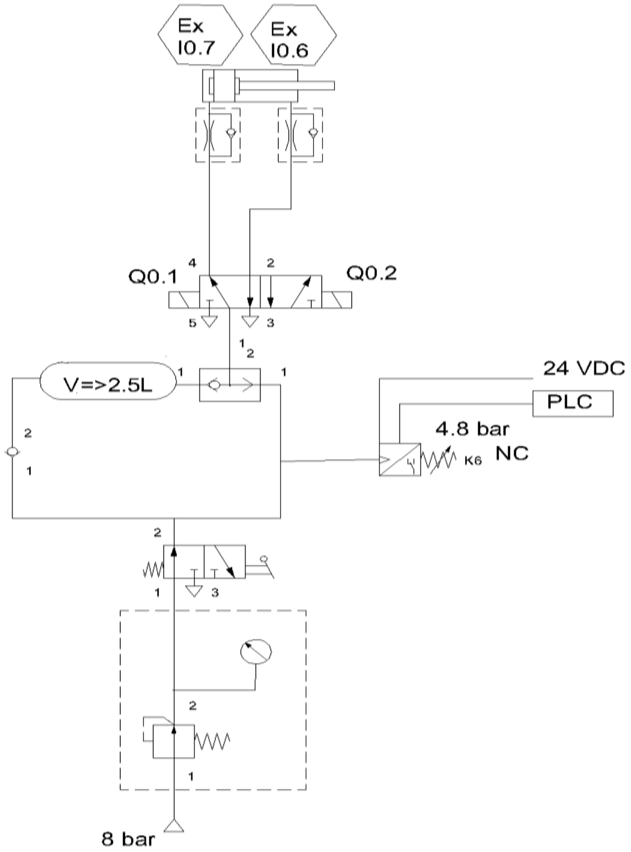

Fig. 6. Pneumatic diagram, where: Ex I0.7 and Ex I0.6 – limit switches, Q0.1 and Q0.2 – electrovalve coils, K6 – pressure meter, PLC - controller

Execution of the assumed algorithm requires a working system equipped with the necessary actors and sensors. As provided in the selected conceptual design for the belt cutter, cam motion is forced by the operation of the pneumatic actuator. Its operation necessitates designing a pneumatic system. Apart from control and supply components, it includes the necessary sensors: limit switches and system pressure sensor. The diagram is provided on Fig. 6.

The markings used in Fig. 6 correspond to the ones used in the software. For piston stroke control, 5-way electrovalve with 2 coils. This is to ensure the piston stays in the given position even after the machine stops. This results from the requirement to ensure safe operation when carrying out work with a dangerous tool, i.e. the knife. Guards were also planned in the machine to reduce the risk of dangerous situations occurring, e.g. unexpected withdrawal of the blade which may occur in the case of valves with coil and spring being used. Additionally, unexpected withdrawal or lowering of the knife may damage the belt which should also be avoided.

When carrying out design works it is necessary to maintain fluidity of motion of the actuator which facilitates improved surface quality of the cut belt. To this end, a pressure meter shall be employed which prevents the initialization of the cutting process if problems are detected with the pressure value in the system.

In order to engage the power supply to the pneumatic system, a valve with manual lever and spring was envisioned, as this system does not require frequent operation.

5. SELECTION OF KNIFE GEOMETRY

The working system of the device calls for utilizing a cutting component, i.e. the blade, able to cut the material with use of a single cutting edge. The geometry thereof has material influence on the forces present during the performance of the belt cutting operation (Wojtkowiak and Talaśka, 2019). As indicated by research, the cutting speed, cutting force and dimensions of the cut material are the most important factors in the aspect of knife wear (Chao-Lieh Yang et al., 2009). Knife wear may significantly affect post-cut surface quality. Together with the selection of the optimal blade, it is necessary to use the correct method of force transmission from the actuator to the blade. Therefore, it is very important to select its correct geometry and determine the force value to be applied on the blade to carry out the cut with set dimensions and made of material with specific strength.

The selected device concept for crosswise cutting of belts is compatible with at least two types of knife blades:

- straight blade edge, where the cutting action is applied simultaneously at the entire width of the belt (Fig. 7),
- inclined blade edge, with the inclination being one sided (Fig. 8), in the course of the cutting action, the blade penetrates the belt gradually.

The type and geometry of the knife blade has a major effect on the value and distribution of the cutting force. Generally, the cutting force with single blade edge can be described with the below formula (Marciniak, 1959):

$$F_T = k \cdot l \cdot g \cdot R_t, \tag{1}$$

where: *k* – correctional coefficient, its value is determined empirically, in includes, e.g. the dulling of the edge with the increasing number of work cycles performed, *l* – cut line length, *g* – cut material thickness, R_t – material shear strength.

It can be observed that the force necessary to cut such a belt depends not only on the material type (expressed by the parameter R_t), but also on the geometry of the cross-section. Total work to be performed by the blade in the course of the cutting process is equal to (Marciniak, 1959):

$$W = \lambda \cdot F_T \cdot s, \tag{2}$$

where: *λ* – the cutting force graph fill coefficient, expressed as a percentage value, *s* – cutting tool stroke. The coefficient *λ* describes the ratio of the area below the curve describing the dependency between the cutting force F_T, and the displacement of the tool *s*, to the total area of the rectangle determined by the maximum cutting force value F_{Tmax} and the tool stroke *s*.

Therefore, the cutting force required to separate the belt with width *m* and thickness *g*, if the straight knife blade is employed, shall be equal to (Fig. 7):

$$F_{T1} = k \cdot m \cdot g \cdot R_t. \tag{3}$$

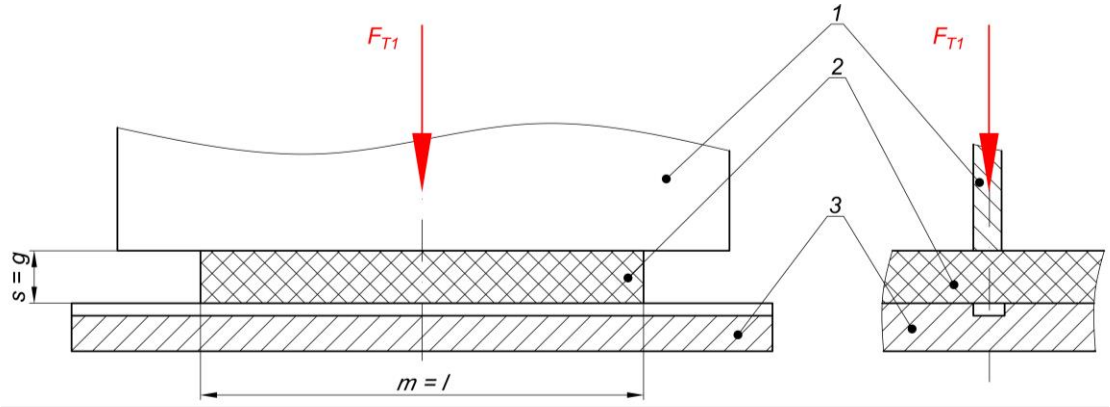

Fig. 7. Cutting with straight knife blade: F_{T1} – total cutting force, *s* – stroke of cutting tool, *g* – thickness of cut material, *l* – cut line length, *m* – width of cut belt; 1 – knife, 2 – cut belt, 3 – support plate

Total work performed during the cutting operation with the straight knife blade is equal to:

$$W_1 = \lambda \cdot F_{T1} \cdot g = \lambda \cdot k \cdot m \cdot g^2 \cdot R_t, \tag{4}$$

whereas for straight knife blade, the length of the cutting line *l* is equal to the width of the cut material *m*, and the working stroke *s* is equal to its thickness *g*.

Please consider that the use of straight knife edge for cutting does not generate additional transverse force which might cause displacement of the belt in the corresponding direction.

When examining the cutting of material with an inclined blade edge and one-sided slant, the distribution of forces is slightly different, mostly due to the presence of transverse, resulting from the inclination of the knife blade (Fig. 8).

The work W_2 necessary to separate the belt made of the same material with the same geometric parameters is equal to the work during cutting operation by the blade (Marciniak, 1959):

$$W_1 = W_2', \tag{5}$$

where W_1 – work carried out during cutting the belt material with straight blade (Fig .7), W_2' – work carried out during cutting the belt material with inclined blade (Fig. 8).

Considering the total stroke of the knife blade in this variant is equal to:

$$s_2 = g + m \cdot \tan\varphi. \tag{6}$$

Therefore, the total work W_2 carried out during the cutting of the belt with thickness *g* and width *m* by the inclined knife edge is:

$$W_2 = \lambda \cdot F_{T2} \cdot (g + m \cdot \tan\varphi). \tag{7}$$

At the same time, the work can be expressed with the following formula:

$$W_2 = W_2{}' + W_2{}'', \tag{8}$$

whereas W_2 – total work carried out during cutting of the belt with inclined knife edge, $W_2{}'$ – the work required to separate the material, $W_2{}''$ – work necessary to overcome frictional resistance of inclined knife stroke.

The important matter is that the cutting force in this variant comprises two components: horizontal and vertical. Therefore, the knife must be supported on the side surface with a slide or roller guide. Consequently, the total cutting force value depends not only on the energy required to separate the material, but also on the resistance on the knife guide. Analyzing the distribution of forces during cutting operation involving the blade of such geometry, one needs to note that the cutting force F_{T2} has two components:

$$F_{T2} = F_{T2}{}' + F_{T2}{}'', \tag{9}$$

whereas $F_{T2}{}'$ – active component participating in the phenomenon of material separation, $F_{T2}{}''$ – component resulting from knife motion resistance on the guide. Its value can be calculated from the following formula:

$$F_{T2}{}'' = F_{n2} \cdot \mu_1 = F_{p2} \cdot \mu_1 = F_{T2}{}' \cdot \mu_1 \cdot \tan\varphi, \tag{10}$$

where F_{n2} – normal component to the guide surface, F_{p2} – horizontal component resulting from the cutting process with inclined knife edge, its value equal to force F_{n2}, which may also cause transverse displacement of the belt, μ_1 – frictional coefficient of the guide.

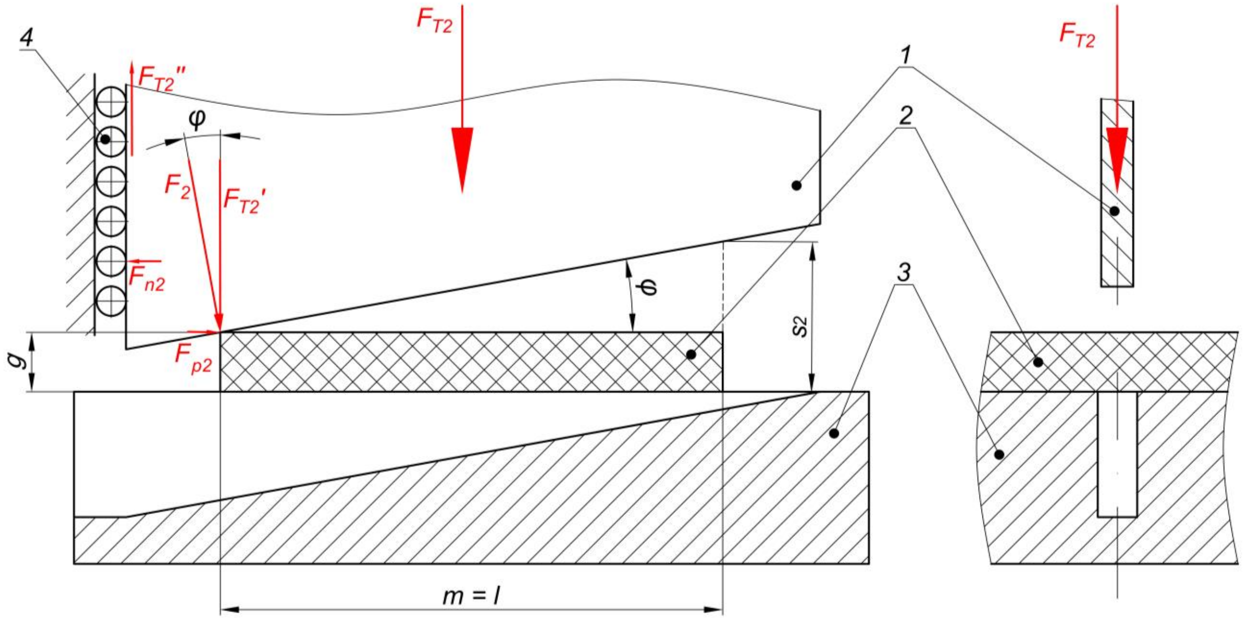

Fig. 8. Cutting with inclined knife edge, with a one-sided slant: F_{T2} – total cutting force, $F_{T2}{}'$ – force necessary to separate the belt, $F_{T2}{}''$ – force necessary to overcome the movement resistance on the guide, F_{p2} – transverse force causing belt displacement, F_{n2} – normal force affecting the guides, F_2 – resultant force, s_2 – stroke of the cutting tool, g – thickness of the cut material, l – cut line length, m – cut belt width; 1 – knife, 2 – cut belt, 3 – support plate

Therefore, the total work during cutting of the belt with knife edge with one-sided slope is:

$$W_2 = \lambda \cdot (F_{T2}{}' + F_{T2}{}'') \cdot (g + m \cdot \tan\varphi). \tag{11}$$

Considering the equal value of work to be carried out to separate the material with straight and inclined knife blade (5) the following condition can be calculated:

$$\lambda \cdot F_{T1} \cdot g = \lambda \cdot F_{T2}{}' \cdot (g + m \cdot \tan\varphi), \tag{12}$$

and therefore, the formula to describe the ratio of both forces:

$$\frac{F_{T2}{}'}{F_{T1}} = \frac{g}{(g+m \cdot \tan\varphi)}. \tag{13}$$

Based on the above, the force necessary to separate the material with inclined knife blade $F_{T2}{}'$ is equal to:

$$F_{T2}{}' = F_{T1} \cdot \frac{g}{(g+m \cdot \tan\varphi)} = k \cdot m \cdot g \cdot R_t \cdot \frac{g}{(g+m \cdot \tan\varphi)}. \tag{14}$$

Therefore, considering the dependencies arrived on (9, 10 i 14), the total force to be applied to the guillotine knife is:

$$F_{T2} = k \cdot m \cdot g \cdot R_t \cdot \frac{g}{(g+m \cdot \tan\varphi)} \cdot (1 + \mu_1 \cdot \tan\varphi). \tag{15}$$

To summarize, considering the formulas (6, 7 and 15), the total work performed in the course of cutting the belt with inclined knife blade is:

$$W_2 = \lambda \cdot k \cdot m \cdot g^2 \cdot R_t \cdot (1 + \mu_1 \cdot \tan\varphi). \tag{16}$$

One needs to consider that total work carried out to separate the belt with knife blade with one sided slope (16) is slightly higher than the work carried out when straight blade (4) is utilized. This results from the additional transverse force which is to be counteracted on the blade guide. Consequently, an additional friction resistance as the stroke of the working mechanism is performed. However, considering that, in particular in the case of roller bear-

DOI 10.2478/ama-2020-0021

ings, the frictional coefficient values are relatively low (between 0,001 and 0,01), the contribution of this component is negligibly small (Hiwin, 2012).

As observed, this method of cutting causes a transverse force to be effected which causes displacement of the belt in the corresponding direction. Its value is equal to:

$$F_{p2} = F_{T2}' \cdot \tan\varphi = k \cdot m \cdot g \cdot R_t \cdot \frac{g \cdot \tan\varphi}{(g + m \cdot \tan\varphi)}, \qquad (17)$$

The presence of this force means that the design assumptions for the device construction are not met, as the belt must not move during the operation. This can be solved by adding holders to immobilize the belt during the cutting process. The press force of the holder should meet the following condition:

$$F_d \geq \frac{F_{T2}' \cdot \tan\varphi}{\mu_2} = k \cdot m \cdot g \cdot R_t \cdot \frac{g \cdot \tan\varphi}{(g + m \cdot \tan\varphi) \cdot \mu_2}, \qquad (18)$$

where μ_2 – the coefficient of friction between the belt and the table.

What follows from the above analysis to select the optimal knife geometry, two solutions are possible. The first variant involves the use of straight knife blade which does not exert any additional forces when separating the material to cause the displacement of the belt. The second possible variant uses knife blade with one-sided inclination which is characterized by the following disadvantages:

– it necessitates the employment of an additional knife guide due to the transverse forces occurring in the process of material separation,
– transverse forces may cause the motion of the belt on the cutting table, this necessitates using additional holding components.

However, the blade with inclination is characterized by significantly lower force necessary to cut the belt. Moreover, the distribution of this force remains uniform throughout the stroke of the working tool, in contrast to the straight knife.

Considering the above mentioned advantages and disadvantages of both solutions, it is necessary to continue conceptual work on optimal geometry of the knife so as to arrive on a compromise solutions, characterized by low force value necessary to separate the material, at the same time applying no additional forces on the belt.

6. CONCLUSIONS

Transport belts are widely employed in the industry, and their manufacturing process often necessitates cutting them down to the desired length in order to prepare the final product. Market demand influenced the authors to make an effort to design a machine for cutting belts.

Considering the design assumptions formulated earlier based on specifications given by the belt manufacturers and identified based on the authors' own experience, three concepts were developed for the construction of the machine for crosswise cutting of transport belts. Each concept utilizes similar components to cause the motion of the working mechanism; however, they differ in regards to the layout of components and in the kinematics of motion of the working mechanism of the device. The first two variants employ a direct transmission of the stroke of the pneumatic actuators onto the motion of the cutting tool, these approaches were discarded due to the limited possibility of adjustment of the knife stroke. Additionally, a possibly significant challenge is identified in the possible slanting of the support beam on which the knife is fixed. The concept involving a single pneumatic actuator and cam to force the motion of the knife together with guides and springs to ensure fluid motion of the knife was believed to meet the user requirements to the greatest degree.

Furthermore, a control system concept was developed for this device, based on a programmable logic controller, connected to the pneumatic control system components.

The presented design concept of the device construction and control system structure shall be supplemented in the course of the actual machine design.

Considerations made in this work regarding the determination of forces affecting the belt during the cutting process involving the straight and inclined knife edges constitute a starting point for further examination to select the optimal geometry thereof. At this stage of works, it was established that neither the straight or the inclined blade constitute an effective solution. Therefore, further works are consider to modify the knife geometry.

REFERENCES

1. **BASF** (2010), *Thermoplastic Polyurethane Elastomers, Elastollan® - Material Properties,* BASF.
2. **Behabelt** (2015), *Product Catalogue 2015/2016,* Behabelt, Glottertal.
3. **Berdychowski M., Malujda I., Wałęsa K., Fierek A.** (2020), Analysis of angular deflection of bearing node in machine with toothed transport belt, *IOP Conference Series: Materials Science and Engineering,* 776, 012019.
4. **Breco** (2011), *Brecoflex flat belts – Product Catalogue***,** Breco, Porta Westfalica.
5. **Broniewicz T., Iwasiewicz A., Kapko J., Płaczek W.** (1970) *Methods of researches and examination of plastics properties (in Polish)*, WNT, Warszawa.
6. **Chao-Lieh Yang, Shey-Huei Sheu, Kun-Tzu Yu,** (2009) The reliability analysis of a thin-edge blade wear in the glass fiber cutting process, *Journal of Materials Processing Technology*, 209, 1789-1795.
7. **Ciszewski A., Radomski T.** (1989), *Constructuion materials in machine design (in Polish),* PWN, Warszawa.
8. **Continental,** (2020), *Continental products catalogue*, In: https://www.contitech.de (Access date: 06.04.2020).
9. **Domek G., Dudziak M.** (2011), Energy Dissipation in Timing Belts Made From Composite Materials, *Advanced Material Research,* Vol. 189-193, 4414-4418.
10. **Fierek A., Malujda I., Talaśka K.** (2019), Design of a mechatronic unit for applications of coats of adhesive, *MATEC Web of Conferences*, 254, 01019.
11. **Górecki J.** (2020), Preliminary analysis of the sensitivity of the algebraic dry ice agglomeration model using multi-channel dies to change their geometrical parameters, *IOP Conference Series: Materials Science and Engineering*, 776, 012030.
12. **Górecki J., Fierek, A., Talaśka K., Wałęsa K.** (2020), The influence of the limit stress value on the sublimation rate during the dry ice densification process, *IOP Conference Series: Materials Science and Engineering*, 776, 012072.
13. **Górecki J., Malujda I., Talaśka K.** (2016), Investigation of internal friction of agglomerated dry ice, *Procedia Engineering*, 136, 275-279.
14. **Górecki J., Talaśka K., Wałęsa K., Wilczyński D., Wojtkowiak D.** (2020), Mathematical model describing the influence of geometrical parameters of multichannel dies on the limit force of dry ice extrusion process, *Materials,* 13(15), 3317.

15. **Groover M. P.** (2015), *Fundamentals of modern manufacturing*, Willey, 503-510.
16. **Hiwin** (2012), *HIWIN Kompakt – linear guides – product catalogue*, Hiwin GmbH, Offenburg.
17. **Klimpel A.** (2000), *Welding of termoplastics materials (in Polish),* Wydawnictwo Politechniki Śląskiej, Gliwice.
18. **Krawiec P., Domek G.** (2019), *Transmissions with V-belts (in Polish)*, Wydawnictwo Politechniki Poznańskiej, Poznań.
19. **Madej M., Ozimina D**. (2010), *Plastics and composite materials (in Polish),* Wydawnictwo Politechniki Świętokrzyskiej, Kielce.
20. **Marciniak Z.** (1959), *Punching dies construction (in Polish)*, WNT, Warszawa, 299-302.
21. **Osiński Z.** (2007), *Basics of machine design (in Polish)*, PWN, Warszawa, 157-163.
22. **Puszka A.** (2006), *Polyurethanes – sources, properties and modifications (in Polish)*, Zakład Chemii Polimerów, Wydział Chemii Uniwersytetu Marii Curie Skłodowskiej w Lublinie, Lublin.
23. **Sikora R.** (1993), *Polymers processing (in Polish),* Wydawnictwo ŻAK, Warszawa.
24. **Soares, V. M., Pereira, J. G., Zanette, C. M., Nero L.A., Pinto J.P., Barcellos J.P., Bersot L.S.** (2014) Cleaning Conveyor Belts in the Chicken-Cutting Area of a Poultry Processing Plant with 45 degrees C Water, *Journal of Food Protection*, 77(3), 496-498.
25. **Talaśka K., Wojtkowiak D.** (2018), Modelling mechanical properties of the multilayer composite materials with the polyamide core, *MATEC Web of Conferences*, 157, 02052.
26. **Wałęsa K., Malujda I., Górecki J.** (2020), Experimental research of the mechanical properties of the round drive belts made of thermoplastic elastomer, *IOP Conference Series: Materials Science and Engineering,* 776, 012107.
27. **Wałęsa K., Malujda I., Talaśka K., Wilczyński D.** (2020), Process analysis of the hot plate welding of drive belts*, Acta Mechanica et Automatica*, 14(2), 84-90.
28. **Wałęsa K., Malujda I., Wilczyński D.** (2019), Shaping the parameters of cylindrical belt surface in the joint area, *Acta Mechanica et Automatica,* 13(4), 255-261.
29. **Wałęsa K., Malujda I., Wilczyński D.** (2020), Experimental research of the thermoplastic belt plasticizing process in the hot plate welding, *IOP Conference Series: Materials Science and Engineering,* 776, 012011.
30. **Wanqing L., Changqing F., Xing Z., Youliang C., Rong Y., Donghong L.** (2017), Morphology and thermal properties of polyurethane elastomer based on representative structural chain extenders, *Thermochimica Acta*, 653, 116–125.
31. **Wilczyński D., Malujda M., Górecki J., Domek G.** (2019), Experimental research on the process of cutting transport belts, *MATEC Web of Conferences*, 254, 05014.
32. **Wilhelm Herm. Müller,** (2020), *Nitta Industries – Product Catalogue (in Polish)*, In: www.whm.pl (Access date: 06.04.2020).
33. **Wojtkowiak D., Talaśka K.** (2019), Determination of the effective geometrical features of the piercing punch for polymer composite belts, *The International Journal of Advanced Manufacturing Technology*, 104(1-4), 315-332.
34. **Wojtkowiak D., Talaśka K., Malujda I., Domek G.** (2017), Vacuum conveyor belts perforation – methods, materials and problems, *Mechanik,* 90(12), 1138-1142.
35. **Wojtkowiak D., Talaśka K., Malujda I., Domek G.** (2018), Analysis of the influence of the cutting edge geometry on parameters of the perforation process for conveyor and transmission belts, *MATEC Web of Conferences*, 157, 01022.
36. **Wojtkowiak D., Talaśka K., Malujda I., Domek G.** (2018), Estimation of the perforation force for polymer composite conveyor belts taking into consideration the shape of the piercing punch, *The International Journal of Advanced Manufacturing Technology,* 98(9-12), 2539-2561.
37. **Żuchowska D.** (2000), *Construction polymers (in Polish),* WNT, Warszawa.

FUNCTIONAL BEHAVIOR OF PSEUDOELASTIC NITI ALLOY UNDER VARIABLE AMPLITUDE LOADING

Volodymyr IASNII,* Petro YASNIY,* Yuri LAPUSTA, Oleg YASNIY,* Oleksandr DYVDYK**

*Department of Structural Mechanics, Ternopil Ivan Puluj National Technical University,
Ruska str. 56, 46001 Ternopil, Ukraine
**Université Clermont Auvergne, SIGMA Clermont (ex-IFMA, French Institute of Advanced Mechanics), Institut Pascal,
BP 10448, F-63000 Clermont-Ferrand, France, CNRS, UMR 6602, IP, F-63178 Aubière, France

v_iasnii@tntu.edu.ua, petroyasniy@gmail.com, lapusta@sigma-clermont.fr, oleh.yasniy@gmail.com, sashadyvdyk@gmail.com

Received 24 March 2020, revised 10 November 2020, accepted 13 November 2020

Abstract: Cyclic loading of superelastic NiTi shape memory alloy (SMA) causes forward and reverse austenite–martensite transformations, and also increases the volume of stabilized martensite. This appears in the change of stress-strain curve form, the decrease of dissipation energy, and increase of residual strain, that is, named transformation ratcheting. In real structures, the SMA components in most cases are under the action of variable amplitude loading. Therefore, it is obvious that the loading history will influence the functional fatigue. In the present work, the effect of stress ratio on the functional properties of superelastic NiTi shape memory alloy under variable amplitude loading sequence with two blocks was investigated. The studies were carried out under the uniaxial tension of cylindrical specimens under load-full unload and load-part unload. The change of residual strain, strain range, dissipation, and cumulative dissipation energy density of NiTi alloy related to load sequences are discussed. Under both stress ratios, the residual strain in NiTi alloy is increased depending on the number of loading cycles on the high loading block that is similar to the tests at constant stress or strain amplitude. An unusual effect of NiTi alloy residual strain reduction with the number cycles is found at a lower block loading. There was revealed the effect of residual strain reduction of NiTi alloy on the number of loading cycles on the lower amplitude block. The amount of decrement of the residual strain during a low loading block is approximately equal to the reversible part of the residual strain due to the stabilized martensite. The decrease of the residual strain during the low loading block is approximately equal to the reversible part of residual strain due to the stabilized martensite. A good correlation of the effective Young's modulus for both load blocks with residual strain, which is a measure of the volume of irreversible martensite, is observed.

Keywords: Pseudoelastic NiTi alloy, functional fatigue, variable amplitude loading, strain range, residual strain, dissipation energy

1. INTRODUCTION

Shape memory alloys (SMA) are functional materials, which are characterized by shape memory effect and pseudoelasticity. Due to these properties, they are widely used in bioengineering (Nematollahi et al., 2019), aeronautics (Pecora and Dimino, 2015), robotics (Zeng et al., 2020), and civil and mechanical engineering (Zeng et al., 2020).

Recovery and residual strains are important parameters, which represent a quantitative measure of the cyclic evolution of the SMA pseudoelastic properties during loading. Recovered strain is pseudoelastic recovery from mechanical unloading and residual strain is unrecovered strain upon unloading. The accumulation of inelastic deformation (residual strain) occurring in NiTi shape memory alloy under the cyclic loading is named transformation ratcheting, since it is mainly caused by the solid-solid transformation from austenite to martensite phase and vice versa (Auricchio et al., 2004; Kang, 2013). This evolution associated with deterioration of super-elastic characteristics is referred as "functional fatigue." Recovered and dissipated energy are the parameters that represent the shape of the stress–strain hysteresis loop.

The functional properties of the pseudoelastic SMA deteriorate under cyclic loading (Auricchio et al., 2004; Araya et al., 2008; Kang G., 2013; Vantadori et al., 2018). In particular, there is a significant decrease of recovered strain, recovery energy, dissipated energy, Young's modulus, direct transformation stress, and increased residual strain at strain-controlled and stress-controlled tests (Maletta, 2014; Kang G., 2013).

It is known that the temperature (Araya et al., 2008), type of loading (Mammano and Dragoni, 2012), stress ratio (Iasnii and Yasniy, 2019b; Mahtabi et al., 2015), and heat treatment (Wagner et al., 2008) affect the functional and structural fatigue of SMA.

Most structures and structural elements made of SMA operate under variable amplitude loading at real conditions. However, there exist a few studies regarding the effect of load sequence (Soul and Yawny 2015; Mahtabi at al., 2018) and variable amplitude loading (Soul and Yawny, 2017; Mahtabi et al., 2018) on SMA functional fatigue. In particular, there was studied the effect of various amplitude block loading history under the controlled crosshead displacement on the functional properties of pseudoelastic NiTi alloy (Soul and Yawny, 2017). These blocks were applied with an increasing amplitude sequence, a decreasing amplitude sequence, and interleaved amplitudes. It was shown that the loading type, namely, the block with increasing or decreasing amplitude sequence affects significantly on the residual strain evolution. The linear damage rule cannot be not applied completely to the test full austenite partial martensite (FAPM) cycles, for which the decreasing ordering sequence resulted in lower values of maximum residual drift (Soul and Yawny, 2017).

Though, it is not clear how the functional properties of superelastic SMA will change after the alternation of blocks with high and low stress amplitude, and different stress ratio. Since degradation or total loss of functional properties may cause failure of a structure, machine or other object, it is important to study the functional behavior of SMA under variable amplitude loading. It is then expected that the global stress–strain response would reflect the previous cycling history of the specimen.

In this paper, the uniaxial functional behavior of superelastic NiTi alloy under two blocks variable amplitude loading was studied experimentally, especially the evolution of the residual strain and energy dissipation of NiTi alloy.

2. MATERIAL AND EXPERIMENTAL SETUP

A commercial pseudoelastic $Ni_{55.8}Ti_{44.2}$ rod (Wuxi Xin Xin glai Steel Trade Co., China) with diameter 8 mm was analyzed. The chemical composition of alloy was given in the paper (Iasnii et al., 2018a). Mechanical properties were determined according to ASTM F2516-14 standard (2014) in ice water at 0°C, which is higher than the austenite finish temperature (A_f = −38.7°C): yield strength, $\sigma_{0.2}$ = 447 MPa, ultimate tensile strength, σ_{UTS} = 869 MPa (V Iasnii et al. 2018a). The phase transformation temperatures were identified as A_s = –60.5°C and A_f = –38.7°C using differential scanning calorimetry by Q1000 TAI during heating and cooling of the specimen (Iasnii and Junga, 2018; V Iasnii et al., 2018b).

The effect of two blocks' variable amplitude loading on functional properties of NiTi alloy under uniaxial tension of the cylindrical specimens with a diameter of 4 mm and a gage length of 12.5 mm at 0°C was investigated. The test technique at constant amplitude loading is described in the paper (Iasnii et al., 2018). Stress-controlled tests were carried out on servo-hydraulic testing machine STM-100 (Yasniy et al., 2005) with automated control and data acquisition system under sinusoidal loading with a frequency of 0.5 Hz. Tests were performed under two blocks variable amplitude loading (Fig. 1a).

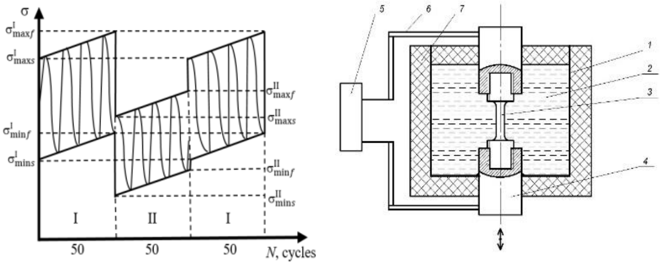

a **b**

Fig. 1. Loading history (a) and scheme of specimen testing (b): 1 – metal box; 2 – ice and ice water; 3 – specimen; 4 – clamps; 5 – extensometer; 6 – extenders; 7 – insulation wrap

The maximum and minimum loads were increased linearly in each block and jump-like every 50 cycles. This type of loading was chosen due to its similarity with the loading, which undergo the cardiovascular stents in the human body during the change of physical activity (Duerig T. et al., 2003; Pelton, A.R. et al., 2008), the structural elements of bridges due to the change of traffic, and so on. On the one hand, this allows studying the effect of loading history on the functional fatigue of SMA, that is necessary for the physical substantiation and building of SMA fatigue failure models under the variable amplitude loading. On the other hand, the features of functional behavior at variable amplitude loading are important for the design of models of structural fatigue of alloys (Soul H., Yawny A., 2017).

Two series of tests were performed. In the first series, the stress ratio was $R_\sigma = \sigma_{min}/\sigma_{max}$ = 0.09–0.13, and in the second one, R_σ = 0.33–0.51 (here σ_{min} and σ_{max} are the minimum and maximum stresses of loading cycle, respectively). The cyclic loading parameters are given in Table 1: $(\sigma^{I}_{\min s}, \sigma^{I}_{\max s}, \sigma^{I}_{\min f}, \sigma^{I}_{\max f})$ are the minimum and maximum stresses in the first and last cycle of the first (I) loading block; $(\sigma^{II}_{\min s}, \sigma^{II}_{\max s}, \sigma^{II}_{\min f}, \sigma^{II}_{\max f})$ are the minimum and maximum stresses in the first and last cycle of the second (II) loading block (Fig. 1a). The previously described sequences (Fig. 1a) and stress parameters (Tab. 1) provided the start of the tests from the fully austenitic side (R_σ = 0.09–0.13), and from the fully martensitic side (R_σ = 0.33–0.51). The force, crosshead displacement and longitudinal strain were recorded during the testing. The longitudinal strain was measured by Bi-06-308 extensometer (Bangalore Integrated System Solutions); maximum error did not exceed 0.1%. The crosshead displacement was determined by inductive Bi-02-313 sensor with an error not more than 0.1%. The tests were carried out in the chamber filled with ice and ice water (Iasnii et al., 2018b). Testing scheme is presented in Fig. 1b. This provided the constant temperature of 0°C measured by chromel–alumel thermocouple mounted on the sample with an error not more than 0.5°C.

3. RESULTS AND DISCUSSION

Typical hysteresis loops for different values of the stress range and different number of loading cycles are shown in Fig. 2.

The functional properties of pseudoelastic SMA can be characterized by residual strain ε_{res}. Fig. 3 shows the dependencies of residual strain upon the number of loading cycles at various stress ratio. The residual strain is generally increasing with the increase of loading cycles' number at stress ratio R_σ = 0.09–0.13 and reaches almost 7% before the failure (Fig. 3a). Nevertheless, the increase of residual strain at variable amplitude loading occurs only on the loading block with higher stress amplitude. The larger volume of non-damaged material is included into the transformation during the transition from the lower to the higher loading amplitude. The nature of this process is reflected in the almost constant residual strain rate on block I. This is consistent with the evolution of NiTi alloy residual strain with the number of loading cycles for blocks with an increasing amplitude sequence (Soul and Yawny, 2015). However, with the decrease of the amplitude sequence, the residual strain shows opposite tendency with the number of cycles. The effect of residual strain decrease is observed during the second loading block. This can be caused by the decrease of material volume involved in the transformation and reduction of the residual stresses during the second block. SEM and TEM studies (Hua P. et al., 2020) indicate that cyclic phase transformation results in the formation and glide of transformation-induced dislocations. These dislocations inhibit reverse transformation and result in residual martensite and residual stresses.

It can be assumed that similar to NiTi alloy heating above the austenite transformation finish temperature (Hua P. et al., 2020), low-amplitude loading triggers reverse transformation of the residual martensite after high amplitude, due to partial reduction of the residual stresses. Obviously, a decrease in residual stress will be accompanied by a decrease in residual strain.

However, this phenomenon requires a more detailed experimental study of functional properties and transformation of the microstructure under variable amplitude loading sequence.

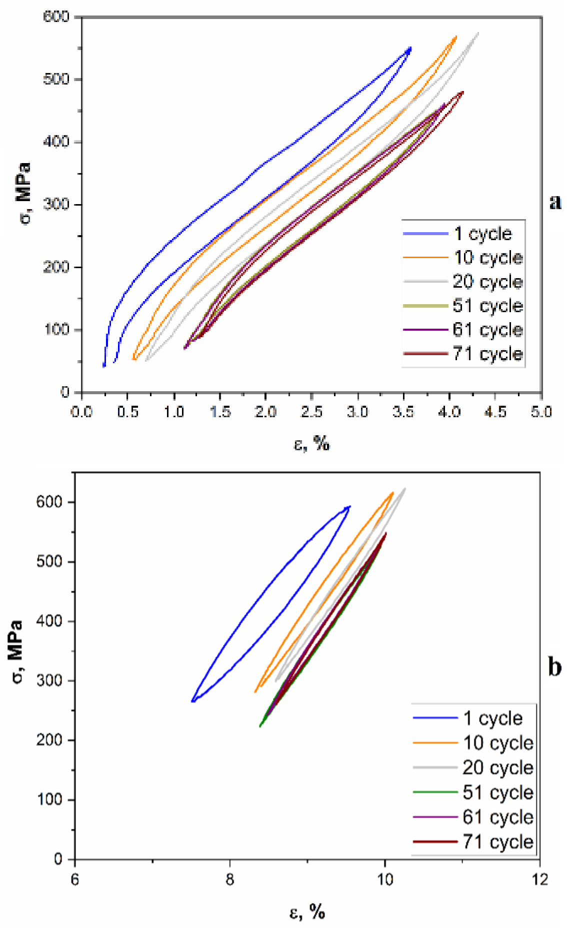

Fig. 2. Typical hysteresis loops for variable loading amplitude at R_σ = 0.09–0.13 (a) and at R_σ = 0.33–0.51 (b)

This regularity is preserved during each block of loading up till specimen failure. Therefore, one can conclude that the stepwise decrease of stress amplitude changes on the opposite the character of residual strain dependency on the number of loading cycles. The above-mentioned regularity was also observed at higher stress ratio (Fig. 3b). The increase of residual strain changes with its decrease on the block of lower amplitude (II) during next 50 cycles of loading. This alternation of the increasing and decreasing blocks is observed in each block of loading up till specimen failure.

Fig. 4 shows the dependence of the residual strain increment on the number of loading cycles in blocks I and II at the end of the corresponding block under variable loading at R_σ = 0.09–0.13. The residual strain increment was calculated as follows:

$$\Delta\varepsilon_{\text{res}} = \varepsilon^{f}_{\text{res}} - \varepsilon^{s}_{\text{res}},$$

where $\varepsilon^{s}_{\text{res}}$ and $\varepsilon^{f}_{\text{res}}$ are residual strains at start and finish of block loading, respectively.

The increment of residual strain in the block with a high amplitude (block I) increases from 0.8% for *N* = 50 cycles to 1.1% for *N* = 550 cycles. In block II, the decrement of the residual strain varies from –0.2% to –0.11% and is significantly smaller than those in block I. It was studied that the residual strain consists of two parts: plastic strain (~79% of total) due to dislocations and reversible due to residual martensite (~21%), estimated by the recovered strain after heating (Hua P. et al, 2020). In our case, the decrease of residual strain in block II comprises from 10% to 25% of total residual strain in end cycle of block I. This almost coincides with the reversible part of residual strain. Unlike the stress ratio R_σ = 0.09–0.13, at R_σ = 0.33–0.51, the residual strain at the end and at the start of each block is practically not sensitive to the number of loading cycles (Fig. 3b). This can be explained that in this case, the value of residual strain in the first cycle of loading comprises 8.8%, which exceeds the maximum strain, at which the effect of pseudoelasticity is observed (Iasnii et al., 2018). It is also known that the pseudoelastic deformation of SMA, accompanied with the stress-induced martensitic transformations leads to heat release and, in its turn, it affects the functional properties. The amplitude of the temperature increase becomes more and more significant as the strain level increases (Bubulinca et al., 2013).

It should be noted, that in both cases, the failure of the specimens occurred at the loading block with the higher amplitude.

Tab. 1. The cyclic loading parameters during testing (Fig. 1)

Block	$R_\sigma = \sigma_{min}/\sigma_{max}$	σ_{mins}	σ_{minf}	σ_{maxs}	σ_{maxf}	$\Delta\sigma_s$	$\Delta\sigma_f$	Δ*N*, *cycles*
		MPa						
I	0.09–0.10	50	58	530	580	480	522	50
II	0.10–0.13	55	47	430	470	375	423	50
I	0.33–0.43	245	216	572	650	327	434	50
II	0.49–0.51	220	280	450	550	230	270	50

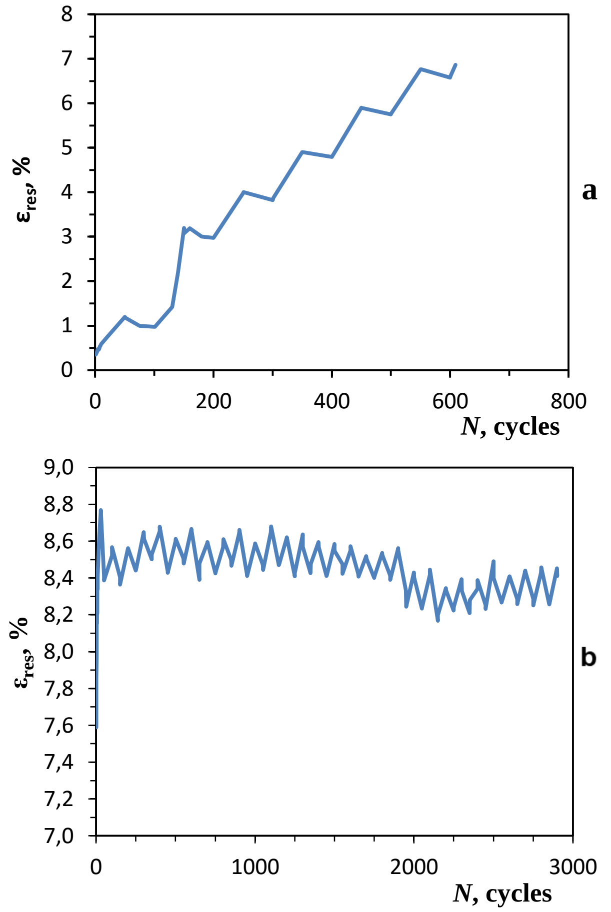

Fig. 3. The dependency of residual strain on the number of loading cycles under variable loading at R_σ = 0.09–0.13 (a) and at R_σ = 0.33–0.51 (b)

The functional properties of pseudoelastic shape memory alloy can be characterized by the strain range per cycle.

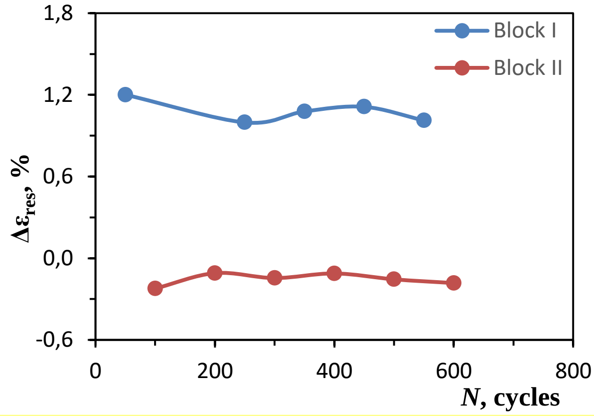

Fig. 4. The dependences of residual strain increment in block I and block II on the number cycles under variable loading at R_σ = 0.09–0.13

Fig. 5 shows the dependencies of minimum and maximum strains (Fig. 5a) and the strain range (Fig. 5b) on the number of loading cycles at R_σ = 0.09–0.13.

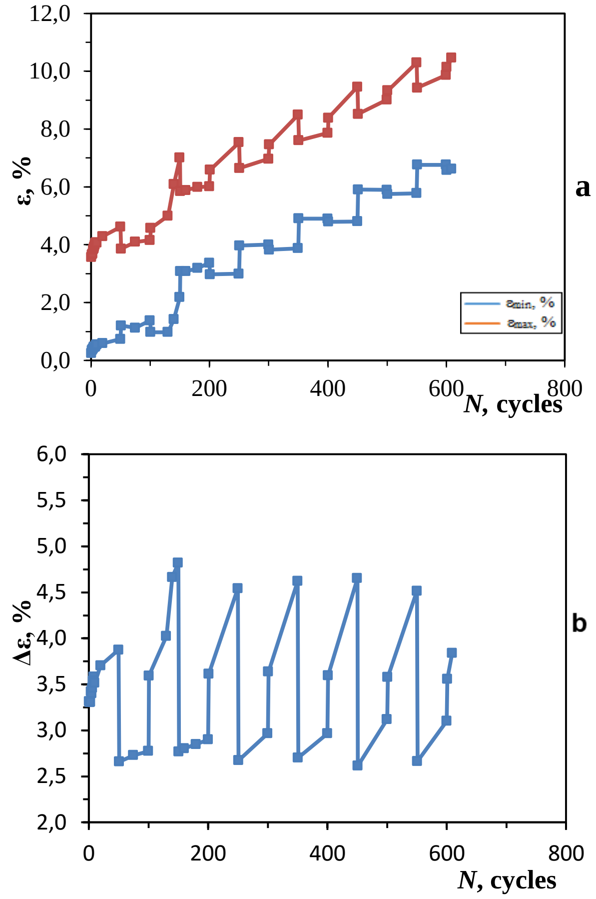

Fig. 5. The dependency of minimum and maximum strain (a) and strain range (b) on the number of cycles under variable amplitude loading at R_σ = 0.09–0.13

Unlike the residual strain, the maximum strain increases with each loading cycle at both loading blocks. Also, the more intensive increase of maximum strain is observed at block I (Fig. 1), that is caused by the interaction effect under the stepwise decrease of specimen loading.

The minimum strain remains invariant to the number of loading cycles within the margins of the first and second block, and the general increase of minimum strain occurs only during the transition from one block to the other. The character of minimum and maximum strain change affects the dependency of strain range on the cyclic loading (Fig. 5b). The mentioned above dependency and the values of the parameters of this dependency within the loading block are almost insensitive to the number of blocks loading up to the specimen failure.

The sawtooth dependency of minimum and maximum strain on the number of loading cycles was observed that was increasing on the first block and decreasing on the second one at two step variable amplitude loading at R_σ = 0.33–0.51, unlike the stress ratio R_σ = 0.09–0.13, (Fig. 5a). This dependency repeats from the loading block to loading block with the constant average strain value. Regardless, some increase of fluctuation of minimum and maximum strain after 2000 loading cycles, this does not affect the dependency of strain range on the number of loading cycles (Fig. 5b). The dependency of strain range on the number of loading cycles and the values of this dependency parameters within the loading block are also almost insensitive to the number of block up to its failure, similarly to the data at values R_σ = 0.09–0.13 (Fig. 4b).

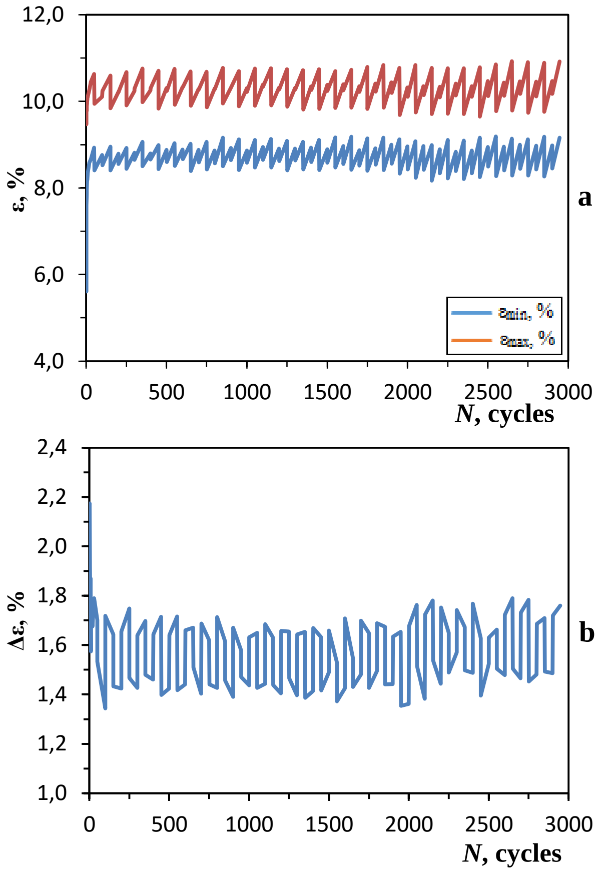

Fig. 5. The dependency of minimum and maximum strain (a) and strain range (b) on the number of cycles under variable amplitude loading at R_σ = 0.33–0.51

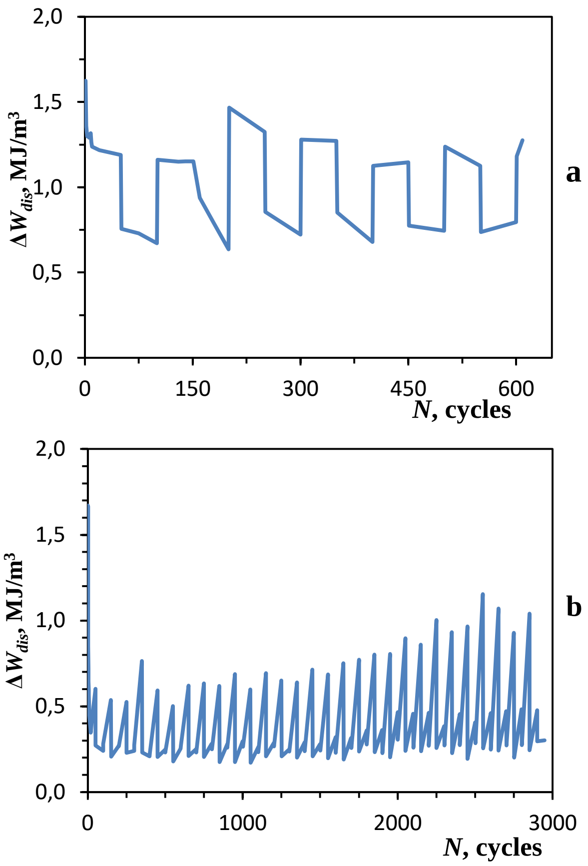

Fig. 6. Dependence of dissipation energy on the number of cycles under variable amplitude loading at R_σ = 0.09–0.13 (a) and R_σ =0.33–0.51 (b)

The dissipated energy per cycle was calculated as difference between the areas under loading and unloading stress – strain curves, using numerical integration. Fig. 6 shows the dependences of dissipation energy on the loading cycle number under variable amplitude loading at stress ratio R_σ = 0.09–0.13 and R_σ = 0.3–0.39. The intensive decrease in the dissipation energy was observed for both values of stress ratio R_σ during twenty loading cycles (block I), followed by stabilizing block. These data are consistent with the results obtained under constant amplitude loading at stress ratio R_σ = 0.1 and R_σ = 0.5 (Iasnii and Yasniy, 2019b).

Subsequently, with increasing the loading cycle number at R_σ = 0.09–0.13, the dissipation energy increases at the start and at the end of second block, and decreases at the beginning and end of the loading unit first block (Fig. 6a).

In contrast, the dissipation energy is proportional to the loading cycles at the beginning and at the end of first block at stress ratio R_σ = 0.33–0.52 (Fig. 6b). The dissipation energy is also proportional to the number of loading cycles within the first block.

Fig. 6 shows the dependences of accumulated dissipation energy on the loading cycle number under variable amplitude loading at stress ratio R_σ = 0.09–0.13 and R_σ = 0.33–0.51.

The total dissipation energy up to *i*-th cycle was determined by formula:

$$W_i = \sum_{i=1}^{N_k} \Delta W_i,$$

where ΔW_i is the dissipated energy for *i*-th loading cycle.

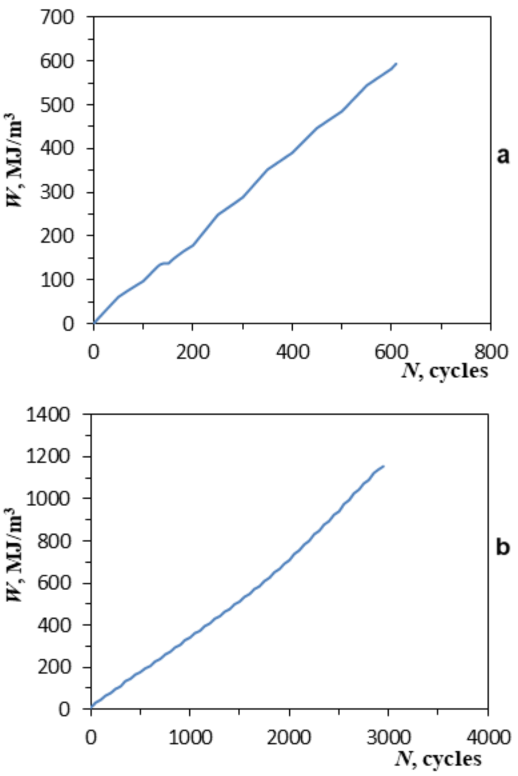

Fig. 7. Dependence of total dissipation energy on the number of cycles under variable amplitude loading at R_σ = 0.09–0.13 (a) and R_σ = 0.33–0.51 (b)

The total dissipation energy increases almost proportionally to the number of loading cycles for both stress ratios. Increasing of stress ratio from R_σ = 0.09–0.13 to R_σ = 0.33–0.51 decreases the total dissipated energy in two times for the same number of loading cycles, but increases the total dissipated energy in more than 3 times up to failure. It should be noted that under the lower value of mean stress, the stress range $\Delta\sigma_f$ exceeds the stress range at R_σ = 0.33–0.51 on the first block of loading spectrum (Fig. 1a) at the R_σ = 0.09–0.13, which determines the intensity of the total dissipation energy increase.

An important parameter that characterizes the functional properties of SMA is Young's modulus of austenite. During cyclic loading the effective Young's modulus decreases due to the increased volume fraction of stabilized martensite.

Fig. 8 shows the dependence of the effective Young's modulus at the last cycle of blocks I and II on the residual strain under variable amplitude loading at stress ratio R_σ = 0.09–0.13.

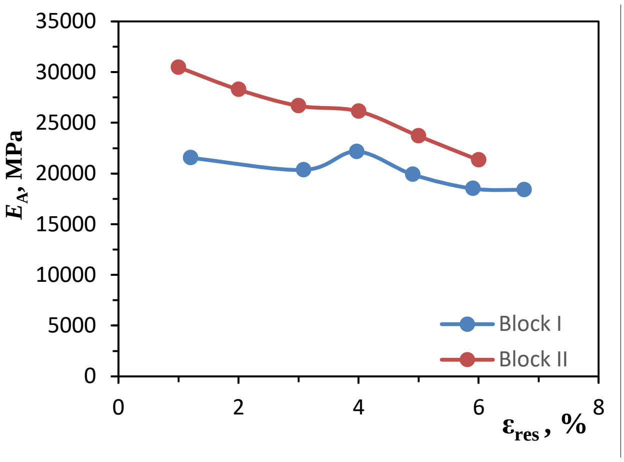

Fig. 8. Dependence of effective Young's modulus austenite in the last cycle of blocks I and II on the residual strain under variable amplitude loading at R_σ = 0.09–0.13

There is observed a good correlation of the effective Young's modulus for both loading blocks with the residual strain, which is a measure of irreversible martensite volume. Increasing the residual stress, the effective Young's modulus decreases in the last loading cycle of blocks I and II. There is a significant difference between the values of the effective elasticity modulus for I and II blocks. At equal residual strain, the effective Young's modulus is smaller at high stress amplitudes. Therefore, the effect of the maximal stress on the effective Young's modulus for a variable amplitude loading at R_σ = 0.09–0.13 is similar to the test at constant strain amplitude (Maletta et al., 2014).

4. CONCLUSIONS

The effect of stress ratio on the functional properties of superelastic NiTi SMA under variable amplitude loading sequence with two blocks at temperature above the austenite finish temperature was studied.

Residual strain significantly increases with the increase of loading cycles number at stress ratio R_σ = 0.09–0.13 and reaches almost 7% before failure. The residual strain is not sensitive to the number of cycles at the end (or start) of loading block under stress ratio R_σ = 0.33–0.51. This can be explained by the fact that in this case, the residual strain in the first cycle is 8.8% that exceeds the maximum strain under which the pseudoelastic effect is still visible.

The dependence of NiTi alloy residual strain on the number of loading cycles increases on the high loading block similarly to the test at constant stress or strain amplitude during both stress ratios.

An unusual effect of functional properties partially recovery – reduce of the NiTi alloy residual strain with the number of loading cycles is found at a lower block loading. It can be assumed that similar to heating of NiTi alloy above the austenitic transformation finish temperature, low-amplitude loading after high amplitude one triggers residual martensite reverse transformation, which partially reduce the residual stresses. The amount of residual strain decrement during a low load block is approximately equal to the reversible part of the residual strain due to the stabilized martensite. This effect can be used to the partial recovery of SMA functional properties.

With the increase of loading cycles' number, the dissipation energy increases at the start and end of block II, and decreases at the start and end of block I at the stress ratio R_σ = 0.09–0.13. In contrast to this, the dissipation energy is proportional to the number of loading cycles at the start and end of block I at stress ratio R_σ = 0.33–0.51. Also, the dissipation energy is proportional to the number of loading cycles within the block I.

Increase of stress ratio decreases the total dissipated energy for the same number of loading cycles, though increases the total dissipated energy up to failure.

REFERENCES

1. **Araya R., Marivil M., Mir C., Moroni O., Sepúlveda A.** (2008), Temperature and grain size effects on the behavior of CuAlBe SMA wires under cyclic loading, *Materials Science and Engineering: A*, 496(1-2), 209–213.
2. **ASTM F2516-14** (2014), Standard Test Method for Tension Testing of Nickel-Titanium Superelastic Materials.
3. **Auricchio F., Marfia S., Sacco E.** (2003) Modelling of SMA materials: training and two way memory effect, *Comput. Struct.* 81, 2301–2317.
4. **Bubulinca C., Balandraud X., Grédiac M., Stanciu S., Abrudeanu M.** (2014), Characterization of the mechanical dissipation in shape-memory alloys during stress-induced phase transformation, *Journal of Materials Science*, 49, 701–709.
5. **Carpinteri A., Di Cocco, Fortese G., Iacoviello F., Natali S., Ronchei C., Scorza D., Vantadori S., Zanichelli A.** (2018), mechanical behaviour and phase transition mechanisms of a shape memory alloy by means of a novel analytical model, *Acta Mechanica et Automatica*, Vol. 12, No. 2, 105–108.
6. **Duerig T., Stoeckel J., Johnson D.** (2002) SMA — smart materials for medical applications, *Proceedings of SPIE 4763*, Bellingham, WA, 7–15.
7. **Hua P., Chu K., Ren F., Sun Q.** (2020), Cyclic phase transformation behavior of nanocrystalline NiTi at microscale, *Acta Materialia*, 185, 507–517.
8. **Iasnii V., Junga R.** (2018), Phase Transformations and Mechanical Properties of the Nitinol Alloy with Shape Memory, *Materials Science*, 54(3), 406–411.
9. **Iasnii V., Yasniy P.** (2019a), Degradation of functional properties of pseudoelastic NiTi alloy under cyclic loading: an experimental study, *Acta mechanica et automatica*, 13(2), 95–100.

10. **Iasnii V., Yasniy P., Lapusta Y., Shnitsar T.** (2018), Experimental study of pseudoelastic NiTi alloy under cyclic loading, *Scientific Journal of TNTU*, 92(4), 7–12.
11. **Iasnii, V., Yasniy P.** (2019b), Influence of stress ratio on functional fatigue of pseudoelastic NiTi alloy, *Procedia Structural Integrity*, 16, 67–72.
12. **Kang G.** (2013), Advances in transformation ratcheting and ratcheting-fatigue interaction of NiTi shape memory alloy, *Acta Mechanica Solida Sinica*, 26(3), 221–236.
13. **Kecik K.** (2015), Application of shape memory alloy in harvesto-absorber system, *Acta mechanica et automatica*, 9(3), 155–160.
14. **Mahtabi M.J., Shamsaei N., Rutherford B.** (2015), Mean strain effects on the fatigue behavior of superelastic Nitinol alloys: An experimental investigation, *Procedia Engineering*, 133, 646–654.
15. **Mahtabi M.J., Stone T.W., Shamsaei N.** (2018), Load sequence effects and variable amplitude fatigue of superelastic NiTi, *International Journal of Mechanical Sciences*, 148, 307–315.
16. **Maletta C., Sgambitterra E., Furgiuele F., Casati R., Tuissi R.** (2014), Fatigue properties of a pseudoelastic NiTi alloy: Strain ratcheting and hysteresis under cyclic tensile loading, *International Journal of Fatigue*, 66, 78–85.
17. **Nematollahi M., Baghbaderani K.S., Amerinatanzi A., Zamanian H., Elahinia M.** (2019), Application of NiTi in Assistive and Rehabilitation Devices: A Review, *Bioengineering*, 6(2), 37.
18. **Pecora R., Dimino I.** (2015), SMA for Aeronautics, *Shape Memory Alloy Engineering*, Chapter 10, 275–304.
19. **Pelton, A.R., Schroeder V., Mitchell M.R., Gong Xiao-Yan, Barney M., Robertson S.W.** (2008), Fatigue and durability of Nitinol stents, *Journal of the Mechanical Behavior of Biomedical Materials*, 1 (2), 153–164.
20. **Scirè Mammano G., Dragoni E.** (2012), Functional fatigue of NiTi shape memory wires for a range of end loadings and constraints, *Frattura ed Integrità Strutturale*, 7(23), 25–33.
21. **Soul H., Yawny A.** (2015), Self-centering and damping capabilities of a tension-compression device equipped with superelastic NiTi wires, *Smart Materials and Structures*, 24(7), 075005.
22. **Soul H., Yawny A.** (2017), Effect of Variable Amplitude Blocks' Ordering on the Functional Fatigue of Superelastic NiTi Wires, *Shap. Mem. Superelasticity*, 3, 431–442.
23. **Wagner M.F., Nayan N., Ramamurty U.** (2008), Healing of fatigue damage in NiTi shape memory alloys, *Journal of Physics D: Applied Physics*, 41(18), 185408.
24. **Yasniy P., Hlado V., Hutsaylyuk V., Vuherer T.** (2005), Microcrack initiation and growth in heat-resistant 15Kh2MFA steel under cyclic deformation, *Fatigue & Fracture of Engineering Materials & Structures*, 28(4), 391–397.
25. **Zeng Z., Oliveira J.P., Ao S. Et al.** (2020), Fabrication and characterization of a novel bionic manipulator using a laser processed NiTi shape memory alloy, *Optics & Laser Technology*, 122.

sciendo

DOI 10.2478/ama-2020-0023 *acta mechanica et automatica, vol.14 no.3 (2020)*

ON GRÜNWLAD-LETINKOV FRACTIONAL OPERATOR WITH MEASURABLE ORDER ON CONTINUOUS-DISCRETE TIME SCALE

Ewa PAWŁUSZEWICZ,* Andrzej KOSZEWNIK,* Piotr BURZYŃSKI*

*Faculty of Mechanical Engineering, Department of Mechatronics Systems and Robotics,
Bialystok University of Technology, Wiejska 45c, 15-351 Białystok, Poland

e.pawluszewicz@pb.edu.pl, a.koszewnik@pb.edu.pl, p.burzynski@doktoranci.pb.edu.pl

received 7 May 2020, revised 12 November 2020, accepted 17 November 2020

Abstract: Considering experimental implementation control laws on digital tools that measurement cards are discharged every time unit one can see that time of simulations is partially continuous and partially discrete. This observation provides the motivation for defining the Grünvald-Letnikov fractional operator with measurable order defined on continuous-discrete time scale. Some properties of this operator are discussed. The simulation analysis of the proposed approach to the Grünwald-Letnikov operator with the measurement functional order is presented.

Keywords: Grünvald-Letnikov fractional operator, measurement order, time scale

1. INTRODUCTION

It is well known that during control system design process, one of the most important steps is to develop the proper mathematical model of an analyzed control plant. Generally, the analysis of experiment results shows that there is a large class of systems where behavior of real phenomena is not properly explained by using the classical calculus. It has been found that these systems not only contain non-local dynamics but can also be described using fractional-order operators and their properties, see for example in control engineering, signal processing, electronics and electrical engineering, (Buslowicz and Nartowicz, 2009; Djennoune et al., 2019; Kavuran et al, 2017, Ortigueira, 1997, Balaska et al., 2020). Among the other, an example of the control plant that shows that fractional calculus applied to the modelling of its behavior is better than the classical tools is the voltage – current relation of a semi-infinite lossy transmission line (Wang, 1987), the diffusion process of the heat into a semi-infinite (Podlubny et al., 1995), modeling and simulation of plant models (Alagoz et al., 2019). In automatic regulation and its industrial applications to process controlling the most popular and commonly used are PID controllers. However, it is known that controllers of fractional orders (FOPID) in many cases can provide better optimal preferences and behaves more robust than the classical ones, see (Ostalczyk et al., 2015; Patniak et al., 2002; Tepljakov et al., 2018). It follows from the fact that such controllers have more tuning freedom. However the usage of FOPID controllers usually requires some approximations which makes their applications more complex.

Since the Grünwald-Letnikov fractional order operator in automatic control and industry applications has been considered as the most useful and a proper tool for approximations in the scope of numerical solutions (see, e.g., Coimbra, 2003; Patniak et al., 2002; Alagz and Alisoy, 2018; Tepljakov, 2017 and references therein), we lay attention on it. The practical usefulness of this operator is due to the fact that its value depends on all past values of the fractionally derived function, so the history or memory of the process in naturally included in the analysis. Also, it provides a recursive solution in time and hence reduces computing time (Alagoz et al., 2019). However, taking into account the limitation of computational resources, computational complexity should be as low as possible. There are works addressed to optimization of number steps in approximation used in computing of the Grünwald-Letnikov fractional order operator (see Stanislawski and Latawiec, 2012; Alagoz et al., 2019; Tepljakov et al., 2012) and references therein.

The natural analytic extension of fractional order operators are variable order ones. In some ways, this is a natural direction, not only from mathematical point of view, but also arises from modelling of real-word phenomena (Patniak et al., 2002). The first works in that scope have already shown that it is a good approach to modelling but not easy research topic (see, e.g. Coimbra, 2003; Lorenzo and Hartley, 2002; Samko and Ross, 1993). Note that in this case, there exist four different definitions of these operator with variable order (see Sierociuk et al., 2013; Sierociuk et al., 2015; Valerio and Sa da Costa, 2001). These definitions have been used, for example, in modelling of FOPID controllers as well as in heat transfer process (Sierociuk and Macias, 2013). The influence on the shaping of the transient characteristics of a closed-loop systems has been analyzed in Ostalczyk et al. (2012, 2015). In each case, the variable order has been taken as a function defined on the set of natural numbers. As it is known from the engineering point of view in measurement process digital tools are used to test different control plants. This means that measurement cards are discharged periodically every time unit δ, so the measurment time is not only discrete, but partially continuous and partially discrete as on time scales (Bohner and Peterson, 2001).

We concentrate on the classical approach to the Grünwald-Letnikov fractional order operator. Taking into account its implementation in digital systems (Alagz and Alisoy, 2018, Koszewnik et al., 2016, Koszewnik et al, 2018, Pawluszewicz et al., 2019), it is natural to consider a fractional order of this operator as a function defined on continuous-discrete time scale, that is, on a model of time that extends the classical time domain of dynamical systems (Bohner and Petrson, 2002). This problem, as well as the motivation to present work, is discussed in Section 2. The maximum bandwidth of the signal occurring during discharging of the measuring card may not be a good measure of signal changes, in the case of uniform sampling, some of the samples may be unnecessary. To eliminate this redundancy, non-uniform discharging can be used. Application of the non-uniform sampling allows to reduce the amount of measured data and next decrease power consumption for computation, which is important in industrial applications. In Section 3, there is introduced the Grünwald-Letnikov operator with the discrete-continuous order following from the non-uniform process of discharging measurement cards. In Section 4, the simulation analysis of proposed approach is presented.

2. MOTIVATION

It is known that the continuous time control law of fractional order PID controller usually is expressed as $u(t) = K_p e(t) + K_i D^{\lambda} e(t) + K_d D^{\mu} e(t)$ where orders λ, μ are nonnegative, $u(t)$ denotes the control signal, $e(t)$ is the control error between the desired value and the measured value, D is a fractional operator. During experimental implementation or verification of this control law, digital tools are commonly used. This means that:

- parameters K_p, K_d, K_i are recalculated by considering particular gains of A/D and D/A (Fig. 1) converters inbuilt to measure digital tools,
- steady state error, which is strictly connected with the orders of fractional operator, is changing during the regulation process.

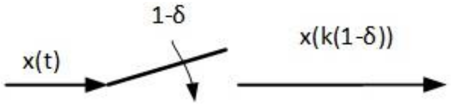

Fig. 1. Impulsator switched periodically for 1-δ time units

Furthermore, taking into account that measurement cards are discharged periodically every time unit and assuming that the discharging takes δ > 0 time units, time of simulations is partially continuous and partially discrete (not only discrete), see Fig. 1 and Fig. 2.

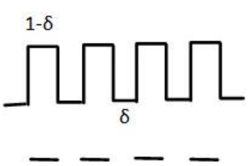

Fig. 2. Clock impulsator with duty cycle equal to 1-δ of time units

In a general case, this situation can be described using the following model of time presented on Fig. 3, see (Bohner and Petrson, 2002):

$$P_{1-\delta,\delta} = \bigcup_{k\in\mathbb{N}_0} [k, k+1-\delta] \tag{1}$$

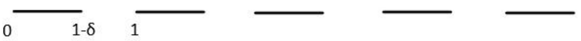

Fig. 3. Time scale $\mathrm{P}_{1-\delta,\delta}$ of signal from clock impulsator

Then the previous time instant of $t \in P_{1-\delta,\delta}$, denoted as $\rho(t)$, is

$$\rho(t) = \begin{cases} t & \text{if} \quad t \in \bigcup_{k=0}^{\infty} [k, k+1-\delta) \\ t-\delta & \text{if} \quad t \in \bigcup_{k=0}^{\infty} \{k+1-\delta\} \end{cases}$$

In fact $\rho(t)$ defines the backward jump operator of t. The difference between t and its previous time instance $\rho(t)$, called *(backward) graininess function* $\upsilon : P_{1-\delta,\delta} \longrightarrow \mathbb{R}_+ \cup \{0\}$, is defined as:

$$v(t) := t - \rho(t).$$

Putting $\rho^l = \underbrace{\rho \circ \ldots . \circ \rho}_{l\ times}$ and $\rho^0(t) = t$ inductively, one can show that $\rho^n(t) = t - \nu^n(t)$ (Ortigueira et al., 2016). Then,

$$\rho^n(t) = \begin{cases} 0 & \text{if} \quad t \in \bigcup_{k=0}^{\infty} [k, k+1-\delta) \\ t-n\delta & \text{if} \quad t \in \bigcup_{k=0}^{\infty} \{k+1-\delta\} \end{cases} \tag{2}$$

So,

$$v(t) = \begin{cases} t & \text{if} \quad t \in \bigcup_{k=0}^{\infty} [k, k+1-\delta) \\ t-\delta & \text{if} \quad t \in \bigcup_{k=0}^{\infty} \{k+1-\delta\} \end{cases}$$

for any $t \in P_{1-\delta,\delta}$.

Similarly, as in (Ortigueira et al., 2016), on the time model given by (1), one can look as a model of time defined by a set of discrete time instants $t_n, n \in \mathbb{Z}_+$, and corresponding (backward) graininess. These instants are consecutive boundary point defining a closed interval, in which graininess is null inside the intervals starting in moment k and finishing in moment $k + 1 - \delta$. Following Ortigueira et al. (2016), one can define the *graininess interval* as the width of the considered interval. For time model (1), we have $v([k, k + 1 - \delta])$=1-δ. Then, $t_n = t_{n-1} + v_n, n \in \mathbb{Z}_+,$ is the direct graininess.

Remark 1. Such approach to time model (1) allows to consider not only a uniformly discharge periodically measurement cards but also a nonuniformly discharged measurement cards with discharge time units $\delta_k, k \in \mathbb{N}$. Nonuniform sampling in some situations reduces the required computing power and data processing. It is also possible to optimize the energy consumption of the controller, and thus save energy necessary in the control processes (see, e.g. Janczak et al., 2016; Kondratiuk et al., 2018).

3. THE GRÜNWLAD-LETNIKOV OPERATOR WITH DISCRETE-CONTINUOUS FRACTIONAL ORDER

Let us consider a function $C: P_{1-\delta,\delta} \times \mathbb{Z}_+ \cup \{0\} \longrightarrow \mathbb{R}$ defined as follows:

$$C^{\alpha(\tau)}(s)=\begin{cases}0 & \text{for} \quad s<0\\ 1 & \text{for} \quad s=0\\ \dfrac{(-1)^s}{s!}\alpha(\tau)\alpha\big(\rho(\tau)...\alpha(\rho^s(\tau)\big) & \text{for} \quad s>0\end{cases} \tag{3}$$

where ρ is the graininess interval and $\rho^l=\underbrace{\rho\circ...\circ\rho}_{l\ times}$. From (3), it follows that the following recursive relation

$C^{\alpha(\tau)}(s)=C^{\alpha(\tau)}(s-1)\frac{\alpha(\rho^S(\tau))}{s}$ holds for given $s\geq 1$.

Proposition 2. *For any natural s and j such that $s>j$, it holds*

$$C^{\alpha(\tau)}(s)\pm C^{\alpha(\tau)}(j)$$
$$=\frac{j!}{k!}C^{\alpha(\tau)}(j)\left(\prod_{i=j+1}^{k}(-1)^{k-i}\alpha(\rho^i(\tau))\pm\prod_{i=j+1}^{j}i\right)$$

Proof. Thesis follows from the fact that

$C^{\alpha(\tau)}(s)\pm C^{\alpha(\tau)}(j)=\frac{(-1)^j}{j!}\alpha(\tau)\,....\,\alpha\left(\rho^j(\tau)\right)\cdot$
$\left[\frac{(-1)^{k-j}}{(j+k)....k}\alpha\left(\rho^{j+1}(\tau)\right)...\,\alpha\big(\rho^k(\tau)\big)+1\right]$. □

Definition 3. The Grünwald-Letnikov – type fractional operator $\Delta^{\alpha(\tau)}$ of functional order $\alpha: P_{1-\delta,\delta}\longrightarrow\mathbb{R}$, for a function $x: P_{1-\delta,\delta}\longrightarrow\mathbb{R}$ is defined as

$$\big(\Delta^{\alpha(\tau)}x\big)(\tau):=\textstyle\sum_{s=0}^{\infty}C^{\alpha(\tau)}(s)x(\rho^s(\tau)) \tag{4}$$

In (4), weight function $C^{\alpha(\tau)}(s)$ is given by formula (3). Note that in a natural way, it contains information about the history of the process mathematically described by function $x: P_{1-\delta,\delta}\longrightarrow\mathbb{R}$. Since $\alpha: P_{1-\delta,\delta}$, then this history strictly depends on the process of discharging a measurement card. Moreover, since the weight function $C^{\alpha(\tau)}(s)$ is defined by the graininess interval, it follows that charging/discharging of the card can be done nonuniformly. If function $\alpha: P_{1-\delta,\delta}\longrightarrow\mathbb{R}$ is unbounded, then for a fixed s, the operator (4) may not be bounded or even may not exists. We assume that for given $x: P_{1-\delta,\delta}\longrightarrow\mathbb{R}$, function $\alpha: P_{1-\delta,\delta}\longrightarrow\mathbb{R}$ is bounded and measurable. The domain of Grünwald-Letnikov – type operator $\Delta^{\alpha(\tau)}$ is formed by two sets: a set $N_\delta=\{k\in\mathbb{Z}_+ : k+1-\delta\}$ of discrete/isolated points and a set of intervals $\{k\in\mathbb{Z}_+ : [k,k+1-\delta]\}$.

In practical implementations, instead of infinite sum in (4), there is need to use a finite one

$$\big(\Delta_J{}^{\alpha(\tau)}x\big)(\tau):=\textstyle\sum_{s=0}^{J}C^{\alpha(\tau)}(s)x(\rho^s(\tau)) \tag{5}$$

where, following (Stanislawski Latawiec , 2012) and remembering that we look at time model (1) as a model of time defined by a set of discrete time instants $t_{n,}$ $n\in\mathbb{Z}_+$, corresponding to the (backward) graininess,$J=\min\big(t_{n,}\bar{J}\big)$ and $\bar{J}$ is the upper bound to s when $t_{n,}>\bar{J}$. From (5), it follows that

$$\big(\Delta_J{}^{\alpha(\tau)}x\big)(\tau)=$$
$$\begin{bmatrix}1 & C^{\alpha(t)}(1) & .... & C^{\alpha(t)}(J)\end{bmatrix}\begin{bmatrix}x(t)\\ x(\rho(t))\\ ....\\ x(\rho^{n-a}(t))\end{bmatrix} \tag{6}$$

Proposition 4. *If for every $t\in P_{1-\delta,\delta}$, there is a real number K such that $|x(\tau)|\leq K$ and $\alpha: P_{1-\delta,\delta}\longrightarrow[0,1]$, then*

$$\left|\big(\Delta^{\alpha(\tau)}x\big)(\tau)-\big(\Delta_J^{\alpha(\tau)}x\big)(\tau)\right|\leq K^2e.$$

Proof. Since

$$\left|\big(\Delta^{\alpha(\tau)}x\big)(\tau)-\big(\Delta_J^{\alpha(\tau)}x\big)(\tau)\right|$$
$$=\left|\sum_{s=0}^{\infty}C^{\alpha(\tau)}(s)x\big(\rho^s(\tau)\big)-\sum_{s=0}^{J}C^{\alpha(\tau)}(s)x\big(\rho^s(\tau)\big)\right|$$
$$\leq\sum_{s=0}^{J}\left|C^{\alpha(\tau)}(s)x\big(\rho^s(\tau)\big)\sum_{v=J+1}^{\infty}C^{\alpha(\tau)}(v)x\big(\rho^v(\tau)\big)-1\right|$$
$$\leq K\sum_{s=0}^{J}\left|C^{\alpha(\tau)}(s)\right|\left[\sum_{v=J+1}^{\infty}\left|C^{\alpha(\tau)}(v)x\big(\rho^v(\tau)\big)\right]+1\right|$$
$$\leq K^2\sum_{s=0}^{J}\left|C^{\alpha(\tau)}(s)\right|\sum_{v=J+1}^{\infty}\left|C^{\alpha(\tau)}(v)\right| \tag{7}$$

Since $\alpha: P_{1-\delta,\delta}\longrightarrow[0,1]$, then $\left|C^{\alpha(t)}(s)\right|\leq\frac{1}{s!}$, and from (7), it follows that

$\left|\big(\Delta^{\alpha(\tau)}x\big)(\tau)-\big(\Delta_J^{\alpha(\tau)}x\big)(\tau)\right|\leq K^2\sum_{s=0}^{\infty}\frac{1}{s!}=K^2e.$ □

4. SIMULATION ANALYSIS

In this Section, simulation analysis of the Grünwald-Letnikov operator with the discrete-continuous order $\alpha: P_{1-\delta,\delta}\longrightarrow\mathbb{R}$ is presented. To this aim, a process of switching on/off of the switch occurring in the holding circuit has been analyzed in detail based on electrical scheme shown in Fig. 4.

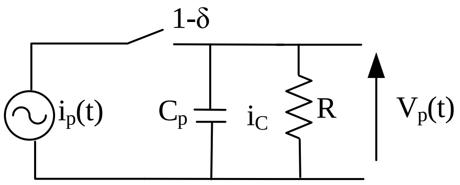

Fig. 4. Electrical circuit of RC system

Taking into account the behavior of the classical switch and the fractional operator, the capacitor has been firstly charged in the time $1-\delta$ in results of switching on/off the switch with randomly occurring delay. Next, the switch is turned off. It has led to discharging of the capacitor by time δ and also getting value of the voltage signal $x(\tau)$ from this element to further analysis. As a result, the whole process of switching on/off the switch is changeable, especially in time interval $[1-\delta,\delta]$.

The proposed approach allowed to check the influence function $\alpha: P_{1-\delta,\delta}\longrightarrow\mathbb{R}$, on fitting of the Grünwald-Letnikov – type fractional operator $\Delta^{\alpha(\tau)}$ of functional order $\alpha: P_{1-\delta,\delta}\longrightarrow\mathbb{R}$ in reference to three base signals. As the first, the sinusoidal signal $x(t)=\sin(0.04t)$, next $x(t)=H(t-a)$, where $H(\cdot)$ denotes the Heaviside's step function, and as the last one, $x(t)=e^{-0.1t}$ signal have been considered for function α, respectively. The obtained results for the given signals on time domain $P_{1-\delta,\delta}$

presented in Figs. 5–7 showed that the signal with the Grünwald-Letnikov – type fractional operator of order $\alpha : P_{1-\delta,\delta} \longrightarrow \mathbb{R}$ is best customized to the base signal $x(t)$ for ever smaller values of the function $\alpha : P_{1-\delta,\delta} \longrightarrow \mathbb{R}$ also of a function that has increasingly smaller values. Such behavior is especially visible for the variable value of the sampling step in the Grünwald-Letnikov – type fractional operator of order $\alpha : P_{1-\delta,\delta} \longrightarrow \mathbb{R}$, where increasing this value has led to weaker fitting to the base signals $x(t)$.

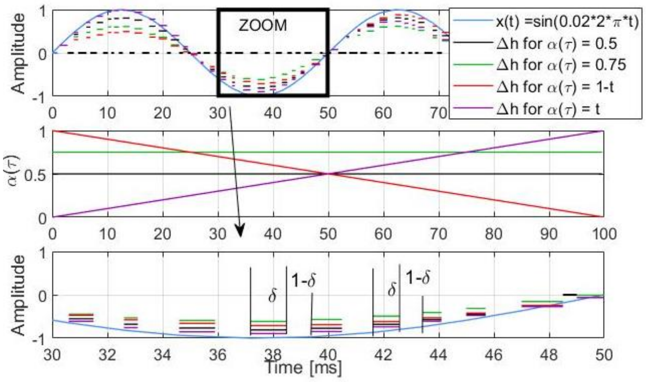

Fig. 5. The comparison of sinusoidal discrete-continuous signal with different values of function $\alpha : P_{1-\delta,\delta} \longrightarrow \mathbb{R}$ (for $\alpha(t) = t$, $\alpha(t) = 1 - t$, $\alpha(t) = 0.5$ respectively) to the base function $x(t) = \sin(0.04t)$

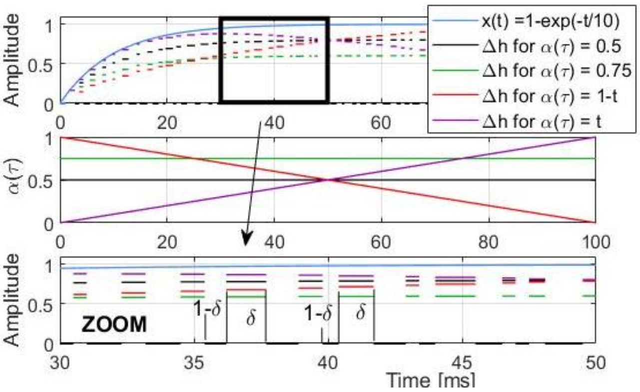

Fig. 6. The comparison of exponential discrete-continuous signal with different values of function $\alpha : P_{1-\delta,\delta} \longrightarrow \mathbb{R}$ (for $\alpha(t) = t$, $\alpha(t) = 1 - t$, $\alpha(t) = 0.5$ respectively) to the base function $x(t) = e^{-0.1t}$

In the second step, the influence of parameters a and b in function $x(t) = a\,sin(0.04t) + b, t \in P_{1-\delta,\delta}$, has been additionally analyzed. To this aim, again the base sinusoidal signal $x(t) = sin(0.04t)$ has been taken. The obtained result in Fig. 8 once again showed that the best customization to the base signal $x(t)$ has been achieved for the smallest values of both parameters of function $\alpha(\cdot)$. As a result, it leads to the conclusion that real industrial processes can be effectively controlled by using the discrete fractional control systems with variable sampling step and low values of the Grünwald-Letnikov – type fractional operator of functional order $\alpha : P_{1-\delta,\delta} \longrightarrow \mathbb{R}$.

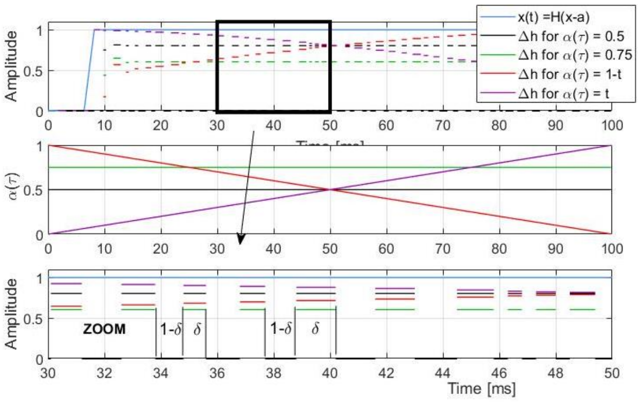

Fig. 7. The comparison of the Heaviside step function with delay discrete-continuous signal with different values of function $\alpha : P_{1-\delta,\delta} \longrightarrow \mathbb{R}$ (for $\alpha(t) = t$, $\alpha(t) = 1 - t$, $\alpha(t) = 0.5$ respectively) to the base function $x(t) = H(t - a)$

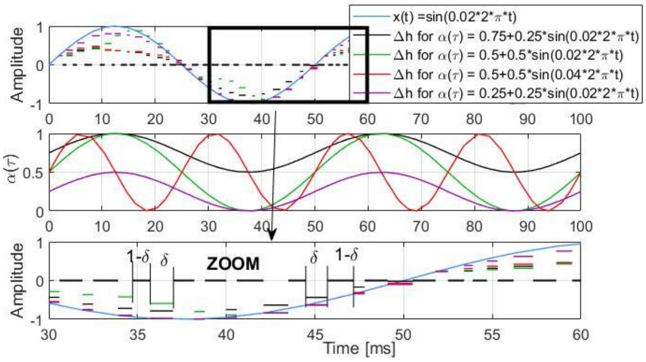

Fig. 8. The comparison of sinusoidal discrete-continuous signal with different values of function $\alpha : P_{1-\delta,\delta} \longrightarrow \mathbb{R}$ (for $\alpha(t) = t$, $\alpha(t) = 1 - t$, $\alpha(t) = 0.5$ respectively) to the base function $x(t) = a\sin(0.04t) + b$

Consequently, taking into account Figs. 4–7, it can be concluded that real industrial processes can be effectively controlled by using the discrete fractional control systems with variable sampling step and low values of the Grünwald-Letnikov – type fractional operator of functional order $\alpha : P_{1-\delta,\delta} \longrightarrow \mathbb{R}$.

5. CONCLUSIONS

The realization problem for Grünwld-Letnikov fractional operator with a measurable order on continuous-discrete time scale was studied. For this aim, firstly, some parameters from time scale calculus associated with sampling time (uniform and non-uniform) used in the measurement instruments like backward graininess was discussed. The proposed approach allowed to suppose that the process of charging and discharging of the capacitor inbuilt to the measurement cards of A/D and D/A converters could also be uniform. As a result, the practical implementation of the proposed approach for the measurement process can lead to reduction of consumption energy needed to control some industry processes by real time processor. Next, the proposed approach was checked in the simulation analysis. In order to do this, three base discrete-continuous signals $x(\cdot)$, such as sinusoidal signal, the Heaviside step function and exponential function for constant and changeable values of function order $\alpha(\cdot)$, were considered. The obtained results, given in Figs. 4–7 for the given signals on time domain $P_{1-\delta,\delta}$, showed that the signal Grünwald-Letnikov – type fractional operator of functional order $\alpha : P_{1-\delta,\delta} \longrightarrow \mathbb{R}$ is best customized to the base function $x(\cdot)$ for even smaller values of the function $\alpha : P_{1-\delta,\delta} \longrightarrow \mathbb{R}$ also of a function that has increasingly smaller values.

Finally, it can be concluded that real industrial processes can be effectively controlled by using the discrete fractional control systems with variable sampling step and low values of the Grünwald-Letnikov type fractional operator with variable order defined on continuous-discrete time domain.

REFERENCES

1. **Alagoz B.B., Tepljakov A., Ates A.** (2019) Time-domain identification of one noninteger order plus time delay models from step response measurements, *International Journal of Modeling, Simulation and Scientific Computing,* Vol. 10, No. 1, 1941011-1–1941011-22.
2. **Alagz B.B., Alisoy H**. (2018) Estimation of reduced order equivalent circuit model parametres of batteries from noisy current and voltage measurements, *Balkan Journal of Electrical & Computer Engineering*, Vol. 6, No. 4, 224–231.
3. **Balaska H., Ladaci S., Djouambi A., Schulte H., Bourouba B.** (2020) Fractional order tube model reference adaptive control for a class of fractional order linear systems *International Journal of Applied Mathematics and Computer Science*,, Vol. 30, No. 3, 501–515
4. **Bohner M., Petrson A.** (2002) Dynamic Equations on Time Scales: A survey, *Journal of Computational and Applied Mathematics*, Vol. 141, No. 1–2, 1–26.
5. **Buslowicz M. Nartowicz T.** (2009) Design of fractional order controller for a class of plants with delay, *Measurement Automation and Robotics*, Vol. 2, 398–405.
6. **Coimbra C**.,(2003), Mechanics with variable-order differential operators, *Annual Physics*, Vol. 12, 692-703.
7. **Djennoune S., Bettayeb M., Al-Saggaf U.M**. (2019) Synchronization of fractional order discrete-time chaotic systems by exact state reconstructor: application to secure communication, *International Journal of Applied Mathematics and Computer Science*, Vol. 29, No. 1, 179–194.
8. **Janczak J., Kondratiuk M., Pawluszewicz E**. (2016) Testing of adaptive non-uniform sampling switch algorithm with real-time simulation-in-the-loop, *Control and Cybernetics*, Vol. 45, No. 3, 317–328.
9. **Kavuran G., Yeroğlu C., Ates A. Alagoz B.B.** (2017) Effects of fractional order integration on ASDM signals, Int. J. Dynam. Control Vol. 5, 10–17
10. **Kondratiuk M., Ambroziak L., Pawluszewicz E, Janczak J.** (2018) Discrete PID algorithm with non-uniform sampling Practical implementation in control system, *AIP Conference Proceedings* 2029, 020029, doi: 10.1063/1.5066491.
11. **Koszewnik A., Ostaszewski M., Pawłuszewicz E., Radgowski P.** (2018) Performance Assessment of the Tilt Fractional Order Integral Derivative Regulator for Control Flow Rate in Festo MPSR©PA Compact Workstation, *Proceedings of 23rd International Conference on Methods and Models in Automation and Robotics,* Poland.
12. **Koszewnik A., Pawluszewicz E., Nartowicz T**., (2016), Fractional order controller to control pomp in Festo MPS® PA Compact Workstation, Proceedings of the 17th International Carpathian Control Conference (ICCC 2016), 364–367.
13. **Lorenzo C.F., Hartley T.T.** (2002) Variable order and distributed order fractional operators, *Nonlinear Dynamics*, Vol. 29, 57–98.
14. **Ortigueira M., Torres D.M.F., Trujillo J**. (2016) Exponents and Laplace transforms on non-uniform time scale, *Communications in Nonlinear Science and Numerical Simulations*, Vol. 39, 252–270.
15. **Ortigueira M.D.** (1997) Fractional discrete-time linear systems, *Proceedings of the EEICASSP*, Munich, Germany, IEEE New York, Vol. 3, 2241–2244.
16. **Ostalczyk P**. (2012) Variable- fractional-order discrete PID controller, *IEEE Proceedings of the 17th International Conference on Methods and Models in Automation and Robotics, MMAR 2012*, Miedzyzdroje, Poland, 534–539.
17. **Ostalczyk P., Duch P. Brzezinski D.W., Sankowski D**. (2015) Order functions selection in the variable-, fractional-order PID controller in: *Advances in modelling and control of non-integer-order systems*, Eds. Latawiec K.J., Lukaniszyn M., Stanislawski R., 159–170.
18. **Patniak S., Hollkamp J.P., Semperlotti A.** (2002) Applications of variable-order fractional operators: a review, *Proceedings of the Royal Society A*, 476, 1–32.
19. **Pawluszewicz E., Koszewnik A**., (2019), Markov parameters of the input-output map for discrete-time order systems with Grünwlad-Letnikov h-difference operator, Proceedings of the 24th International Conference on Methods and Models in Automation and Robotics (MMAR), 456–459.
20. **Podlubny , I., Dorcak, L., Misanek, J.** (1995) Application of fractional order derivatives to calculation of heat load intensity change in blast furnace walls, *Transactions of Technical University of Kosice*, Vol. 5, 137–144.
21. **Samko S.G., Ross B.** (1993) Integration and differentiation to a variable fractional order, *Journal Integral Transforms and Special Functions,* Vol. 1, No. 4, 277–300.
22. **Sierociuk D., Macias M**. (2013) Comparison of variable fractional order PID controller for different types of variable order derivatives, *Proceedings of the 14th International Carpathian Control Conference ICCC 2013*, Rytro, Poland, 334–339.
23. **Sierociuk D., Malesza W**., **Macias M.** (2013) On a new definition of fractional variable-order derivative, *Proceedings of the 14th International Carpathian Control Conference ICCC 2013*, Rytro, Poland, 339–345.
24. **Sierociuk D., Malesza W., Macias M**. (2015) Deviation, interpolation and analog modelling of fractional variable order derivative definitions, *Applied Mathematics and Modelling*, Vol. 39, 3876–3888.
25. **Stanislawski R., Latawiec K**. (2012) Normalized finite fractional differences: computational and accuracy breakthrough, *International Journal of Applied Mathematics and Computer Science*, Vol. 22, No. 4, 907–919.
26. **Tepljakov A.** (2017) *Fractional-order modeling and control of dynamic systems,* Springer-Verlag.
27. **Tepljakov A., Alagoz B.B. et al.** (2018) FOPID controllers and their industrial applications: a survey of recent results**,** *IFAC Papers On Line* 51-4, 25–30.
28. **Tepljakov A., Petlekov E., Belikov J.** (2012) A flexible Matlab tool for optimal fractional-order PID controller design subject to specifications**,** *Proceedings of the 31st Chinese Control Conference*, 4698–4703.
29. **Valerio D., Sa da Costa J.** (2001) Variable-order fractional derivatives and their numerical approximations, *Signal Processing*, Vol. 91, 470–483.
30. **Wang J.C**. (1987) Realizations of generalized Warburg impedance with RC ladder networks and transmission lines, *Journal of Electrochemical Society*, Vol. 134, No. 8, 1915–1920.

Acknowledgment: The work is supported with University Works No WZ/WM-IIM/1/2019 (A. Koszewnik and E. Pawluszewicz) and WI/WM-IIM/7/2020 (P. Burzyński) Faculty of Mechanical Engineering, Bialystok University of Technology.

sciendo

DOI 10.2478/ama-2020-0024

TEMPERATURE VARIATION EFFECT ON THE ACTIVE VIBRATION CONTROL OF SMART COMPOSITE BEAM

Mostefa SALAH,* Farouk B. BOUKHOULDA,* Mohamed NOUARI, Kouider BENDINE***

*Structures and Solid Mechanical Laboratory, Mechanical Department, Djillali Liabes University of SidiBel- Abbes,
BP 89 Cité Ben M'Hidi Sidi Bel-Abbès 22000, Algéria.
**University of Lorraine, Laboratoire d'Etude des Microstructures et de Mécanique des Matériaux,
LEM3 CNRS-UMR 7239, GIP-INSIC, 27 Rue d'Hellieule, 88100 Saint-Dié-des-Vosges, France.

mostefa.salah@yahoo.fr, boukhoulde22000@yahoo.fr, nouari.mohamed@univ-nancy.fr, bendine.k@live.fr

received 14 January 2020, revised 17 November 2020, accepted 19 November 2020

Abstract: Due to their impressive capacity of sensing and actuating, piezoelectric materials have been widely merged in different industrial fields, especially aeronautic and aerospace area. However, in the aeronautic industry, the structures are operating under critical environmental loads such as high and very low temperature, which made the investigation of the effect of thermal forces on the piezoelectric structures indispensable to reach the high functionality and performance. The present paper focuses on the effect of thermal loads on the active vibration control (AVC) of structures like beams. For this purpose, a finite element model of composite beam with fully covered piezoelectric sensor and actuator based on the well-known high order shear deformation theory is proposed by taking into account the electrical potential field and a linear temperature field. Hamilton's principle is used to formulate the electro-thermo-mechanical governing equations. The negative velocity feedback controller is implemented to provide the necessary gain for the actuator. Different analyses are effectuated to present the effect of the temperature ranging from -70°C to 70°C on the active vibration control of the composite beam.

Keywords: Piezoelectric, thermal loads, beams, active vibration control, Hamilton's principle

1. INTRODUCTION

Structures made of composite materials are intensively used in different industrial sectors (Gay and Hoa, 2007). Due to their light weight, rigidity and high physical properties, they can be found especially in aeronautic and aerospace technology. These structures are subjected to different type of critical loads, which lead to huge amount of vibrations. The vibrations are mostly undesirable and significantly affect the composite structures and cause their failure and damage (Zou et al., 2000). To prevent the failure of the composite structures caused by the vibration, the research community proposed a variety of solutions, among them passive, semi active and active vibration control. The passive damping techniques (PDT) (Johnson, 1995) is based on the integration and the addition of materials or systems, possessing high damping properties, into the structure in such a way that the vibrations can be absorbed by the developed damping system without any further outside interference. However, these techniques have certain limitations: their performance is limited in the low frequency domain, the size can be important and the damping coefficient is especially dependent on temperature and frequency. Semi-active control methods are well known in the context of structural vibration using piezoelectric actuator to dissipate energy caused by the system's motion (Clark, 1999). The main benefit is that no additional energy is added to the system, and their implementation does not require any sophisticated signal processing systems or any bulky power amplifier (Qiu et al., 2009), which guarantees stability of the whole system. In addition, semi-active methods are more efficient than the passive ones, but always with a lower efficiency in comparison to the active methods. The last technique, which is the main objective of this study, is the based on piezoelectric active vibration control (AVC). It is inspired by the phenomena of piezoelectricity in certain materials (Ye, 2008), the AVC techniques are gradually merged in different fields (Crawley and De Luis, 1987). It consists of four main keys, the structure itself, the sensor, the actuator and the control algorithms. Thus, it requires bonding piezoelectric patches in a conventional structure to create a kind of smart structure, which have the ability of self-control.

An explosion of research papers have been focused on the finite element modelling of the AVC using piezoelectric materials. Lam et al. (1997) developed a finite element model for piezoelectric composite laminate based on the classical plate theory. Peng et al. (1998) introduced a finite element model using the well-known third order laminate theory for the active vibration control of composite beams with distributed piezoelectric sensors and actuators. Elshafei and Alraiess (2013) suggested a finite element formulation for modelling and analysis of isotropic as well as orthotropic composite beams with distributed piezoelectric actuators subjected to both mechanical and electrical loads. Bendine et al. (2016) proposed a finite element method (FEM) to study the active vibration control smart FGM beam based on higher-order shear deformation theory, the authors analyzed different types of loading and provided a displacement feedback controller to reduce the vibrations. Beheshti-Aval et al. (2011) introduced a three nodded beam finite element of composite laminated beam with distributed piezoelectric sensor/actuator layers for the static analysis. Kargarnovin et al. (2007) considered a simply supported

FGM plate bonded with piezoelectric patches; the model equation of motion is derived using classical laminated plate theory CLPT. Tzou and Tseng (1990) derived a new piezoelectric finite element with internal degree of freedom for modelling a shell or plate structures containing distributed piezoelectric sensor and actuator. Tzou and Gadre (1989) established an experimental work to model active vibration suppression of a multi-layered shell coupled with piezoelectric actuators.

Otherwise, the composite structures are used under a high critical environmental thermal field, especially in aerospace sector. This variation in temperature effects the system performance and, in particular, their dynamic responses. Recently, a great number of researches have focused on the analysis of piezothermoelastisity. Lee and Saravanos (1996) developed and implemented a finite element equation to a beam element with linear shape function to model mechanical, electrical and thermal responses of composite beam integrated with piezoelectric patches. Zhou et al. (2000) used a higher order temperature field to describe the temperature distribution through the thickness of a composite plate; a thermo-piezoelectric-mechanical theory is adopted to model dynamic response of a composite plate bonded with piezoelectric actuator. Bansal and Ramaswamy (2002) investigated the dynamic as well as static thermal responses of laminated composites bonded with piezoelectric layers by using a four node finite element formulation, which have five mechanical degrees of freedom per node. Lee and Saravanos (1998) implemented finite element equations for beams and plates to model active response of piezoelectric composite laminate taking into account the thermal effect on the material properties. Liew et al. (2001) presented a finite element formulation to model active control of functionally gradient material FGM plate integrating with piezoelectric layers, the model is based on the first shear deformation theory and he subjected to a thermal gradient. Jiang and Li (2007) used a negative velocity feedback for active vibration control of a composite beam distributed with piezoelectric sensor and actuator layers subjected to a thermal excitation, the finite element model is based on a high-order displacement field. Raja et al. (2004) derived the finite element actuator and sensor using a nine nodded field consistent shallow shell element to analyze piezohygrothermoelastic laminated plates and shells. Gupta et al. (2011) introduced AVC of a smart cantilever plate using negative velocity feedback control at elevated temperature ranging from 25°C to 75°C. Sharma et al. (2016) investigated the dynamic response and the AVC of cantilever structure over a temperature range (-70°C–70°C) experimentally and numerically, the model is based on the first order shear deformation theory. Song et al. (2004) presented a numerical and experimental study of active reduction of deformation due to thermal effect of a composite beam using piezoelectric ceramic actuators. Birman (1996) studied the effect of temperature on piezoelectric sensors and on a composite layer. Chandrashekhara and Tenneti (1995) developed an FEM for the active control of thermally induced vibration of laminated composite plate bonded with piezoelectric actuators. Chattopadhyay et al. (1999) applied the principle of free energy and Hamilton's principle to obtain differential equations to modelling a coupled thermo-piezoelectric-mechanical of composite laminate bonded with piezoelectric actuators in the surface.

In the previous paper, the piezoelectric coefficients' values were assumed to be independent of temperature, which is not correct. The present paper proposes a finite element formulation of composite beam based on the well-known high order shear deformation theory. The piezoelectric coefficients were supposed to be dependent on temperature. Two types of analysis are considered, which include static and dynamic responses. A negative velocity feedback algorithm is used to provide the necessary gain for the active vibration control of the composite beam. Different results are presented to prove the efficiency of the proposed model.

2. HAMILTON'S PRINCIPLE

As presented in Fig. 1, a laminated beam with two piezoelectric films bounded on its top and bottom surfaces is considered in this study. To derive the structure thermoelectromechanical equations, the well-known Hamilton's principle, which assumes that the energy variation over an arbitrary period of time equals zero, is used.

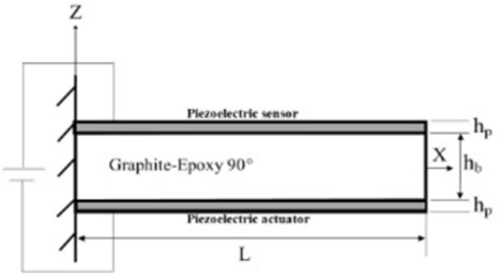

Fig. 1. Cantilever graphite-epoxy Beam (90°) distributed with piezoelectric patches

The mathematical statement of Hamilton's principle, which explains the variation of integration of the total energy, can be expressed as follows:

$$\int_{t_1}^{t_2} \delta(T-P)dt = 0 \tag{1}$$

where T and P are respectively the kinetic and the potential energies of the structure that can be defined as (Tzou and Bao, 1995):

$$T = \int_{v} \left(\frac{1}{2}\rho\dot{u}\dot{u}\right) dv \tag{2}$$

$$P = \int_{V} \left[M\left(\sigma_i, E_j, \theta_a\right) + \Omega\theta_a\right] dv - \int_{S} \left[s_j u - q_j \lambda\right] ds \tag{3}$$

We noted here that u and $\dot{u}$ are the displacement and velocity, σ_i , E_j are the strain and the electric field, $\theta_a$is the absolute temperature and Ω is the thermal entropy density, ρ,M and q_i is the mass density, the electric enthalpy and the surface electric charge ,s_j is the surface traction in the J direction and λ is the electrical potential. V and S are the volume and surface of the piezothermoelastic continuum.

The electric enthalpy M can be formulated as:

$$M = \frac{1}{2}\{\sigma\}^t[C]\{\sigma\} - \frac{1}{2}\{E\}^t[d]\{E\} - \frac{1}{2}a\theta^2 - \{E\}^t[p]\{\sigma\} - \{\chi\}^t\{\sigma\}\theta - \{\kappa\}^t\{e\}\theta \tag{4}$$

where $\{\sigma\}$, $\{E\}$, $\{\chi\}$ and $\{\kappa\}$ denote respectively strain vector, electric field, stress temperature and pyroelectric coefficient vector and$[C]$, $[d]$ and $[p]$ represent lastic stiffness, dielectric permittivity and piezoelectric coefficient matrix.

We noted that θ is the temperature rise and α_v is a material coefficient done by $\alpha_v = \rho c_v \theta_0^{-1}$, where c_v is the specific heat and θ_0 is the temperature of the natural plane.

Using Eq. (2) and (3) and including the electric enthalpy formula Eq. (4), the Hamilton's equation for the laminated piezoelectric beam can be rewritten as:

$$\int_{t_0}^{t_1} \int_v \frac{1}{2} \rho \delta(u)^2 dV dt - \int_{t_0}^{t_1} \int_v (\{D\}^t \Delta(\delta\lambda) + \{S\}^t \delta\{\sigma\}) dV dt + \int_{t_0}^{t_1} \int_v \left(t_f \delta u_f - q_j \delta\lambda\right) dS dt = 0 \tag{5}$$

3. PIEZOTHERMOELASTIC CONSTITUTIVE EQUATIONS

According to Benjeddou and Andrianarison (2005), the piezothermoelastic field, which is by definition the elasto-electric-thermal interactions, is given by:

$$\begin{gathered} \{S\} = [C]\{\sigma\} - [p]^T\{E\} - \{\chi\}\theta \\ \{D\} = [p]\{\sigma\} + [d]\{E\} + \{\kappa\}\theta \\ \Omega = \{\chi\}\{\sigma\} - [\kappa]^T\{E\} + a\theta \end{gathered} \tag{6}$$

It must be noted that $\{S\}$, $\{D\}$ and Ω are respectively the stress, electric displacement and thermal entropy density vector.

4. DISPLACEMENT AND STRAIN

According to Reddy (1984) and Zorić et al. (2013) and based on a simple higher-order shear deformation theory, the displacement field can be written as following (Eq. 7):

$$\begin{cases} u(x,z,t) = u_0(x,t) - z\dfrac{dw(x)}{dx} + (z - z^3\dfrac{4}{3h^2})\varphi_x(x,t) \\ w(x,z,t) = w_0(x,t) \end{cases} \tag{7}$$

where: (u, w) and (u_0, w_0) are the displacements of any point and the mid-plane displacement in the x and z directions. φ_x is the bending rotation of the mid-plane and h is the total thickness of the composite structure.

From Eq. (7), the strain equation can be derived as:

$$\begin{cases} \sigma_1 = \sigma_x = \frac{du}{dx} - z\frac{d^2w(x)}{dx^2} + (z - z^3\frac{4}{3h^2})\varphi_x(x,t) \\ \sigma_5 = \tau_{zx} = (z - z^3\frac{4}{3h^2})\varphi_x(x,t) \end{cases} \tag{8}$$

We noted here that τ is the shear strain. The strain and displacement Eq. (9) and (10) can be presented as:

$$u = a_u u_u \tag{9}$$

$$\varepsilon = l_u u_u \tag{10}$$

where:

$$a_u = \begin{bmatrix} 1 & -z\dfrac{d}{dx} & z - \dfrac{4z^3}{3h^2} \\ 0 & 1 & 0 \end{bmatrix} \tag{11}$$

$$l_u = \begin{bmatrix} \dfrac{d}{dx} & -z\dfrac{d^2}{dx^2} & z - \dfrac{4z^3}{3h^2} \\ 0 & 0 & 1 - \dfrac{4z^2}{h^2} 0 \end{bmatrix}$$

and,

$$\Omega = z^3 - \frac{4}{3h^2} \tag{12}$$

$$\varepsilon_{xx} = \varepsilon_{xx}^0 + z\varepsilon_{xx}^1 - \Omega\varepsilon_{xx}^3 \tag{13}$$

$$\tau_{xz} = \tau_{xz}^0 - z^2\frac{4}{h^2}\tau_{xz}^2 \tag{14}$$

5. FINITE ELEMENT FORMULATION

5.1. Mechanical field

In this work, the composite structure is modeled using the finite element method. Each beam element has two nodes with four mechanical degrees of freedom $\{u_e\} = \left\{u, w, \varphi_x, \frac{\partial w}{\partial x}\right\}$ at each node. One electric degree of freedom for each piezoelectric layer is also used. The axial displacement u and the rotation φ_x are expressed in the nodal displacement in the finite element model as follows (Zorić et al., 2013):

$$\begin{gathered} \xi_1 = (1 - \gamma)/2 \\ \xi_2 = (1 + \gamma)/2 \end{gathered} \tag{15}$$

where ξ_1 is the Lagrangian shape function.

The transverse displacement w is expressed in the finite element model by a Hermite cubic interpolation shape functions:

$$\begin{gathered} \theta_1 = 1/4(1 - \gamma)^2 (2 + \gamma) \\ \theta_2 = 1/4(2 - \gamma)(1 + \gamma)^2 \\ \theta_1' = 1/4(1 - \gamma)^2 (1 + \gamma) \\ \theta_2' = -1/4(1 - \gamma)(1 + \gamma)^2 \end{gathered} \tag{76}$$

where γ is the local coordinate define as:

$$\gamma = 2\frac{x}{l_e} - 1 \tag{87}$$

Putting Eq. 15, 16 and 17 into matrix form yields:

$$n_u = \begin{bmatrix} \xi_1 & 0 & 0 & 0 & \xi_2 & 0 & 0 & 0 \\ 0 & \theta_1 & 0 & \theta_1'\left(\frac{l_e}{2}\right) & 0 & \theta_2 & 0 & \theta_2'\left(\frac{l_e}{2}\right) \\ 0 & 0 & \xi_1 & 0 & 0 & 0 & \xi_2 & 0 \end{bmatrix} \tag{189}$$

The displacement vector and the strain vector can be expressed as follows:

$$u = a_u u_u = a_u n_u u_u^e = n u_u^e \tag{10}$$

$$\varepsilon = l_u u_u = l_u n_u u_u^e = b_u u_u^e \tag{20}$$

where n is the displacement interpolation matrix and b_u is the strain interpolation matrix.

5.2. Electric field

The electric potential along the kth piezoelectric layer is assumed to be a cubic form, and may be presented as:

$$\phi^k(x,y,\widetilde{z}) = p_1^k(\tilde{z})E_1^k(x,y) + p_2^k(\tilde{z})E_b^k(x,y) + p_3^k(\tilde{z})\phi^k(x,y) \qquad (21)$$

where: $e_1^k(x,y)$, $e_b^k(x,y)$ are the electric fields at the top and the bottom surface. $\phi^k(x,y)$ is the difference in potential between the top and bottom surface. $p_1^k, p_2^k and\ p_3^k$ are the interpolation functions that can be given by:

$$p_1^k = -\left(\tilde{z}+\frac{1}{2}\right)^2\left(\tilde{z}-\frac{1}{2}\right)h_k$$
$$p_2^k = -\left(\tilde{z}+\frac{1}{2}\right)\left(\tilde{z}-\frac{1}{2}\right)^2 h_k \qquad (22)$$
$$p_3^k = 3\left(\tilde{z}+\frac{1}{2}\right)^2 - 2\left(\tilde{z}+\frac{1}{2}\right)^3 - \frac{1}{2}$$

It is to be noted that $\mathrm{h_k}$ and $\tilde{\mathrm{z}}$ are the thickness of the kth piezoelectric layer and the local thickness coordinate of the kth piezoelectric layer respectively, $\tilde{\mathrm{z}}\epsilon[-1/2 \rightarrow 1/2]$

$$\tilde{z} = \frac{z}{h_k} - \frac{z_t^k z_b^k}{2h_k} \qquad (23)$$

$z_t^k$and z_b^k are respectively the z-axis coordinate for the top and bottom surfaces of the kth piezoelectric layer. The electric field vector $E_k$for each layer is by definition the gradient of the electric potential, thus, the electric field can be formulated as follow:

$$E_k = \begin{bmatrix}E_x\\E_z\end{bmatrix} = \begin{Bmatrix}-\dfrac{\partial\emptyset}{\partial x}\\-\dfrac{\partial\emptyset}{\partial z}\end{Bmatrix} = -\begin{bmatrix}p_1^k\dfrac{d}{dx} & p_2^k\dfrac{d}{dx} & p_3^k\dfrac{d}{dx}\\\dfrac{dp_1^k}{dz} & \dfrac{dp_2^k}{dz} & \dfrac{dp_3^k}{dz}\end{bmatrix}\begin{Bmatrix}E_t^k\\E_b^k\\\overline{\Phi^k}\end{Bmatrix} = -l_\Phi^k U_\Phi^k \qquad (24)$$

It is worth to be noted that the potential in the y direction can be taken as $\mathrm{E_y} = 0$.

5.3. Thermal field

Assuming that the temperature field is a linear function through the thickness of the beam, hence, the temperature field can be interpolated as:

$$\theta(x,z) = \left(\frac{1}{2}-\frac{z}{h}\right)\theta_b(x) + \left(\frac{1}{2}+\frac{z}{h}\right)\theta_t(x) = B_\theta\theta \qquad (25)$$

where θ_t and θ_b are the top and bottom surface temperature, B_θ is the linear interpolation vector for the temperature variation.

6. GOVERNING EQUATION

With the help of Eq. 6, 7, 8, 9 and using Eq. 5, 10 and 11 and taking into account the damping effect, we get the dynamic matrix equations as follow:

$$m\ddot{u}_u + C_{uu}u_u + C_{ua}u_a + C_{us}u_s = f_u + k_{u\theta}\theta \qquad (11)$$

$$K_{au}u_u - e_{aa}u_a = -f_a - k_{a\theta}\theta \qquad (27)$$

$$K_{su}u_u - e_{ss}u_s = -f_s - k_{s\theta}\theta \qquad (128)$$

where m, $\mathrm{C_{uu}}$, $\mathrm{C_{ui}}$ and $\mathrm{k_{u\theta}}$ are respectively the mass, the elastic, the matrix coupling electric-mechanical for actuator and sensor and the matrix coupling thermal-mechanical, and $\mathrm{e_{aa}}$, $\mathrm{k_{k\theta}}$, $\mathrm{f_u}$ and $\mathrm{f_s}$ are the permittivity matrix for actuator and sensor, the matrix coupling electric-thermal for actuator and sensor, the mechanical load vector and the applied charge vector; which are of the form:

$$m = \int_\mathrm{v} \rho n^t n dv \qquad (139)$$

$$C_{uu} = \int_\mathrm{v} b_u^t C b_u dv \qquad (30)$$

$$C_{ui} = \int_\mathrm{v} b_u^t \sigma^t b_\phi dv \ \ ; i = (c,a) \qquad (31)$$

$$k_{u\theta} = \int_\mathrm{v} b_u^t \chi b_\theta dv \qquad (32)$$

$$C_{kk} = \int_\mathrm{v} b_\phi^t d_k b_\phi dv \ \ ; k = (c,a) \qquad (33)$$

$$k_{k\theta} = \int_\mathrm{v} b_\phi^t \kappa_k b_\theta dv \ \ ; k = (c,a) \qquad (34)$$

$$f_u = \int_\mathrm{v} n^t f_b dV + \int_{\mathrm{S}_f} n^t f dS + n^t f_c \qquad (35)$$

$$f_k = \int_\mathrm{v} n_\phi^t f_k^t q ds \ \ ; k = (c,a) \qquad (36)$$

6.1. Negative velocity feedback strategy

It should be noted that in this study, we introduce a controller to damp the vibrations caused by the external excitation. A negative velocity feedback controller is considered in order to have good stability and robustness properties. The electrical potential is to be the feedback to the actuator, and is calculated as:

$$\{V\}_a = G_v\{V\}_s \qquad (14)$$

where G_v is the control gain.

7. RESULTS AND DISCUSSION

In order to validate the present FE model, a benchmark cantilever beam bonded by piezoelectric along the upper and bottom surface as shown in Fig. 1 is proposed. The beam dimensions are: length L = 0.5 m, with 0.1 m and thickness h = 0.001 m. The FEM model is composed of four layers, the stacking sequence is [90°/90°/90°/90°]. The material properties of the structure are listed in the Table 1.

Tab. 1. Material proprieties(Jiang and Li, 2007)

Proprieties	*Graphite-Epoxy*	*PZT*
Poison's ratio υ_{12}=υ_{13}=υ_{23}	0.33	0.33
Density $\rho(kg/m^3)$	1600	7750
Elastic stiffness matrix $E(GN/m^2)$	$E_{11} = 180$, $E_{22} = E_{33} = 10$	$E_{11} = E_{22} = E_{33} = 60$,
Shear modulus $G(GN/m^2)$	$G_{11} = G_{13} = 8$, $G_{23} = 3$,	$G_{11} = G_{13} = G_{23} = 22.5$
Thermal expansion A	$A_1 = 2.4x10^{-8}$, $A_2 = A_3 = 2.4x10^{-5}$	$A_1 = A_2 = A_3 = 1.2x10^{-6}$
Electric permittivity $d(F/m)$	--	$d_{11} = d_{22} = d_{33} = 150x10^{-10}$
Piezoelectric strain matrix e	--	$e_{31} = 6.5, e_{33} = 23.3, e_{15} = 17$
Piezoelectric compliance $d(C/N)$	--	$d_{15}{=}d_{24} = 6x10^{-10}$, $d_{31} = d_{32} = -1.7x10^{-10}$ $d_{33} = 3.5x10^{-10}$
Pyroelectric constant $\kappa(c/km^2)$	--	$\kappa_3 = -2.5x10^{-5}$

Two cases are considered to validate the proposed model. the first case, the beam has been subjected to a temperature gradient of 5, 10, 20 and 50°C, as shown in Fig. 2, the deflection is upwards and proportional to the temperature, which is quite normal due to the fact that temperature in the bottom is higher than the top surface. The results are validated using the study of Jiang and Li (2007).

The second validation case seeks the effect of pyroelectric and thermal strain effect, as shown in Fig. 3; the thermal strain effect is much more significant than the pyroelectric effect. Those results are confirmed by the study of Jiang and Li (2007).

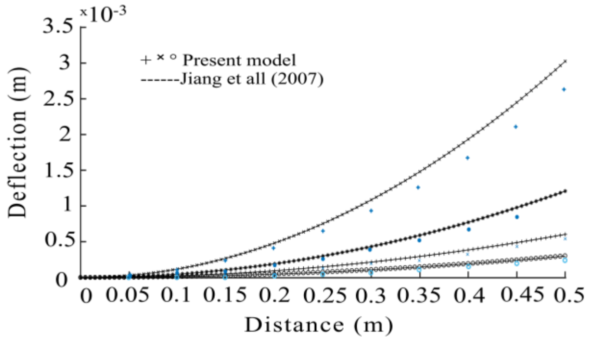

Fig. 2. Beam deflection along the length of the beam (+50°C, ● 20°C, * 10°C, ○ 5°C)

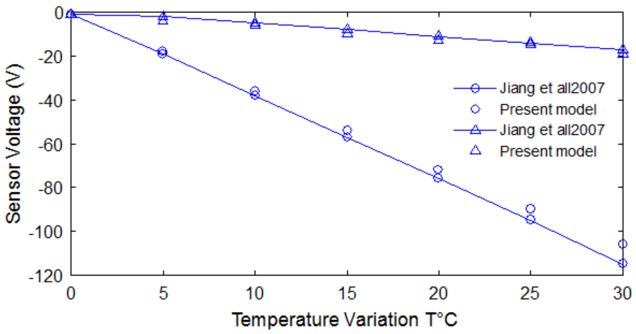

Fig. 3. Pzt sensor voltage due to temperature variation (o Thermal strain effect , Δ Pyroelectric effect)

7.1. Temperature effect on the active vibration control

In the area of active vibration control, most research papers consider that the piezoelectric stress coefficients and permittivity are independent of the temperature, which is quite incorrect due to the fact that the coefficients are highly sensitive to the temperature and their change can be described as linear when it comes to the stress coefficients and nonlinear for the case of permittivity (Gupta et al., 2011). In the present work, we considered the variations in piezoelectric and permittivity coefficients versus the temperature in the bandwidth of [-70°C to +70°C] for the case of lead zirconate titanate ceramic PZT-5H, which are provided by the experimental investigation done by Wang et al. (1998), which is shown in Table 2.

Tab. 2. Dielectric constant and permittivity coefficient of piezoelectric materials versus temperature (Sharma et al., 2016)

Temperature $(°C)$	Piezoelectric constant $(d_{31})10^{-12}$ (pC/N)	Dielectric constant $(k_{33})10^{-9}$ (F/m)
-70	1.6	1.67
-50	1.84	1.92
-25	2.13	2.22
0	2.43	2.49
25	2.72	2.84
50	3	3.11
70	3.24	3.34

To study the performance of the active vibration control under the aforementioned thermal bandwidth, the structure under study is subjected to an external transient load of 10 N at the free end for a duration of 1 ms. The control gain is calculated using negative velocity feedback algorithm, while the structural damping is taken to be 1 %. The beam displacement for both control on and control off are presented in Fig. 4. Seven different values of temperature [-70,-50,-25,0,25,50,70]°C have been tested. The results show that the efficiency of the piezoelectric layer on the control system is decreasing when the temperature is decreased, which agreed with the previous static analysis finding and can be explained by the fact that the piezoelectric coupling coefficient d31 is increasing proportionally with the temperature.

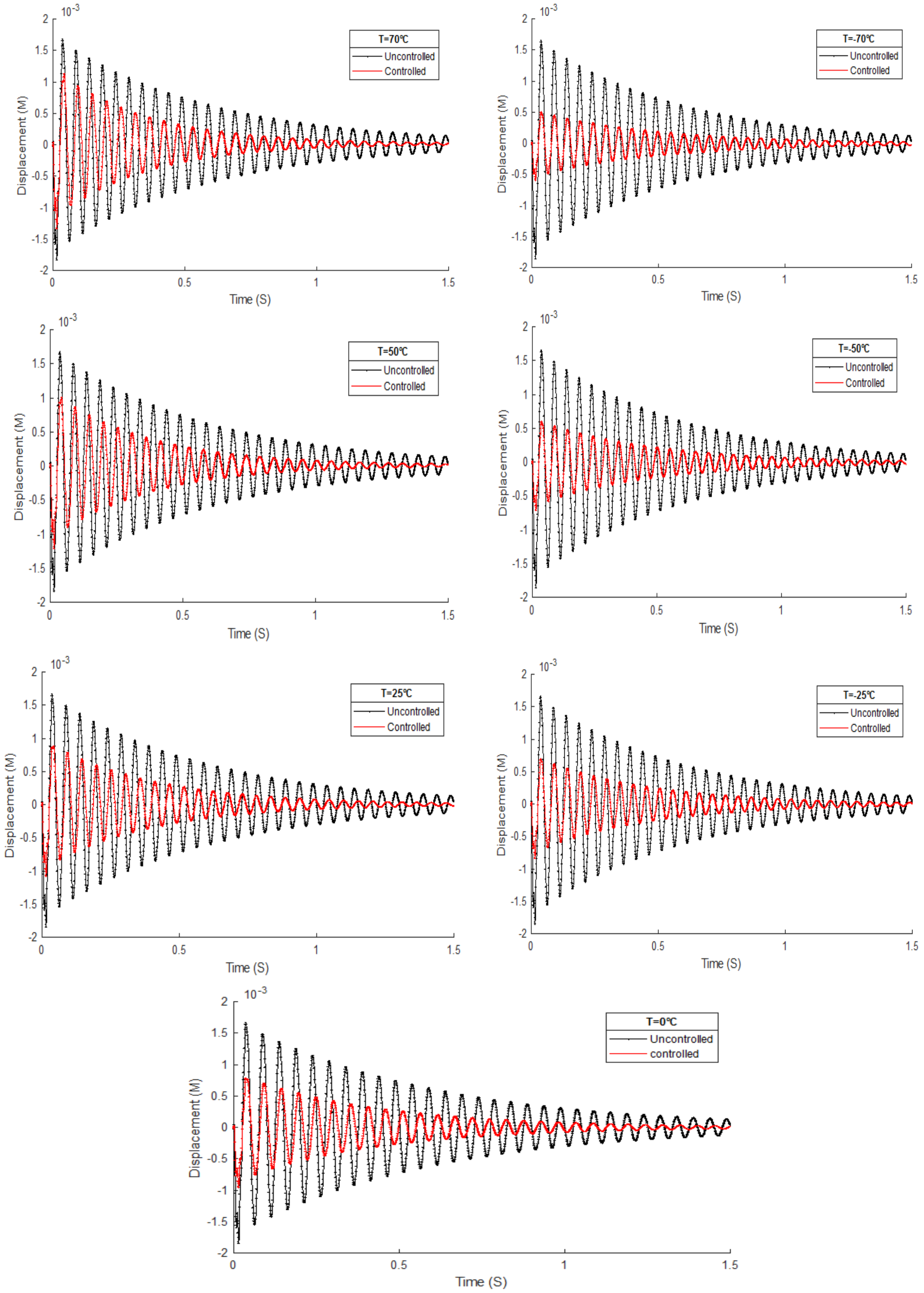

Fig. 4. Controlled dynamic response with a different thermal gradient (-70°C to 70°C)

The controlled and uncontrolled sensor signal at the previously mentioned temperature ranged is shown in Fig. 5. It can be observed that the sensor signal increase with temperature, which proved the accuracy of the proposed control algorithm. The same control behavior as the displacement is noticed for the investigated temperature.

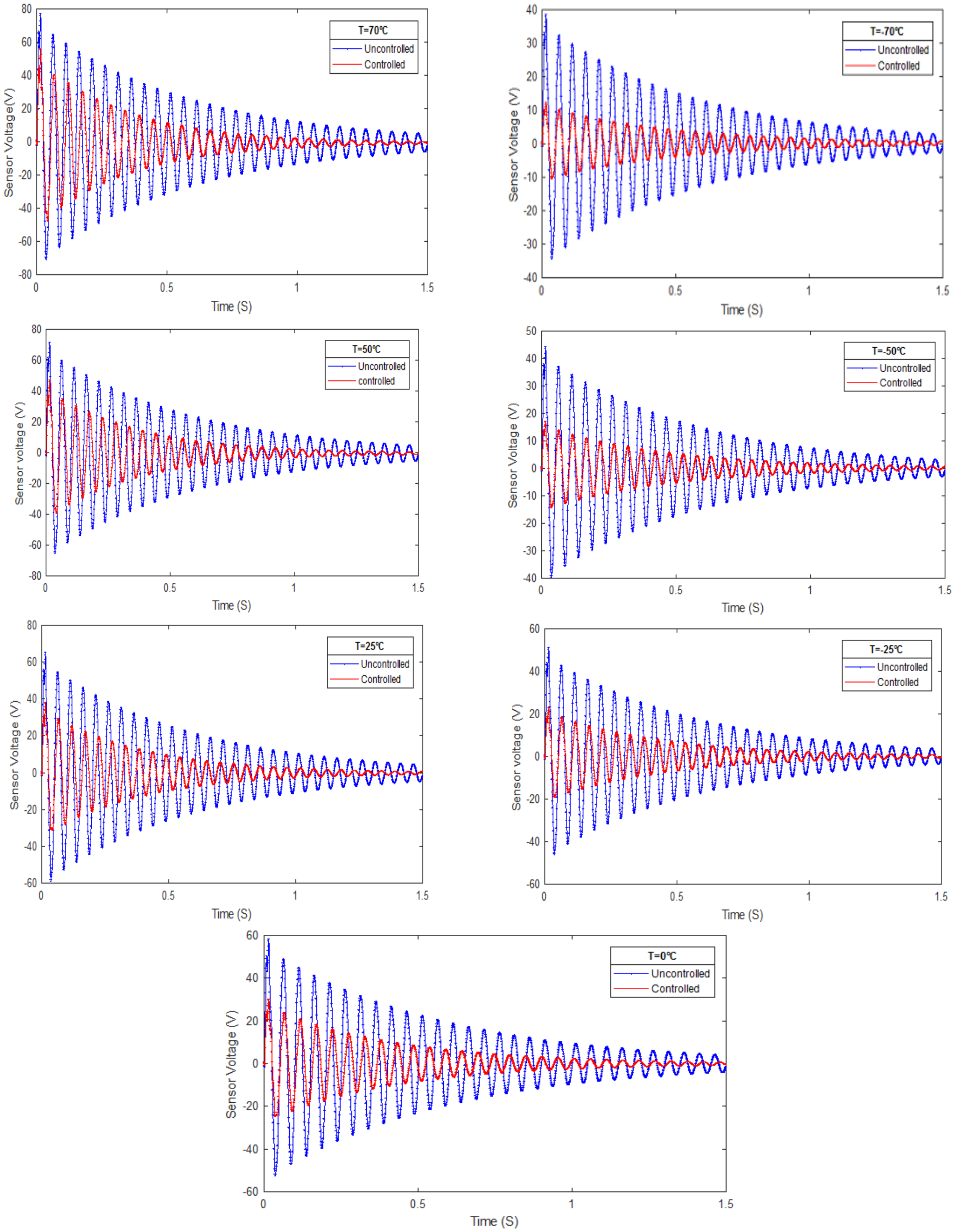

Fig. 5. Pzt sensor voltage due at different temperature

The actuator voltage with consideration of the range of temperature are depicted in Fig. 6. As it is clearly shown in the figure, the actuator voltage is proportional to the temperature.

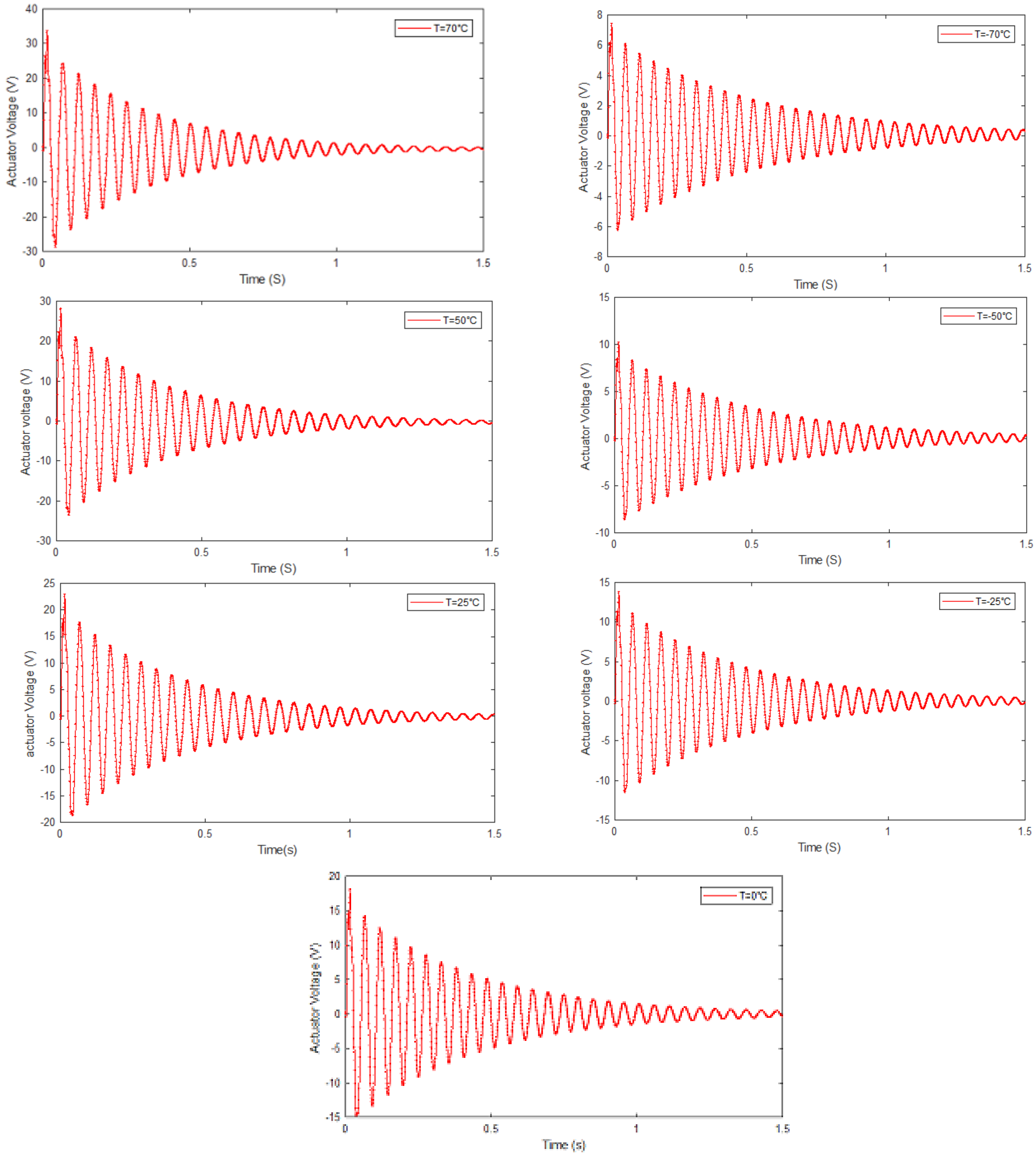

Fig. 6 Pzt actuator voltage versus time in different temperature 70°C, 50°C, 25°C, 0°C

8. CONCLUSION

In this paper, the finite element formulation for the laminated composite beam bounded by full recovery piezoelectric sensors and actuators has been developed for the purpose of AVC. The negative velocity feedback control algorithm is designed and implemented to provide the control gain. The coupling between thermal and piezoelectric effect is mathematically described and investigated. The results show a high dependency of the control efficiency on the temperature. The piezoelectric sensor voltage contributed by the thermal strain effect is much more than that contributed by pyroelectric effect. So, the temperature must be included in constitutive equations. It is found that AVC performance is not maintained at a range of temperatures, if the control law ignores the temperature dependence of the PZT coefficients. However, AVC performance is maintained when the control law includes the temperature dependence of d31 and k33. This scheme can be implemented in all the applications of smart structures where piezoelectric materials are used as sensors and actuators.

REFERENCES

1. **Bansal A., Ramaswamy A.** (2002), FE analysis of piezo-laminate composites under thermal loads, *J. Intell. Mater. Syst. Struct.*, 13,

291–301.

2. **Beheshti-Aval S.B., Lezgy-Nazargah M., Vidal P., Polit O.** (2011), A Refined Sinus Finite Element Model for the Analysis of Piezoelectric-Laminated Beams , A Refined Sinus Finite Element Model for the Analysis of Piezoelectric-Laminated Beams, *J. Intell. Mater. Syst. Struct.*, 22, 203–219, https://doi.org/10.1177/1045389X10396955.
3. **Bendine K., Boukhoulda F.B., Nouari M., Satla Z.** (2016), Active vibration control of functionally graded beams with piezoelectric layers based on higher order shear deformation theory, *Earthq. Eng. Eng. Vib.*, 15, 611–620.
4. **Benjeddou A., Andrianarison O.** (2005), A thermopiezoelectric mixed variational theorem for smart multilayered composites, *Comput. Struct.*, 83, 1266–1276.
5. **Birman V.** (1996), Thermal effects on measurements of dynamic processes in composite structures using piezoelectric sensors, *Smart Mater. Struct.*, 5, 379, https://doi.org/10.1088/0964-1726/5/4/001.
6. **Chandrashekhara K., Tenneti R.** (1995), Thermally induced vibration suppression of laminated plates with piezoelectric sensors and actuators, *Smart Mater. Struct.*, 4, 281. https://doi.org/10.1088/0964-1726/4/4/008.
7. **Chattopadhyay A., Li J., Gu H.** (1999), Coupled Thermo-Piezoelectric-Mechanical Model for Smart Composite Laminates, *AIAA J.*, 37, 1633–1638, https://doi.org/10.2514/2.645.
8. **Clark W.W.** (1999), Semi-active vibration control with piezoelectric materials as variable-stiffness actuators, *Smart Structures and Materials: Passive Damping and Isolation*, International Society for Optics and Photonics, 123–130.
9. **Crawley E.F., De Luis J.** (1987), Use of piezoelectric actuators as elements of intelligent structures, *AIAA J.*, 25, 1373–1385.
10. **Elshafei M.A., Alraiess F.** (2013), Modeling and analysis of smart piezoelectric beams using simple higher order shear deformation theory, *Smart Mater. Struct.*, 22, 035006.
11. **Gay D., Hoa S.V.** (2007), *Composite Materials : Design and Applications*, Second Edition, CRC Press.
12. **Gupta V., Sharma M., Thakur N., Singh S.P.** (2011), Active vibration control of a smart plate using a piezoelectric sensor–actuator pair at elevated temperatures, *Smart Mater. Struct.*, 20, 105023.
https://doi.org/10.1088/0964-1726/13/1/004
https://doi.org/10.1115/1.3167719
https://doi.org/10.1201/9781420045208
13. **Jiang J.P., Li D.X.** (2007), A new finite element model for piezothermoelastic composite beam, *J. Sound Vib.*, 306, 849–864.
14. **Johnson C.D.** (1995), Design of Passive Damping Systems, *J. Mech. Des.*, 117, 171–176, https://doi.org/10.1115/1.2836451.
15. **Kargarnovin M.H., Najafizadeh M.M., Viliani N.S.** (2007), Vibration control of a functionally graded material plate patched with piezoelectric actuators and sensors under a constant electric charge, *Smart Mater. Struct.*, 16, 1252.
16. **Lam K.Y., Peng X.Q., Liu G.R., Reddy J.N.** (1997), A finite-element model for piezoelectric composite laminates, *Smart Mater. Struct.*, 6, 583.
17. **Lee H.-J., Saravanos D.A.** (1996), Coupled layerwise analysis of thermopiezoelectric composite beams, *AIAA J.*, 34, 1231–1237.
18. **Lee H.-J., Saravanos D.A.** (1998), The effect of temperature dependent material properties on the response of piezoelectric composite materials, *J. Intell. Mater. Syst. Struct.*, 9, 503–508.
19. **Liew K.M., He X.Q., Ng T.Y., Sivashanker S.** (2001), Active control of FGM plates subjected to a temperature gradient: modelling via finite element method based on FSDT, *Int. J. Numer. Methods Eng.*, 52, 1253–1271.
20. **Peng X.Q., Lam K.Y., Liu G.R.** (1998), Active vibration control of composite beams with piezoelectrics: a finite element model with third order theory., *J. Sound Vib.*, 209, 635–650.
21. **Qiu J., Ji H., Zhu K.** (2009), Semi-active vibration control using piezoelectric actuators in smart structures, *Front. Mech. Eng. China*, 4, 242–251.
22. **Raja S., Sinha P.K., Prathap G., Dwarakanathan D.** (2004), Thermally induced vibration control of composite plates and shells with piezoelectric active damping, *Smart Mater. Struct.*, 13, 939.
23. **Reddy J.N.** (1984), A Simple Higher-Order Theory for Laminated Composite Plates, *J. Appl. Mech.*, 51, 745–752.
24. **Sharma A., Kumar R., Vaish R., Chauhan V.S.** (2016), Experimental and numerical investigation of active vibration control over wide range of operating temperature, *J. Intell. Mater. Syst. Struct.*, 27, 1846–1860.
25. **Song, G., Zhou, X., Binienda, W.** (2004), Thermal deformation compensation of a composite beam using piezoelectric actuators, *Smart Mater. Struct.*, 13, 30.
26. **Tzou H.S., Bao Y.** (1995), A theory on anisotropic piezothermoelastic shell laminates with sensor/actuator applications, *J. Sound Vib.*, 184, 453–473.
27. **Tzou H.S., Gadre M.** (1989), Theoretical analysis of a multi-layered thin shell coupled with piezoelectric shell actuators for distributed vibration controls, *J. Sound Vib.*, 132, 433–450.
28. **Tzou H.S., Tseng C.I.** (1990), Distributed piezoelectric sensor/actuator design for dynamic measurement/control of distributed parameter systems: a piezoelectric finite element approach, *J. Sound Vib.*, 138, 17–34.
29. **Wang D., Fotinich Y., Carman G.P.** (1998), Influence of temperature on the electromechanical and fatigue behavior of piezoelectric ceramics, *J. Appl. Phys.*, 83, 5342, https://doi.org/10.1063/1.367362.
30. **Ye Z.-G.** (2008), *Handbook of advanced dielectric, piezoelectric and ferroelectric materials: Synthesis, properties and applications*, Elsevier.
31. **Zhou X., Chattopadhyay A., Gu H.** (2000), Dynamic responses of smart composites using a coupled thermo-piezoelectric-mechanical model, *AIAA J.*, 38, 1939–1948.
32. **Zorić N.D., Simonović A.M., Mitrović Z.S., Stupar S.N.** (2013), Optimal vibration control of smart composite beams with optimal size and location of piezoelectric sensing and actuation, *J. Intell. Mater. Syst. Struct.*, 24, 499–526.
33. **Zou Y., Tong L., Steven G.P.** (2000), Vibration-based model-dependent damage (delamination) identification and health monitoring for composite structures — a review, *J. Sound Vib.*, 230, 357–378, https://doi.org/10.1006/jsvi.1999.2624.